INFORMATION TO USERS

This reproduction was made from a copy of a document sent to us for microfilming. While the most advanced technology has been used to photograph and reproduce this document, the quality of the reproduction is heavily dependent upon the quality of the material submitted.

The following explanation of techniques is provided to help clarify markings or notations which may appear on this reproduction.

1. The sign or "target" for pages apparently lacking from the document photographed is "Missing Page(s)". If it was possible to obtain the missing page(s) or section, they are spliced into the film along with adjacent pages. This may have necessitated cutting through an image and duplicating adjacent pages to assure complete continuity.

2. When an image on the film is obliterated with a round black mark, it is an indication of either blurred copy because of movement during exposure, duplicate copy, or copyrighted materials that should not have been filmed. For blurred pages, a good image of the page can be found in the adjacent frame. If copyrighted materials were deleted, a target note will appear listing the pages in the adjacent frame.

3. When a map, drawing or chart, etc., is part of the material being photographed, a definite method of "sectioning" the material has been followed. It is customary to begin filming at the upper left hand corner of a large sheet and to continue from left to right in equal sections with small overlaps. If necessary, sectioning is continued again–beginning below the first row and continuing on until complete.

4. For illustrations that cannot be satisfactorily reproduced by xerographic means, photographic prints can be purchased at additional cost and inserted into your xerographic copy. These prints are available upon request from the Dissertations Customer Services Department.

5. Some pages in any document may have indistinct print. In all cases the best available copy has been filmed.

University Microfilms International
300 N. Zeeb Road
Ann Arbor, MI 48106

Skillman, Evan David

PHYSICAL CONDITIONS IN GIANT EXTRAGALACTIC H II REGIONS

University of Washington PH.D. 1984

PLEASE NOTE:

In all cases this material has been filmed in the best possible way from the available copy. Problems encountered with this document have been identified here with a check mark __✓__.

1. Glossy photographs or pages _____
2. Colored illustrations, paper or print _____
3. Photographs with dark background _____
4. Illustrations are poor copy _____
5. Pages with black marks, not original copy __✓__
6. Print shows through as there is text on both sides of page _____
7. Indistinct, broken or small print on several pages __✓__
8. Print exceeds margin requirements _____
9. Tightly bound copy with print lost in spine _____
10. Computer printout pages with indistinct print _____
11. Page(s) _____ lacking when material received, and not available from school or author.
12. Page(s) _____ seem to be missing in numbering only as text follows.
13. Two pages numbered _____. Text follows.
14. Curling and wrinkled pages _____
15. Other _____

Physical Conditions in Giant Extragalactic H II Regions

by

Evan David Skillman

A dissertation submitted in partial fulfillment

of the requirements for the degree of

Doctor of Philosophy

University of Washington

1984

Approved by _____

(Chairperson of Supervisory Committee)

_____

_____

Program Authorized

to Offer Degree Astronomy

Date 5 November 1984

In presenting this dissertation in partial fulfillment of the requirements for the Doctoral degree at the University of Washington, I agree that the Library shall make its copies freely available for inspection. I further agree that extensive copying of this dissertation is allowable only for scholarly purposes, consistent with πfair useπ as prescribed in the U. S. Copyright Law. Requests for copying or reproduction of this dissertation may be referred to University Microfilms, 300 North Zeeb Road, Ann Arbor, Michigan 48106, to whom the author has granted πthe right to reproduce and sell (a) copies of the manuscript in microform and/or (b) printed copies of the manuscript made from microform.π

Signature 

Date November 5, 1984

University of Washington

Abstract

Physical Conditions in Giant Extragalactic H II Regions

by Evan David Skillman

Chairperson of the Supervisory Committee:

Professor Bruce Balick

Department of Astronomy

Giant Extragalactic H II Regions (GEHRs) in nearby galaxies have been observed at both radio and optical wavelengths. Narrow band optical imaging, large and small aperture optical spectrophotometry, radio continuum imaging at λ6 cm and λ21 cm, and λ21 cm H I spectral line mapping have been employed to investigate the point to point variations of the physical conditions within and surrounding the GEHRs.

Measurements of reddening and extinction were found to be strongly dependent on resolution. Variations in extinction as measured by the optical method were not found to correlate with those measured with the optical-radio method. In at least one case this was due to the presence of a nonthermal radio continuum source.

Significant differences in optical line strength ratios exist between different points in a single GEHR. These differences point to variations of the physical conditions within the GEHR. The results of standard abundance analysis techniques are therefore dependent on the size and position of the observing aperture. Derived oxygen abundances are quite consistent throughout a single GEHR, but nitrogen abundances show significantly large variations.

A supernova remnant (SNR) has been discovered in NGC 5471. Nonthermal radio continuum emission detected in other GEHRs makes it likely that there are SNRs in these regions also. It has been shown that, although SNRs may be difficult to detect in GEHRs, their presence can significantly alter the results of abundance analyses.

Wolf-Rayet stars are found to be an important component of the stellar populations in only a small fraction of GEHRs.

All GEHRs are found adjacent to large H I concentrations. Observations of the neutral hydrogen gas surrounding GEHRs reveals a correlation between H I surface density and velocity dispersion. The velocity dispersion in the adjacent neutral gas is comparable to the velocity dispersion in the GEHR. This strongly favors a gravitational explanation for the anomalously broad emission line widths observed in GEHRs.

Table of Contents

List of Tables

List of Figures

Acknowledgements

I wish to gratefully acknowledge the contributions that Dr. Bruce Balick has made to this dissertation. The diversity and depth of the observational program are attributable to his fecund mind. Dr. Balick provided encouragement, critical analysis, and advice at all stages of this long project.

I would also like to thank Dr. Karl-Heinz Bohm, Dr. Paul Hodge, and Dr. Bruce Margon for serving on my committee and critically reading the thesis. Dr. Margon also arranged for the Mt. Lemmon observing time. I am indebted to both Dr. Paul Hodge and Dr. Robert Kennicutt for sharing their knowledge of extragalactic H II regions.

The directors, staffs, and telescope allocation committees of the Kitt Peak National Observatory and the National Radio Astronomy Observatory are to be thanked for generous amounts of observing time, excellent observing support, the production of reduction and analysis programs, and seemingly unlimited use of image processing facilities.

Mr. Bill Spiesman is to be thanked for assistance and advice on computing problems on innumerable occassions. Mr. Alejandro Raga provided several computations. Getting computing tasks done was made much easier by the most conscientious and competent system manager, Mr. J. James Belonis. The nice figures were produced using John Tonry's plotting program. The very nice figures were drafted by

Jason Cardelli.

It is traditional to note that the best part of being a graduate student in astronomy at the University of Washington is the time spent with the other graduate students. Dr. David Muchmore, Dr. Hugh Harris, Dr. Greg Bothun, Dr. Verne Smith, Dr. Edward Olszewski, Dr. Doug Geisler, Mr. Greg Taylor, Mr. Bernard Bates, Mr. Jason Cardelli, Mr. Scott Anderson, Mr. Simon Radford, Mr. Bill Spiesman, Mr. Don Boggs, Mr. Schuyler Van Dyk, Mr. Mario Mateo, Mr. Mike Bolte, Mr. Alejandro Raga, and Ms. Patricia Bates are all to be thanked for creating an environment that fosters curiosity, cooperation, and a commitment to doing good work.

Lastly, and most importantly, I would like to thank Mom and Dad and Leslie for the support and love they have always given me.

Chapter I Introduction

Giant extragalactic H II regions (GEHRs) are anomalously large regions of star formation. The study of GEHRs has lead to many important results in the diverse fields of stellar evolution, the structure and evolution of galaxies, and cosmology. Although great progress has been made in the study and understanding of GEHRs, there remain many unanswered questions about many of their fundamental properties. The purpose of this work is to perform high resolution observations at radio and optical wavelengths in order to better understand GEHRs. This introductory chapter will begin with a review of GEHR related research, followed by a discussion of deficiencies in our knowledge of GEHRs, and conclude with a brief overview of the purposes and procedures of this thesis.

Before reviewing GEHR research, it is best to start with a description of GEHRs. H II regions are defined by Osterbrock (1974) to be 'regions of interstellar gas in which the exciting stars are O or early B type stars of population I'. Typical H II regions in our galaxy have one or a few exciting stars and sizes ranging from .1 to 10 pc. There is no universally accepted definition dividing GEHRs from normal H II regions, but typical GEHRs require the ionizing flux of hundreds of exciting stars and can range up to 1 kpc in extent. It is important to note that GEHRs are rare objects. GEHRs are found only in late type spiral and irregular galaxies, and there are no known GEHRs in the Andromeda galaxy or our own. The nearest example

of a GEHR is the 30 Doradus nebula in the Large Magellanic Cloud. Despite the rarity of GEHRs, most of the H II regions that are observed outside of the local group are GEHRs.

Highlights of Previous GEHR Research

GEHRs have been the targets of many diverse observational programs, both because of their potential to probe many questions of stellar evolution and cosmology, and because they are intrinsically fascinating objects. It is easy to develop an appreciation for the role of GEHRs in extragalactic research from just a short list of recent works. An equally short list of unsolved problems concerning the properties of these objects will intrigue the curious and stir questions concerning the conclusions of the works on the first list. It is the purpose of this section to foster both appreciation and doubt.

Because of their great luminosities, GEHRs were one of the first classes of objects to be recognized and studied in other galaxies. The study of differences between the optical spectra of H II regions within the same galaxy has been a very fruitful field. Aller (1942) discovered that the [O III] emission was relatively weak in H II regions in the inner part of M 33 and relatively strong in the outer H II regions. The seminal paper of Searle (1971) explored this idea through observations of integrated spectra of H II regions, confirmed that the spectrum of an H II region in a spiral galaxy was dependent

on its position in the galaxy, and proposed that this difference was due to an abundance gradient in the disk of the parent galaxy. In the decade since the work of Searle, studies of H II regions in dozens of spiral galaxies have always shown the same trends: the $\lambda5007/\lambda4861$ ratio (often called the excitation parameter, and usually indicative of the electron temperature) in the H II regions increases with increasing distance from the center of the galaxy, and the measured abundances decrease with increasing radius. The exhaustive survey of McCall (1982) has resulted in a picture of H II regions as members of a one parameter family. In this picture, total oxygen abundance is the determining parameter. Thus, the H II regions in a spiral galaxy present a record of the star formation history and heavy element abundance enhancement of that galaxy. Under the assumption that H II regions lie in a one parameter sequence, it is possible to discover how heavy elements are produced in stars. From correlations of heavy element abundances, McCall proposes that sulfur, in addition to oxygen, is a primary product of nucleosynthesis, and nitrogen is a secondary product.

Searle also observed H II regions in the irregular galaxy NGC 4214 and found all regions to show high excitation. Subsequent studies of H II regions in irregular galaxies have shown that their heavy element abundances are uniform across the galaxy and generally lower than in spirals. A class of extreme examples of this observation was first discovered by Sargent and Searle (1970). Their

letter reported the discovery of 'isolated extragalactic H II regions' - galaxies that appear to consist of a single giant H II region. From models of the evolution of the U, B, and V, colors of galaxies, Searle, Sargent and Bagnuolo (1973) concluded that these blue dwarf galaxies are experiencing short lived, intense bursts of star formation. Later modelling experiments (eg. Huchra 1977) confirmed this basic result. When many of these objects were studied spectroscopically (French 1980, and later Kinman and Davidson 1981, and Kunth and Sargent 1983), it was realized that they represented probes of a metal poor environment.

Peimbert and Torres-Peimbert (1974) first proposed that, given the large range in observable heavy element abundances, it might be possible to discover a {O/H}/{He/H} relationship, extrapolate to zero oxygen abundance, and determine the pregalactic helium abundance. Of the most recent attempts at this experiment, Lequeux et al. (1979), French (1980), and Rayo, Peimbert, and Torres-Peimbert (1982) find evidence of such a relationship. Kinman and Davidson (1981) and Kunth and Sargent (1983) find no evidence for a correlation of helium abundance with oxygen abundance.

In 1970, Smith and Weedman (1970b) published observations of anomalously broad (FWHM up to 60 km/s) line profiles from GEHRs in M101 and M33. Because these observations were made with a Fabry-Perot with a large aperture covering the entire GEHR, Smith and Weedman suspected that the large velocities observed were indicative

of large differences in gas velocity throughout the complex, not large velocity dispersions in the gas. This was consistent with observations of galactic H II regions, where global turbulent velocity measurements were consistently larger than small scale observations (Smith and Weedman 1970a). A detailed study of the 30 Doradus nebula (Smith and Weedman 1972) revealed broad lines on the smallest observable scales (3.3 pc). Because of the presence of many Wolf-Rayet (WR) stars in 30 Dor, it was proposed that the stellar winds of WR stars may be responsible for the large gas velocities. By studying a larger sample of GEHRs, Melnick (1977, 1978) discovered correlations of the global Hα line profile widths with both the linear diameters and the parent galaxy luminosities. Melnick then used both correlations to derive the distance to the M101 group. The cause of the anomalously broad lines is still not resolved. Theoretical calculations by Weaver et al. (1977), Dyson (1979), and Lamers (1982) showed that it is possible for the stellar winds of a number of WR stars to combine to form a wind-blown shell. This shell could give rise to broad emission lines. Rosa and D'Odorico (1982) have shown the energy budget to be feasible for the case of NGC 604. The ubiquity of WR stars in the GEHRs of M 33 has been established by Conti and Massey (1981) and D'Odorico and Rosa (1981).

The large number of exciting stars in a GEHR make them extremely luminous objects. Because GEHRs can be seen to great distances, their utility as distance indicators has been investigated in great

detail. Although the work in this thesis is not directly aimed at the problems of H II regions as extragalactic distance indicators, (it is in this context that GEHRs are best known) and, since much has been learned about GEHRs through studies related to distance determination, a brief review is warranted.

Sandage and Tammann (1974a) showed that the mean diameters of the largest H II regions in Sc and Irr galaxies correlated with the luminosity of the parent galaxy. Thus, H II region diameters were used as calibrators to help extend the distance scale from the nearest galaxies, where Cepheid variable stars are observable, to the Virgo cluster (Sandage and Tammann 1974b,c). Later work by Kennicutt (1979) produced improvements to the method of measuring H II region diameters, but left the distance scale of Sandage and Tammann, for the most part, unchanged. van den Bergh (1980) showed that the power of H II regions as distance indicators relied on the (unjustified) assumption of a linear correlation between H II region sizes and galaxy luminosity, and the classification of parent galaxy luminosity classes. van den Bergh concluded that when the uncertainties of these are properly accounted for, H II region diameters are only marginally useful as distance indicators.

In their study, Sandage and Tammann introduced the concept of a core-halo morphology for GEHRs. This was based simply on the appearance of these regions on photographic plates. The core of a region is the highest surface brightness, central component, and the

halo is the extent to the limit of detection. Sandage and Tammann did not try to give a physical meaning to the definitions other than mentioning that radiation bounded regions would have sharp borders and the sizes of the halos may be reliable for this reason.

Kennicutt (1979) used deep Hα exposures of a large fraction of the H II regions observed by Sandage and Tammann to demonstrate that the majority of GEHRs show a complex structure that cannot be easily described as a core-halo morphology. Multiple cores and halos that extended into diffuse emission associated with a spiral arm were two common features noted in GEHRs. Beside these morphological insights, the works of Sandage and Tammann and Kennicutt did not concentrate on the physical conditions in GEHRs.

By combining the H II region diameters of Sandage and Tammann (1974a,b) with the Hα line width measurements of Melnick (1977, 1979) and Smith and Weedman (1970), Terlevich and Melnick (1981) found a correlation between size (as defined by Sandage and Tammann) and line width for GEHRs similar to the types previously derived for elliptical galaxies and globular clusters. By combining this data with Hβ flux measurements, a correlation between Hβ flux and the fourth power of the emission line width was discovered. The GEHRs were found to bridge the gap between elliptical galaxies and globular clusters in the log (velocity dispersion) versus log (luminosity) diagram. There were two important results from this work. First, a new explanation of the anomalously broad emission was proposed. From

the comparison of GEHRs with globular clusters and elliptical galaxies, it was concluded that the large velocity dispersions observed in GEHRs were a result of the motions of individual ionized gas clouds in the gravitational potential of a bound system of stars and gas. Second, given the correlation of GEHR luminosity and line width, it is possible, in principle, to develop a distance determination scheme based on these two observables.

Deficiencies in Our Understanding of GEHRs

The last section contained evidence that all is not well in the realm of GEHR research. The details of current problems in GEHR research will be presented in this section.

Before optical spectra can be converted into the relative line strengths necessary for abundance analysis, a correction for reddening must be applied. Normally the correction is determined by comparing the observed relative fluxes of the Balmer emission lines with the theoretically predicted values. A second method involves combining radio continuum data with the Balmer line strengths and an assumption of a value for the ratio of selective to total extinction. In principle these two methods should agree. In practice, Israel and Kennicutt (1980) have shown that these two measurements are always greatly discrepant for GEHRs. The possible explanations range from non-uniform absorption or internal reddening to the differences in the way the radio and optical data are acquired. Recently, Mathis

(1983) has shown that a wavelength dependence in the albedo of dust grains will significantly alter the interpretation of the Balmer decrement. Altogether, these studies imply that the way in which optical spectra are normally corrected for reddening may be in error.

A second step required in the process of converting optical spectra into measurements of relative chemical abundances consists of determining the temperature and density of the gas. These are normally derived from forbidden line strength ratios. It is then necessary to model the temperature and density variations within the region, or make certain simplifying assumptions. For most GEHR observations, there is insufficient information to develop a detailed model. Generally, a two zone model is applied. The region is divided into high and low ionization zones. Peimbert and Costero (1969) devised a method of taking into account temperature variations within the zones. Several researchers (Dufour et al. 1980, Pagel et al. 1979) have had a great deal of success using a differential analysis technique based on theoretical model H II regions. In these studies, success is defined as consistency. The underlying assumptions are that the temperature, density, and chemical abundance variations within a region are very small, and that photons from ordinary main sequence stars provide all of the ionization and heating to the gas. It is not clear that these assumptions have been thoroughly tested, or whether several different models could yield consistent predictions of line ratios.

As mentioned in the last section, the source of the anomalously broad lines observed from GEHRs is a matter of contention. To date there are three prime candidates: the winds of WR stars, supernovae explosions, and gravitational potential energy. High spatial and velocity resolution observations of a large sample of GEHRs (Gallagher and Hunter 1983, Skillman and Balick 1984) have proven inconclusive in determining the energy source. An extensive mapping of the GEHR NGC 604 (Rosa and Solf 1984) has shown frequent superpositions of WR stars and large velocity gas motions. This is the strongest evidence to date that WR stars are responsible for the anomalously broad emission lines observed in GEHRs.

The Observational Program

The main thrust of this work is to obtain high spatial resolution observations at optical and radio wavelengths of a number of relatively nearby GEHRs. By analyzing the physical conditions and the variations in the physical conditions in a small number of GEHRs, it is hoped that some of the questions described in the previous section may be answered.

The observations consist of narrow-band optical imaging in the emission lines of Hα, Hβ, and [O III] λ5007, and continuum emission at wavelengths near to the emission lines. Radio continuum images at λ6 cm and λ20 cm were obtained with spatial resolution matching that of the optical images. Both large aperture and small aperture

spectrophotometry were carried out. In addition, the neutral gas in the vicinity of the GEHRs was mapped in the λ21 cm line of hydrogen.

With the Hα images it is possible to determine the distribution of the ionized gas. Hα/Hβ ratio images provide a map of the reddening of the region. Hα/λ5007 ratio images reveal the variations in excitation within the region. The small aperture spectrophotometry then allows an analysis of the physical conditions and chemical abundances in interesting structures identified in the optical imaging. The optical spectrophotometry is also the most sensitive way to search for the presence of WR stars. The large aperture spectrophotometry serves the dual purpose of calibrating the optical images, and emulating observations of GEHRs at larger distances (lower spatial resolution).

Radio continuum maps can be compared to the Hα maps to measure optical extinction under the assumption that the radio emission is due solely to thermal bremsstrahlung ('thermal'). By observing at two radio wavelengths, the radio spectral index can be mapped, and nonthermal sources (presumably supernova remnants) can be detected and separated from the thermal emission. The neutral hydrogen measurements can be used to study the kinematics of the gas in the vicinity of the GEHR and gauge the mass of the cloud from which the GEHR was born.

Chapter II Instruments, Observations, and Data Reduction

The observations performed for this thesis were made with a large variety of telescopes and accompanying instrumentation. Much of the data calibration and reduction was carried out with the assistance of computer programs developed at the telescope's managing or support institution. This chapter is a description of those telescopes, instruments, and computer programs. A detailed description of each telescope, instrument, and computer program would be impractical here; instead, the purpose of this chapter is to provide the reader with enough information to critically judge the strengths and limitations of the data.

Optical Imaging

Four nights of observing time were awarded on the Kitt Peak National Observatory (KPNO) 2.1 meter telescope with the video camera (Butcher and Oemler 1978). The video camera system consists of an intensified silicon image tube focused on a target that is read in a 256 x 256 array by a scanning electron beam. The output is accumulated and the accumulating picture can be monitored in real time. Used with the KPNO 2.1 meter telescope, the video camera affords a 2 arc minute usable field of view with a pixel size of 0.56 . The program GEHRs were observed through interference filters with wavelength coverages centered on emission lines ('on' filters) and wavelength coverage adjacent to the emission lines ('off'

filters). The filter characteristics are listed in Table 2.1.

The raw pictures have to be calibrated for dark bias, pixel to pixel gain variations, and image tube illumination variations. The dark bias was determined from long integrations with the tube at full voltage, but the shutter closed to all light. The second two calibrations must be performed for each filter as there may be spectral dependences. The pixel to pixel variations were determined by integrations of a quartz lamp through each filter at the beginning and end of each night's observing. The illumination variations were measured by taking exposures of a star-free field near twilight.

At the end of the run, the data were taken to the main offices of the KPNO where a computer program accepted the raw images, subtracted the bias level, and divided by the high frequency and low frequency response functions. A second program was run to correct for the geometrical distortion in the camera tube as mapped by the observatory staff.

These calibrated images were then studied via the KPNO image processing system (IPPS) (Tody 1980). Because the different interference filters shifted the image slightly (~ 1 pixel) the first required step was to shift all of the frames to the same coordinate system. When possible, this was done using stars within the field, but in some cases the intensity peaks in the GEHRs themselves had to be used. Precise locations of the chosen reference objects were

Table 2.1

Telescope Parameters for Optical Imaging

Observation	Filter		Integration Time/Seeing (FWHM)		
Frame	λ_o	$\Delta\lambda$	NGC 5471	NGC 4214	NGC 2363
	(angstroms)		(minutes/arc seconds)		
Hα on	6563	20	13.7/2	13.7/2	13.7/3.0
off	6400	100	6.8/2	6.8/2	6.8/3.2
Hβ on	4861	30	13.7/2	13.7/2	13.7/3.5
off	4693	138	6.8/2	6.8/2	6.8/3.2
λ5007 on	5007	16	13.7/2	13.7/2	13.7/2.8 6.8/2.0
off	5300	128	6.8/2	6.8/2	13.7/2.8 3.4/2.0
λ4363 on	4363	13	...	...	13.7/2.0
off	4400	83	...	...	6.8/2.0

determined through point spread function fitting, and the fractional pixel shifting was performed with a cubic spline interpolation algorithm. The sky level was determined at several positions in each frame, and a mean sky level was then subtracted.

The relative throughput of each filter was determined from observations of standard stars. The on and off frames were scaled to the ratios determined from the standard star frames, and then the scaled off frame was subtracted from the corresponding on frame. This yielded a continuum free emission line image of the GEHR.

Before ratio maps can than be constructed by simply dividing two emission line images, any differences in seeing must be measured and accounted for. Convolving an image with a two dimensional Gaussian smoothing function will correct for seeing differences and also improve the signal to noise ratio in the image.

Optical Spectroscopy

Optical spectroscopy was performed with the KPNO 2.1 meter telescope and the Intensified Image Dissector Scanner (IIDS), the KPNO #1 .9 meter telescope and the Intensified Reticon Scanner (IRS), and the Mt. Lemmon 1.5 meter telescope and the Image Dissector Scanner (IDS). Specifications of the IIDS, IRS, and the IDS are listed in Table 2.2. All three instruments are dual-beam, multichannel spectrophotometers. Each system had a TV acquisition system enabling quick set up for each observation. For all these

Table 2.2

Telescope Parameters for the Optical Spectrophotometry

Telescope	Instrument	Aperture (")	Resolution (angstroms)	Wavelength Coverage	Positions NGC 5471	NGC 4214	NGC 2363
Mt. Lemmon 1.5 m	IDS	4.7	12	4000-6800	A,B,C,D	A,B,C,N	
KPNO 2.1 m	IIDS	4.2	8	3400-5200	A,B,C,D	A,B,C,N	A,B,C,II
				5600-7400	A,B,C	A,B,C,N	A,B,C
KPNO .9 m	IRS	22.0	13	3600-7200	core	core	core

instrumental set-ups, the accumulation of the data could be monitored in real time, allowing the decision to end an integration when a sufficient signal to noise ratio was obtained. Observations were made alternating the source between the two spectrograph apertures in an object-sky sky-object sequence. Care was taken to insure that the sky aperture was not contaminated by sources such as nearby stars.

Calibration of the instruments proceeded in a similar fashion to the calibration of the video camera. Bias measurements where made at the beginning and end of each evening. For the IRS, bias was also measured at one hour intervals throughout the night. Exposures of quartz lamps were used to determine channel to channel variations in the instrument. These exposures were taken at the beginning and end of each night. Helium-Neon-Argon comparison lamps were observed to set the wavelength scaling. Standard stars from the list of KPNO standards were observed for flux calibration.

Calibration of the data consisted of subtracting the bias, dividing by the channel to channel response determined from the quartz exposures and applying a linear wavelength scaling derived from a polynomial fit to the dispersion solution of the comparison spectra. Average sky and object spectra were produced for each object for each beam, and the two were subtracted to get an object spectrum. A flux scale was determined from the standard star observations and an application of the standard extinction curves. Line strengths were measured from the fluxed spectra with a Gaussian

fitting routine written by B. Balick. In those cases where nearby lines affected the measurement of a line, multiple lines were fitted simultaneously. In many cases, a number of parameters which are known a priori (e.g. equal line velocities and widths, ratios of line fluxes) were fixed in order to allow the Gaussian fitting routine to converge to a solution. The program produces an estimate of the uncertainty in the flux and this was recorded for all emission lines measured.

Radio Continuum Imaging

Observations of several GEHRs were made at radio wavelengths with the National Radio Astronomy Observatory (NRAO) Very Large Array (VLA). The VLA consists of 27 separate 25 meter diameter antennae in a 'wye' configuration. Each antenna pair operates as an interferometer, sampling spatial frequencies on the sky determined by the projected baseline separation and orientation. The rotation of the earth changes the orientation of the baselines with respect to the source, such that a multiplicity of spatial frequencies are sampled. At any instant of time the VLA acts something like an optical telescope whose primary mirror is masked by a black sheet in which a Y-shaped array of holes has been bored. The resulting instantaneous picture is crossed by a series of diffraction patterns. Pictures are recorded continuously while the mask rotates due to the rotation of the earth. When the data is summed, the effect is to wash out the diffraction patterns (the sidelobes), improve the signal

to noise, and increase the contrast between real sky features and the background.

Time was awarded to use the VLA as a 'scaled array' to make maps of the radio continuum and radio spectral index at λ6 cm and λ20 cm. The principle of a scaled array is to observe at two different wavelengths in two different configurations such that the spatial resolution is nearly identical for the two observations. The λ20 cm observations were made in the A configuration, the most extended of the VLA configurations. This produces a 1 synthesized beam size. The λ6 cm observations were made in the B configuration to match this beam size. The instrumental parameters for the radio continuum observations for NGC 2363 and the largest H II region in NGC 4214 are listed in table 2.3. These instrumental parameters are typical for all of the radio continuum measurements except NGC 5471. For NGC 5471 λ20 cm measurements were made in the B array and λ6 cm measurements in the C array yielding a 3 synthesized beam.

Integration times varied from one to two hours per object, thus a full synthesis (8 hours) was not performed. Beside the loss in sensitivity, integration times of less than 8 hours produce an incomplete sampling of spatial frequencies, resulting in larger sidelobes in the synthesized beam. The most undersampled size scales correspond to the longest baselines. In practice, a taper is applied to the data resulting in a loss of spatial resolution but a decrease in the strength of the sidelobes of the synthesized beam. The use of

Table 2.3

Telescope Parameters for Radio Continuum Imaging

Frequency	1464.9 MHz	4885.1 MHz
VLA Configuration	A	B
Number of Antennae	27	27
Integration (minutes)		
NGC 4214	90	115
NGC 2363	100	120
Bandwidth	50 MHz	50 MHz

a taper results in a better behaved map.

Radio Spectral Line Imaging

Maps of the neutral hydrogen surrounding NGC 5471, NGC 2363, and the largest H II region in NGC 4214 were produced by observing with the VLA at λ21 cm in the spectral line mode. The spectral line data and the observing parameters for these observations are presented in chapter VII. The resolution and sensitivity for these maps are inferior to the continuum maps. The loss in sensitivity is a result of the much smaller bandwidth necessary to gain velocity resolution. A courser spatial resolution is necessary to improve the signal to noise ratio for the extended H I clouds.

Chapter III The Data

Although several GEHRs were observed with each instrument, three objects stand out as having the most complete data sets. The data for these three regions: NGC 5471, NGC 2363, and the largest H II region in NGC 4214, are presented in this chapter. All of these regions are 'multiple- core' regions, that is, the core is easily divided into two or more distinct components. Following Skillman and Balick (1984) these smaller central components will be called nuclei. These three regions will serve as good candidates to compare and contrast, because, as will be seen from the data, these three regions span a large range in temperature. Their nominal electron temperatures are 10,000 K for NGC 4214, 12,000 K for NGC 5471, and 15,000 K for NGC 2363.

The purpose of this chapter is to present a 'first look' so that the reader can become familiar with both the individual objects and the type of data obtained. The subsequent chapters will each be dedicated to one single problem and will draw on the relevant data from all of the objects observed.

GEHR Images

Figures 3.1 and 3.2 show contour maps of the Hα, Hβ, λ5007, and blue optical continuum, and the λ6 cm and λ20 cm radio continuum images of NGC 5471. Five nuclear positions are labeled in the Hα map. A quick inspection reveals that the Hα and Hβ images are nearly

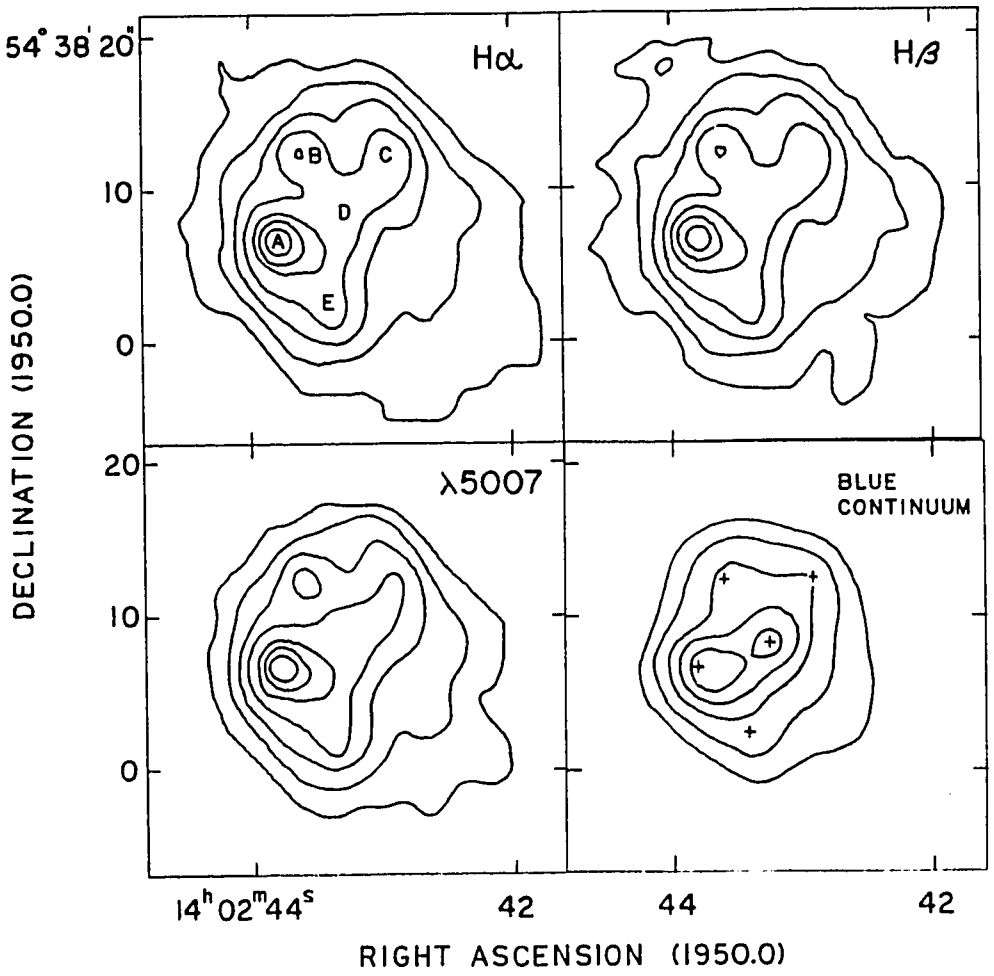

Figure 3.1 Optical Imaging of NGC 5471

Contour map representations of the video camera images of NGC 5471 in the light of Hα, Hβ, λ5007, and the blue continuum. The nuclear positions as referred to in the text are marked in the Hα image. The contour levels are set at 80%, 60%, 40%, 20%, 10%, 5%, and 2% of the peak in each image, except for the blue continuum image for which the 5% and 2% contours are not included.

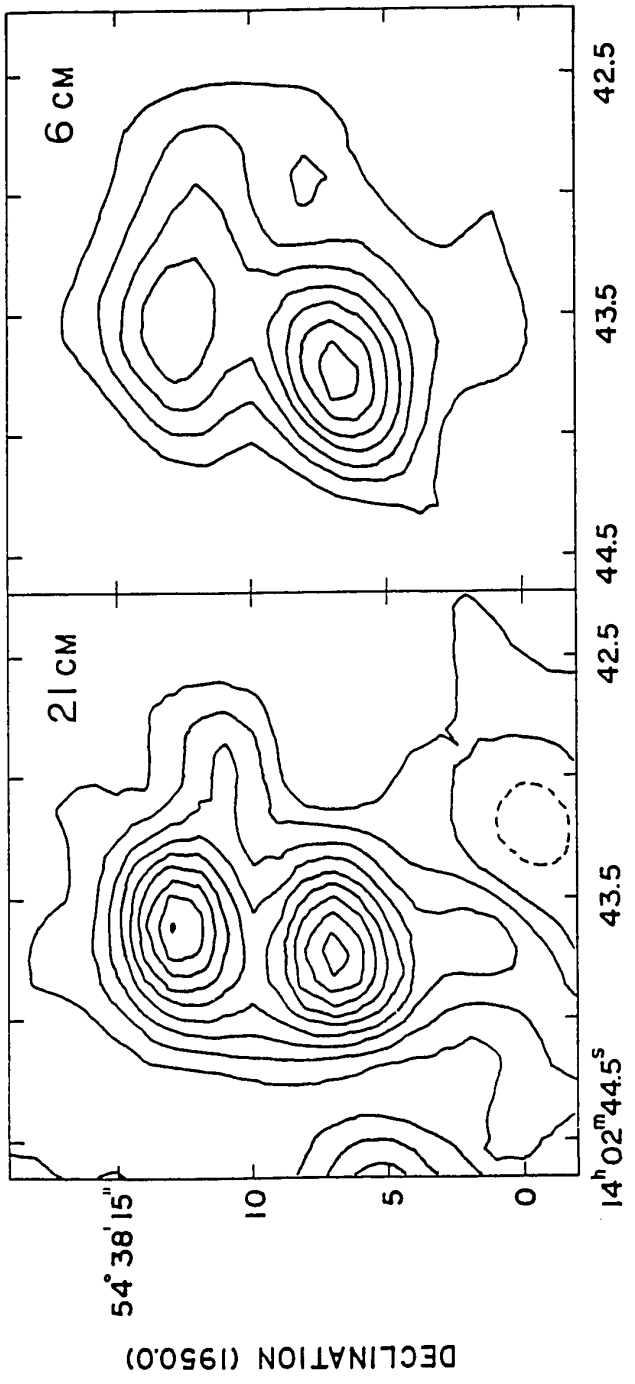

Figure 3.2 Radio Continuum Imaging of NGC 5471

Contour map representations of radio continuum images of NGC 5471. These are clean maps constructed with a 2 FWHM synthesized beam. The contour levels are set at 3 mJy/beam in both maps. Negative contours are dashed.

identical. The only major difference occurs in the southwest corner where the Hβ emission appears relatively weaker. The continuum at nucleus D is much stronger relative to the nebular emission than at the other nuclear positions. Nuclei A and B are both clearly shown in the radio continuum maps. It is clear that the ratio of the flux in nucleus A to that in nucleus B is greater at λ6 cm than at λ20 cm. Nucleus A has a nearly flat radio spectrum, while nucleus B has a negative spectral index. These indices are indicative (or, at least consistent) with A and B being thermal and nonthermal emission regions, respectively.

Figures 3.3 and 3.4 show the images of the largest H II region in NGC 4214. Note that of the three nuclei marked in the Hα map, nucleus A is the brightest in the blue continuum and faintest in the nebular emission images. Note also that nucleus A is much weaker than the other two nuclei in the radio continuum.

Images of NGC 2363 are shown in figures 3.5, 3.6, and 3.7. The Hα, λ5007, and the blue continuum images are compared in figure 3.5. The Hα map shows three nuclear positions and another H II region to the east. The fainter H II region is the second brightest H II region in NGC 2366, and is designated II. Figure 3.6 shows λ5007 and λ4363 images acquired during better seeing conditions. The radio continuum maps are presented in figure 3.7.

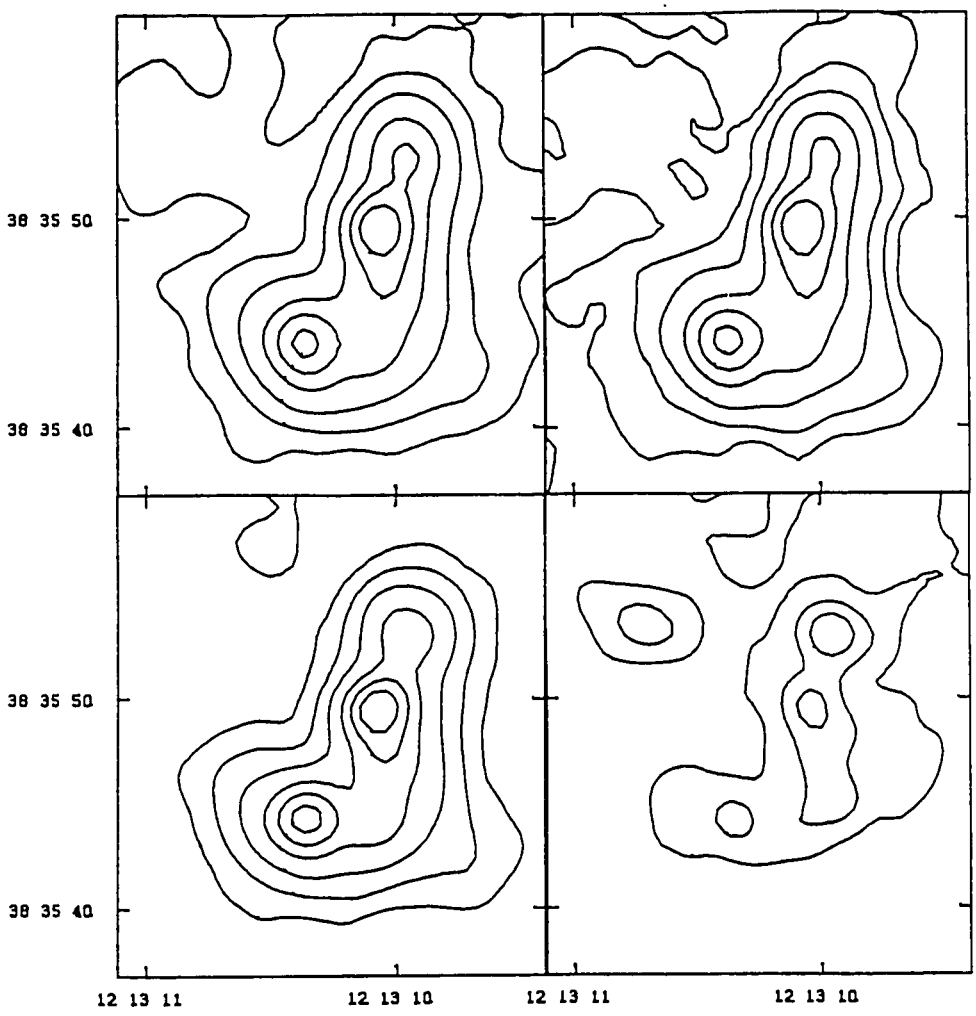

Figure 3.3 Optical Imaging of NGC 4214

Contour map representations of the video camera images of NGC 4214 in the light of Hα, Hβ, λ5007, and the blue continuum. The nuclear positions as referred to in the text are marked in the Hα image. The contour levels are set at 80%, 60%, 40%, 20%, 10%, and 5% of the peak in each image, except for the blue continuum image for which the 20% and 10% contours are not included.

Figure 3.4 Radio Continuum Imaging of NGC 4214

Contour map representations of radio continuum images of NGC 4214. These are clean maps constructed with a 2 FWHM synthesized beam. The contour levels are set at 80%, 60%, 40%, 20%, 10%, and 5% of the peak in each image. Negative contours are dashed.

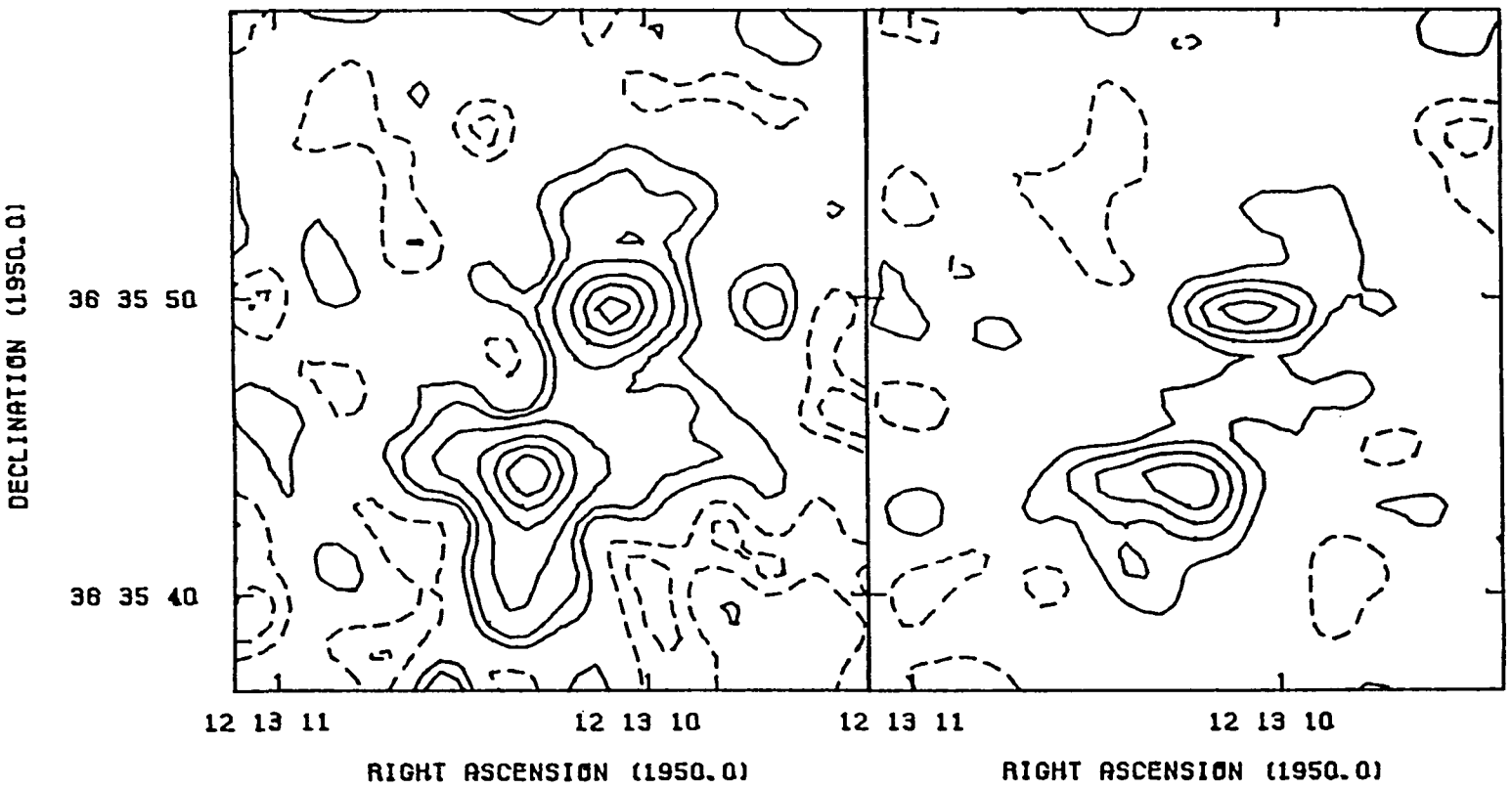
DECLINATION (1950.0)
36 35 50
36 35 40
12 13 11
12 13 10
RIGHT ASCENSION (1950.0)
12 13 11
12 13 10
RIGHT ASCENSION (1950.0)

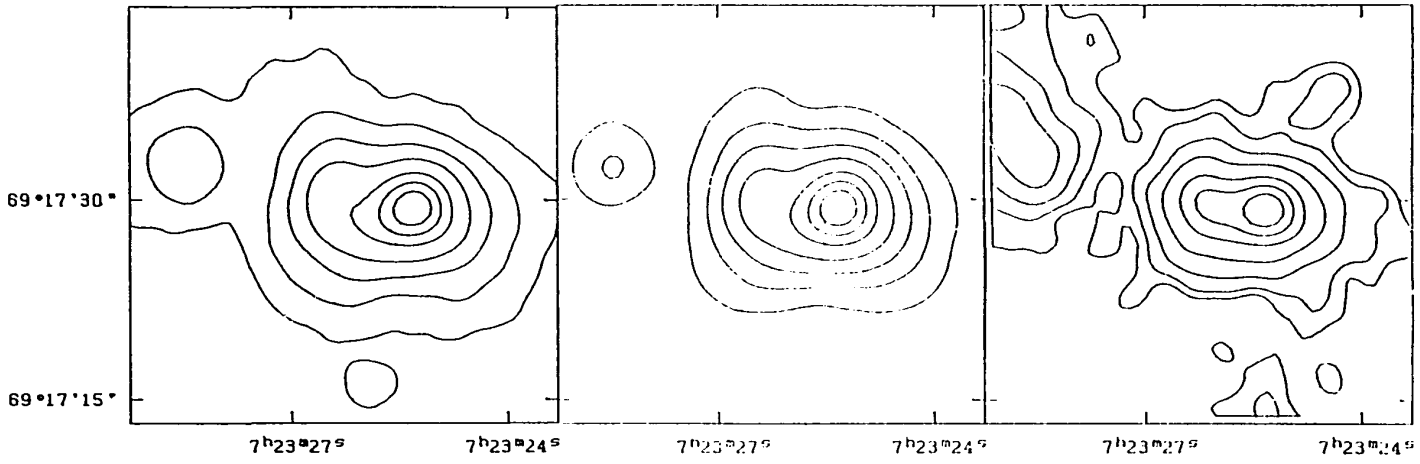

Figure 3.5 Optical Imaging of NGC 2363

Contour map representations of the video camera images of NGC 2363 in the light of Hα, λ5007, and the blue continuum. The nuclear positions as referred to in the text are marked in the Hα image. The contour levels are set at 80%, 60%, 40%, 20%, 10%, 5%, and 2% of the peak in each image.

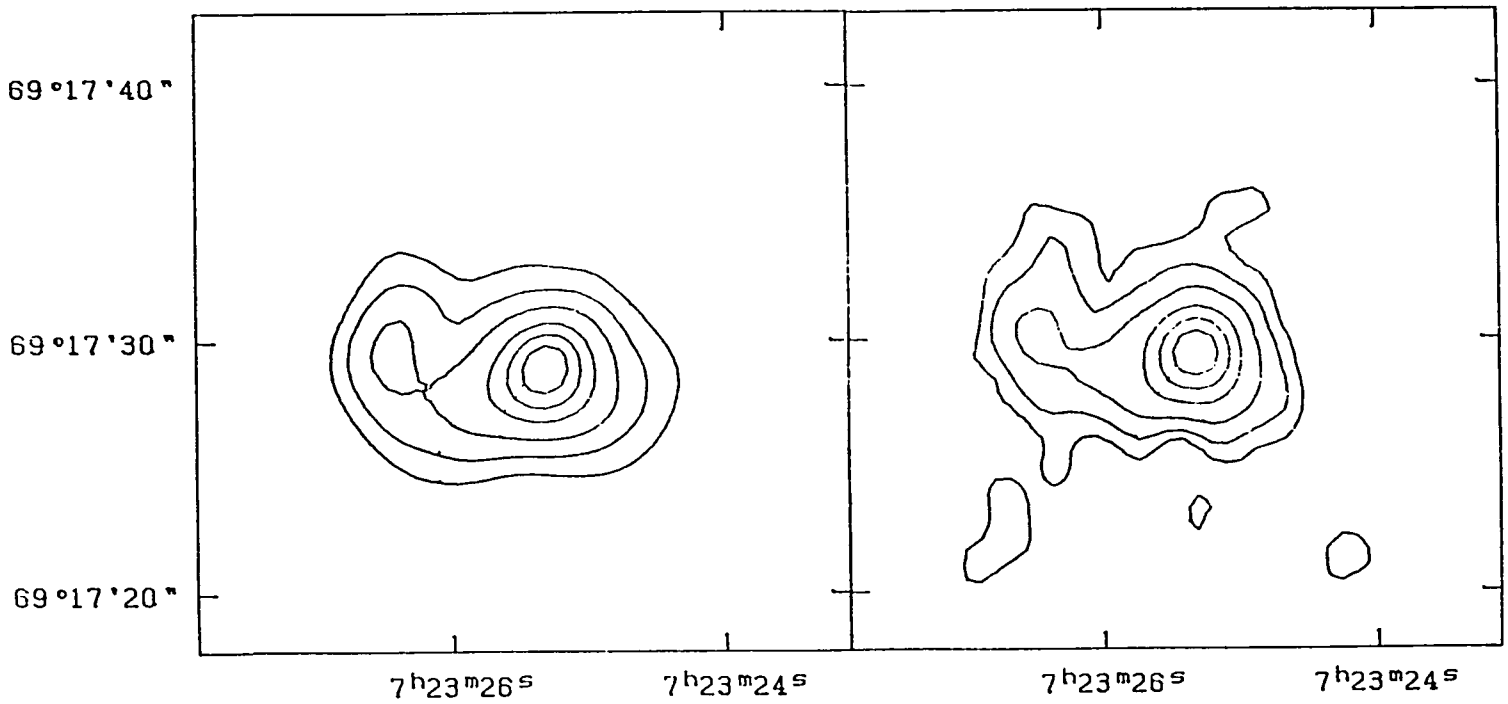

Figure 3.6 [O III] Imaging of NGC 2363

Contour map representations of the video camera images of NGC 2363 in the light of λ5007 and λ4363. The contour levels are set at 80%, 60%, 40%, 20%, 10%, and 5% of the peak in each map.

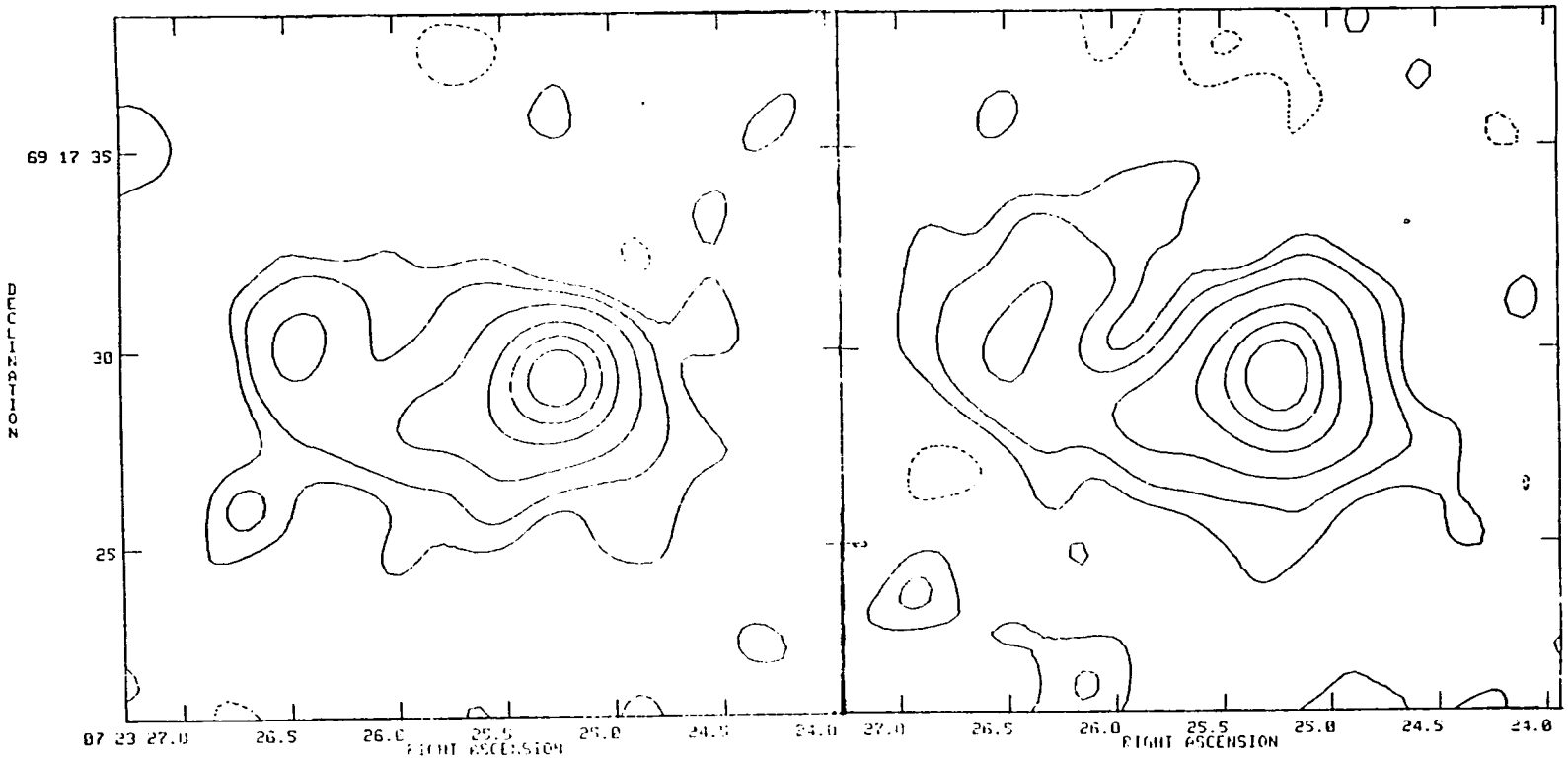

Figure 3.7 Radio Continuum Imaging of NGC 2363

Contour map representations of radio continuum images of NGC 2363. These are clean maps constructed with a 2 FWHM synthesized beam. The contour levels are set at 80%, 60%, 40%, 20%, 10%, and 5% of the peak in each image. Negative contours are dashed.

Note that the λ5007 emission is more concentrated than the Hα emission. Note also that the blue optical continuum in the eastern region is roughly one third of that in NGC 2363, but that the nebular emission is less by a factor of twenty.

Spectrophotometry

Tables 3.1, 3.2, and 3.3 list the reddening corrected emission line strengths normalized to Hβ given by :

$$\frac{I(\lambda)}{I(H\beta)} = \frac{F(\lambda)}{F(H\beta)} \times 10^{c(H\beta)f(\lambda)}$$

where F(λ) is the line flux outside of the earth's atmosphere, c(Hβ) is the logarithmic reddening correction at Hβ and f(λ) is the reddening function normalized at Hβ. The reddening function used is the same as used by Rayo, Peimbert, and Torres-Peimbert (1982) as derived from the normal extinction law (Whitford 1958). The values for c(Hβ) were calculated by comparing the Balmer line Hx/Hβ ratios for x = α, γ, δ, and 9 to the theoretically determined value (Brocklehurst 1971) and including an equivalent width of underlying stellar absorption of 0, 1, 2, 3, and 4 Angstroms. Since the theoretical Balmer decrement varies with temperature, an iterative method of solving for the temperature from the [O III] lines and then solving for c(Hβ) was used. For all of the spectra, the most suitable agreement was found for 2 Angstroms of underlying absorption, as in previous studies of GEHRs (e.g. Shields and Searle 1978). The values of c(Hβ) determined from the calculations for both

Table 3.1

NGC 5471 Line Fluxes and Physical Parameters

Line	Id	A		B		C		D		IRS		AL		BL		CL		DL	
3727	[O II]	1.32	.04	3.00	.11	2.04	.08	1.26	.05	1.56	.06	...	...	...	...	...	...	1.61	.08
3750	H 12	.021	.003	...	...	.013	.006	...	...	...	...	...	...	...	...	...	...	...	...
3770	H 11	.026	.003	.018	.004	.017	.004	.012	.004	...	...	...	...	...	...	...	...	...	...
3798	H 10	.037	.003	.038	.004	.030	.004	.034	.005	.023	.007	...	...	...	...	...	...	...	...
3835	H 9	.057	.003	.054	.004	.050	.004	.031	.004	.049	.007	...	...	...	...	...	...	...	...
3868	[Ne III]	.56	.02	.37	.01	.40	.01	.49	.02	.38	.02	...	...	...	...	...	...	.56	.04
3889	H 8 + He I	.20	.01	.19	.01	.19	.01	.17	.01	.19	.01	...	...	...	...	...	...	.13	.02
3967	H 7 + [Ne III]	.34	.01	.28	.01	.28	.01	.29	.01	.28	.01	.31	.01	...	...	...	...	.22	.04
4026	He I	.016	.003	.011	.004	.016	.004	.015	.005	.009	.006	.013	.005	...	...	.031	.008	.018	.006
4069	[S II]	.009	.006	.038	.004	.021	.004	.019	.006	.024	.007	.027	.007	.028	.008	.079	.014	...	...
4076	[S II]	.010	.005	.017	.003	.009	.003	...	...	...	...	...	...	...	...	...	...	...	...
4102	H 6	.25	.01	.25	.01	.26	.01	.22	.01	.22	.01	.26	.01	.25	.01	.29	.01	.25	.01
4340	H 5	.47	.01	.46	.01	.45	.01	.46	.01	.44	.01	.43	.01	.47	.01	.44	.01	.47	.01
4363	[O III]	.10	.003	.062	.003	.054	.004	.072	.005	.081	.004	.090	.003	.084	.003	.056	.002	.064	.003
4471	He I	.036	.002	.032	.002	.032	.004	.033	.004	.034	.007	.038	.003	.038	.005	.040	.004	.030	.004
4658	[Fe III]	.006	.002	.009	.002	...	...	...	...	...	...	...	...	...	...	...	...	...	...
4686	He II	.011	.003	.013	.002	...	...	.013	.004	...	...	...	...	...	...	...	...	...	...
4712	[Ar IV] + He I	.016	.004	.005	.001	...	...	.011	.004	...	...	...	...	...	...	...	...	...	...
4861	H 4	1.00	.01	1.00	.01	1.00	.01	1.00	.01	1.00	.02	1.00	.01	1.00	.01	1.00	.01	1.00	.01
4959	[O III]	2.21	.02	1.25	.02	1.44	.01	1.97	.02	1.90	.08	2.26	.03	1.49	.03	1.57	.02	1.90	.03
5007	[O III]	6.97	.04	3.92	.02	4.60	.03	6.22	.04	5.64	.11	6.82	.06	4.71	.05	4.64	.03	5.95	.05
5876	He I	.087	.005	.093	.004	.093	.004	...	...	.11	.01	.092	.003	.085	.003	.086	.003	.093	.004
6300	[O I]	.033	.003	.14	.005	.039	.004	...	...	.052	.004	.022	.001	.10	.01	.040	.002	.013	.001
6312	[S III]	.011	.002	.017	.002	.010	.002	...	...	.022	.004	.013	.001	.005	.002	.013	.001	.016	.001
6563	H 3	2.80	.11	2.79	.11	2.81	.11	...	...	2.73	.11	2.78	.11	2.79	.11	2.81	.11	2.80	.11
6584	[N II]	.061	.009	.13	.01	.16	.01	...	...	.17	.01	.077	.010	.16	.01	.17	.01	.091	.009
6678	He I	.021	.003	.024	.004	.020	.003	...	...	.019	.005	.021	.002	.022	.003	.026	.003	.029	.003
6716	[S II]	.081	.005	.26	.01	.15	.01	...	...	.11	.006	.082	.004	.24	.01	.14	.01	.091	.005
6731	[S II]	.060	.003	.22	.01	.12	.01	...	...	.10	.006	.071	.003	.19	.01	.11	.01	.073	.004
7065	He I	.024	.008	.016	.006	.036	.013	...	...	...	...	.021	.002	.027	.003	.014	.003	...	...
7136	[Ar III]	.051	.007	.040	.006	.055	.011	...	...	...	...	...	...	.063	.004	.046	.003	...	...
7281	He I	.006	.006	...	...	...	...	...	...	...	...	...	...	...	...	...	...	...	...
7320	[O II]	...	...	.036	.006	...	...	...	...	...	...	...	...	...	...	...	...	...	...
7330	[O II]	...	...	.029	.005	...	...	...	...	...	...	...	...	...	...	...	...	...	...
c(HB)		.54	.05	.51	.05	.33	.05	.21	.05	.07	.05	.18	.05	.18	.05	.25	.05	.00	.05
EW(HB)		297	...	238	...	245	...	105	...	217	...	244	...	223	...	206	...	139	...
T(O III)		12,850	150	13,450	250	12,050	300	11,950	300	13,000	300	12,500	150	14,150	350	12,050	200	11,650	200
ne(S II)		100	50	400	200	300	200	...	...	600	200	400	200	400	200	300	200	350	200
Teff		42,500	...	39,500	...	37,500	...	39,000	...	40,000	...	...	...	...	...	...	...	40,000	...

Table 3.2

NGC 4214 Line Fluxes and Physical Parameters

Line	Id	A		B		C		N		IRS		AL		BL		CL		NL	
3727	[O II]	3.31	.12	2.60	.10	3.17	.12	2.06	.15	2.86	.11	...	...	...	...	...	...	2.25	.15
3750	H 12	.016	.004	.016	.004	.009	.003	...	...	...	...	...	...	...	...	...	...	...	...
3770	H 11	.020	.004	.019	.004	.021	.003	...	...	...	...	...	...	...	...	...	...	...	...
3798	H 10	.036	.004	.035	.004	.033	.003	...	...	...	...	...	...	...	...	...	...	...	...
3835	H 9	.047	.004	.050	.004	.055	.004	...	...	.070	.014	...	...	...	...	...	...	...	...
3868	[Ne III]	.15	.01	.34	.01	.19	.01	.30	.03	.17	.02	...	...	...	...	...	...	...	...
3889	H 8 + He I	.17	.01	.19	.01	.18	.01	.069	.018	.13	.02	...	...	...	...	...	...	...	...
3967	H 7 + [Ne III]	.18	.01	.25	.01	.20	.01	.087	.014	.16	.01	...	...	...	...	.20	.01	.22	.04
4026	He I	.018	.004	.030	.005	.015	.003	.024	.013	...	...	...	...	...	...	.019	.007	...	...
4069	[S II]	.017	.004	.017	.005	.015	.003	.021	.019	.035	.012	.10	.01	.045	.018	.019	.001	...	...
4076	[S II]	.004	.003	.003	.004	.011	.002	...	...	...	...	...	...	...	...	...	...	...	...
4102	H 6	.23	.01	.24	.01	.24	.01	.13	.01	.20	.01	.31	.01	.29	.02	.27	.01	.17	.02
4340	H 5	.46	.01	.47	.01	.46	.01	.36	.02	.43	.01	.46	.01	.52	.01	.47	.01	.38	.01
4363	[O III]	.22	.003	.034	.004	.024	.002	.025	.007	.024	.006	.034	.003	.020	.003	.034	.002	.032	.006
4471	He I	.035	.003	.038	.003	.034	.002	...	...	.028	.010	.040	.006	...	...	.055	.004	.017	.012
4686	He II	...	...	...	...	.017	.003	...	...	...	...	...	...	...	...	...	...	...	...
4712	[Ar IV] + He I	.002	.003	...	...	...	...	...	...	...	...	...	...	...	...	...	...	...	...
4861	H 4	1.00	.01	1.00	.01	1.00	.01	1.00	.01	1.00	.02	1.00	.01	1.00	.01	1.00	.01	1.00	.01
4959	[O III]	.95	.01	1.40	.01	1.12	.01	1.19	.02	1.12	.05	1.12	.02	1.49	.02	1.27	.02	1.10	.02
5007	[O III]	3.02	.02	4.55	.03	3.52	.02	3.85	.05	3.41	.06	3.48	.03	4.69	.03	3.93	.03	3.56	.04
5876	He I	.11	.01	.10	.01	.097	.003	.091	.007	.12	.01	.11	.01	.11	.01	.11	.01	.11	.01
6300	[O I]	.013	.004	.021	.002	.024	.002	.014	.004	.031	.004	.018	.002	.016	.002	.015	.002	.027	.003
6312	[S III]	.010	.003	.013	.001	.013	.002	.015	.003	.018	.004	.014	.002	.014	.002	.012	.002	...	...
6563	H 3	2.85	.11	2.85	.11	2.86	.11	2.86	.22	2.90	.12	2.88	.11	2.97	.12	2.88	.11	2.98	.12
6584	[N II]	.21	.01	.15	.01	.16	.01	.17	.02	.30	.02	.20	.01	.17	.01	.18	.01	.22	.02
6678	He I	.036	.007	.028	.003	.030	.003	.032	.007	...	...	.021	.002	.020	.002	.037	.003	.022	.004
6716	[S II]	.20	.01	.14	.01	.14	.01	.15	.01	.22	.01	.16	.01	.13	.01	.14	.01	.21	.01
6731	[S II]	.13	.01	.11	.01	.10	.01	.11	.01	.13	.01	.11	.01	.11	.01	.12	.01	.15	.01
7065	He I	.021	.010	.023	.005	.030	.005	.027	.011	...	...	.034	.003	.015	.004	.022	.004	...	...
7136	[Ar III]	.083	.012	.086	.006	.086	.006	.067	.011	...	...	.10	.01	.090	.006	.086	.005	...	...
7320	[O II]	.032	.008	.014	.007	...	...	.016	.007	...	...	...	...	...	...	...	...	...	...
7330	[O II]	.017	.005	.008	.004	...	...	.018	.006	...	...	...	...	...	...	...	...	...	...
c(HB)		.36	.05	.49	.05	.35	.05	.21	.10	.13	.05	.31	.05	.51	.05	.38	.05	.23	.05
EW(HB)		153	...	234	...	236	...	22	...	78	...	178	...	167	...	189	...	30	...
T(O III)		10,250	500	10,350	350	10,000	300	9,900	900	10,100	900	11,200	300	8,800	500	10,800	200	10,950	750
ne(S II)		0	100	150	150	0	100	130	300	0	100	0	100	450	300	350	200	50	150
Teff		37,500	...	40,000	...	40,000	...	38,000	...	38,000	...	...	...	...	...	...	...	36,500	...

Table 3.3

NGC 2363 Line Fluxes and Physical Parameters

Line	Id	A		B		C		IRS		2366 II	
3727	[O II]	.44	.02	.83	.03	1.00	.04	.59	.05	1.06	.09
3770	H 11	.026	.003	.024	.003	.027	.003	...	...	...	...
3798	H 10	.037	.003	.040	.003	.042	.003	.027	.005	.060	.026
3835	H 9	.054	.003	.058	.003	.061	.004	.049	.005	.093	.026
3868	[Ne III]	.57	.02	.48	.02	.51	.02	.47	.02	.21	.04
3889	H 8 + He I	.19	.01	.18	.01	.20	.01	.20	.01	.093	.060
3967	H 7 + [Ne III]	.30	.01	.27	.01	.29	.01	.30	.01	.12	.04
4026	He I	.015	.002	.012	.003	.014	.002	...	...	...	...
4069	[S II]	.004	.002	...	...	.009	.002	...	...	...	...
4076	[S II]	.001	.001	...	...	.004	.002	...	...	...	...
4102	H 6	.26	.01	.25	.01	.28	.01	.24	.01	.23	.03
4340	H 5	.47	.01	.46	.01	.47	.01	.46	.02	.38	.04
4363	[O III]	.15	.003	.12	.003	.11	.003	.145	.006	.138	.024
4471	He I	.034	.002	.030	.002	.037	.002	.034	.008	...	...
4686	He II	...	...	.020	.002	.006	.002	...	...	...	...
4712	[Ar IV] + He I	.023	.004	.014	.002	.008	.003	...	...	...	...
4740	[Ar IV]	.015	.004	...	...	...	...	...	...	...	...
4861	H 4	1.00	.01	1.00	.01	1.00	.01	1.00	.03	1.00	.06
4959	[O III]	2.48	.03	2.07	.01	1.92	.02	2.31	.12	1.71	.09
5007	[O III]	7.70	.05	6.39	.04	6.01	.04	7.13	.19	5.24	.24
5876	He I	.097	.003	.094	.003	.087	.003	.108	.005	...	...
6300	[O I]	.007	.001	.010	.001	.018	.002	.010	.002	...	...
6312	[S III]	.012	.001	.014	.001	.014	.002	.016	.002	...	...
6563	H 3	2.77	.11	2.77	.11	2.77	.11	2.74	.12	...	...
6584	[N II]	.022	.006	.030	.007	.036	.007	.090	.014	...	...
6678	He I	.022	.001	.024	.002	.020	.002	.019	.004	...	...
6716	[S II]	.032	.002	.052	.002	.078	.004	.046	.003	...	...
6731	[S II]	.023	.001	.039	.002	.047	.002	.039	.003	...	...
7065	He I	.026	.002	.015	.002	.022	.004	...	...	...	...
7136	[Ar III]	.046	.003	.051	.003	.055	.005	...	...	...	...
7281	He I	.005	.001	.004	.001	.006	.004	...	...	...	...
7320	[O II]	.008	.001	.011	.002	.015	.003	...	...	...	...
7330	[O II]	.008	.001	.010	.002	.014	.002	...	...	...	...
c(HB)		.39	.05	.56	.05	.00	.05	.27	.05	.00	.05
EW(HB)		518	...	251	...	404	...	331	...	79	...
T(O III)		14,750	150	14,250	150	14,550	150	15,000	350	17,000	1600
ne(S II)		0	100	100	250	0	100	500	350	...	...
Teff		47,500	...	43,000	...	43,000	...	47,000	...	48,000	...

cases of no underlying absorption and 2 Angstroms equivalent width of underlying absorption are presented in Tables 3.4, 3.5, and 3.6. The formal errors for c(Hβ) derived from the uncertainty in the line strength ratios were usually unreasonably small, so .05 was adopted as a conservative minimum uncertainty in c(Hβ) for calculating in the reddening corrected line strengths. The values of c(Hβ) used to make the reddening corrections for each spectrum were the uncertainty weighted means of all of the c(Hβ) values measured for that spectrum. For the KPNO IIDS scans, c(Hβ) was determined from the blue grating tilt and used for both the blue and red scans. The intensities of the red scans were scaled to the blue scans by fixing the Hα/Hβ ratio to be the theoretically determined value (Brockelhurst 1971).

Three physical parameters are derived from the line fluxes and included in tables 3.1, 3.2, and 3.3. Electron temperatures are derived from the temperature sensitive [O III] line ratio (λ5007 + λ4959/λ4363) following Seaton (1975). Approximate electron densities have been calculated following Pradhan (1978). The main source of uncertainty in the density estimates is the uncertainty in temperature. An estimate of the stellar effective temperature has been made using the method of Kunth and Sargent (1983). In this method, an estimate of the oxygen abundance is made from the strengths of the [O II] and [O III] lines relative to Hβ. Then the stellar effective temperature can be estimated by inspection of figure 6 in Stasinska (1980) in which T_{eff} is plotted as a function

Table 3.4

Values for c(Hβ) for NGC 5471

	KPNO					Mt. Lemmon			
	A	B	C	D	IRS	A	B	C	D
no underlying absorption									
Hα/Hβ					.04	.17	.19	.25	-.01
					(.02)	(.01)	(.01)	(.01)	(.01)
Hγ/Hβ	.56	.57	.47	.28	.28	.47	.21	.48	-.01
	(.02)	(.02)	(.03)	(.03)	(.06)	(.03)	(.04)	(.03)	(.04)
Hδ/Hβ	.66	.64	.34	.55	.43	.19	.31	.05	.11
	(.03)	(.03)	(.03)	(.05)	(.08)	(.05)	(.07)	(.07)	(.10)
H9/Hβ	.93	.99	.93	1.54	.70				
	(.07)	(.10)	(.12)	(.21)	(.20)				
2 angstroms EW underlying absorption									
Hα/Hβ					.03	.16	.18	.24	-.02
					(.02)	(.01)	(.01)	(.01)	(.01)
Hγ/Hβ	.52	.51	.42	.17	.21	.39	.15	.40	-.10
	(.02)	(.02)	(.03)	(.03)	(.07)	(.03)	(.04)	(.03)	(.04)
Hδ/Hβ	.58	.52	.23	.29	.32	.07	.20	-.07	-.06
	(.02)	(.03)	(.03)	(.05)	(.07)	(.05)	(.06)	(.06)	(.09)
H9/Hβ	.55	.47	.37	.27	.20				
	(.05)	(.07)	(.09)	(.09)	(.15)				

Table 3.5

Values for c(Hβ) for NGC 4214

	KPNO					Mt. Lemmon			
	A	B	C	N	IRS	A	B	C	N
no underlying absorption									
Hα/Hβ					.15	.34	.54	.40	.29
					(.02)	(.01)	(.01)	(.01)	(.01)
Hγ/Hβ	.40	.49	.39	1.07	.40	.40	.18	.37	.93
	(.02)	(.03)	(.02)	(.12)	(.09)	(.04)	(.04)	(.03)	(.10)
Hδ/Hβ	.59	.67	.48	1.65	.69	-.08	.26	.31	1.17
	(.04)	(.04)	(.03)	(.21)	(.14)	(.06)	(.11)	(.07)	(.19)
H9/Hβ	1.03	1.08	.80	...	.20				
	(.12)	(.12)	(.09)	...	(.30)				
2 angstroms EW underlying absorption									
Hα/Hβ					.12	.32	.53	.39	.22
					(.02)	(.01)	(.01)	(.01)	(.01)
Hγ/Hβ	.33	.44	.34	.37	.25	.33	.11	.31	.39
	(.02)	(.03)	(.02)	(.09)	(.08)	(.04)	(.04)	(.03)	(.08)
Hδ/Hβ	.43	.57	.38	.06	.39	-.27	.11	.20	.11
	(.03)	(.04)	(.02)	(.09)	(.12)	(.06)	(.11)	(.06)	(.11)
H9/Hβ	.37	.58	.35	...	-.45				
	(.08)	(.08)	(.06)	...	(.19)				

Table 3.6

Values for c(Hβ) for NGC 2363

	KPNO				
	A	B	C	IRS	II
no underlying absorption					
Hα/Hβ				.26	
				(.03)	
Hγ/Hβ	.42	.65	.03	.34	.75
	(.02)	(.02)	(.02)	(.09)	(.37)
Hδ/Hβ	.45	.65	-.10	.46	.28
	(.02)	(.03)	(.02)	(.08)	(.30)
H9/Hβ	.88	.93	.30	.92	-.34
	(.07)	(.07)	(.08)	(.17)	(.43)
2 angstroms EW underlying absorption					
Hα/Hβ				.25	
				(.03)	
Hγ/Hβ	.39	.58	-.02	.30	.49
	(.02)	(.02)	(.02)	(.09)	(.34)
Hδ/Hβ	.40	.55	-.17	.39	-.03
	(.02)	(.03)	(.02)	(.08)	(.26)
H9/Hβ	.62	.52	-.03	.49	-.91
	(.06)	(.06)	(.06)	(.13)	(.29)

of oxygen abundance and electron temperature for a grid of model H II regions.

Radio Continuum Flux Measurements

Table 3.7 contains measurements of the radio continuum fluxes for the three GEHRs listed in the last tables. The fluxes at λ6 cm and λ21 cm were measured from images constructed with a 3 FWHM synthesized beam, and represent integrations over various areas in the images. The uncertainties quoted with each measurement are estimates and not 1 σ errors in the formal sense. These uncertainties were determined by changing the area of integration and gauging the sensitivity of the flux measurement to the aperture size. The main source of error for the measurements of the total regions is the confusion in the background due to other sources. The main sources of error for the nuclear positions are the diffuse emission from the halo and the close proximity of the other nuclei. The spectral indices were determined by measuring the ratio of the fluxes in equivalent areas. Again, errors were determined from the sensitivity of the ratio to changes in integration area. For the nuclear positions, the spectral index measurements were much less sensitive to integration areas than the fluxes.

Table 3.7

Radio Continuum Flux Measurements

region	1450MHz	4885MHz	α
N5471	13.7 (1.0)	9.2 (1.0)	-.25 (.1)
A	5.2 (.8)	3.7 (.8)	-.3 (.1)
B	4.4 (.8)	2.5 (.5)	-.5 (.1)
C	1.4 (.6)	1.4 (.6)	-.1 (.2)
N4214	3.4 (.5)	4.0 (.5)	.1 (.1)
A	.6 (.2)	.5 (.2)	-.2 (.2)
B	1.6 (.3)	1.8 (.3)	.1 (.2)
C	1.2 (.3)	1.5 (.3)	.1 (.2)
N2363	15.9 (2.0)	9.8 (1.0)	-.4 (.1)
A	8.5 (2.0)	5.1 (.8)	-.4 (.05)
B	2.9 (.9)	1.5 (.4)	-.5 (.1)
C	2.2 (1.0)	1.6 (1.0)	-.25 (.1)

Chapter IV Reddening and Extinction in GEHRs

Reddening and Extinction Measurement Techniques

The range of particle sizes of interstellar dust grains extends to within an order of magnitude of the size of the wavelengths of optical light. Because of this, light is scattered or absorbed as it passes through the dust, causing extinction. This extinction is wavelength dependent, and this dependence produces a reddening as optical light passes through the interstellar medium. In order to correctly deduce the intrinsic properties of a GEHR, it is necessary to determine the effects of extinction and reddening by dust. A significant ambiguity can arise concerning the location of the dust; if the dust is internal to the GEHR, the effect on the optical spectrum will be different from the effect of a 'screen' of dust that lies between the observer and the GEHR. The importance of understanding the effect of the dust is two-fold: 1.) Because of the wavelength dependence of the extinction, one must accurately determine the reddening before using optical line strength ratios to determine physical parameters such as temperature, density, and chemical abundances. 2.) An accurate measurement of the extinction is necessary for a calculation of the true luminosity of the GEHR. Moreover, internal dust can affect the internal dynamics and ionization structure of a GEHR.

There are two commonly used methods for studying the effects of dust on H II region optical spectra. The first is based on the measurement of the relative strengths of the Balmer emission lines. These have been calculated for a gas that is optically thin to Balmer emission by Brocklehurst (1971). The Balmer line ratios show a very weak dependence on temperature in the range significant for H II regions. Thus, comparing observed line ratios to theoretically predicted line ratios yields a measurement of the relative extinction. If this measurement is combined with the assumption of a universally applicable reddening law (e.g. Whitford 1958, Schild 1977), then the total extinction at each wavelength can be determined from a single Balmer line pair. The measurement of Balmer emission line strengths can be affected by Balmer absorption lines in the underlying stellar continuum, but, it is possible, in principle, to solve simultaneously for the strength of the underlying absorption and the total extinction, by using more than one Balmer line pair.

A second method for determining the extinction of H II regions is based on the premise that at sufficiently long wavelengths there is no extinction. The radio continuum emission due to thermal bremsstrahlung for an H II region has been investigated by Mezger and Henderson (1967) and Rubin (1968). Following the notation of Lequeux (1980), the rate of production of Lyman continuum photons (Nc) can be expressed in terms of the observed free-free radio continuum emission:

$$\frac{Nc}{photon/s} = 7.54 \times 10^{46} \left(\frac{\nu}{GHZ}\right)^{0.1} \left(\frac{Te}{10^4K}\right)^{-.45} \frac{S\nu}{Jy} \left(\frac{D}{kpc}\right)^2$$

This rate can also be calculated in terms of the Hβ emission observed:

$$\frac{Nc}{photon/s} = 2.47 \times 10^{56} \frac{I(H\beta)}{erg/cm^2/s} \left(\frac{Te}{10^4K}\right)^{-0.09} \left(\frac{D}{kpc}\right)^2$$

Combining the above two equations results in the following predicted ratio of observed radio continuum to Hβ flux:

$$\frac{S\nu/Jy}{I(H\beta)/erg/cm^2/s} = 3.28 \times 10^9 \left(\frac{\nu}{GHz}\right)^{-0.1} \left(\frac{Te}{10^4K}\right)^{0.34}$$

From this last equation we have a direct way to measure the total extinction at Hβ.

These two methods have been found in good agreement for galactic H II regions (Gebel 1968) and planetary nebulae (Osterbrock 1974), although Hawley and Duncan (1976) do note a large range in selective to total extinction from observations of planetary nebulae. In contrast, when these methods are applied to GEHRs, quite discrepant results are discovered. The discrepancy for GEHRs has been summarized by Israel and Kennicutt (1980). For 29 extragalactic H II regions studied, they found that the extinction as measured from the Balmer line ratios (optical method) was an average of 1.2 magnitudes less than that measured via the radio strength to Balmer line strength comparison (radio-optical method).

There are several potential sources of extinction for GEHR observations. First, the effects of galactic extinction must be accounted for. This is normally done by referring to a standard galactic extinction law (e.g. Sandage 1973, de Vaucoleurs, de Vaucoleurs and Corwin 1976). Secondly, there can be foreground dust in the host galaxy of the GEHR. Finally, there can be dust mixed within the GEHR itself.

If the dust external to the GEHR is distributed in a uniform screen across the face of the GEHR, and, if the dust is of a similar chemical make-up and size distribution as the dust observed in our galaxy (i.e. obeys the standard galactic reddening law), then the two methods used for determining the interstellar extinction should be in good agreement. However, if the dust is clumpy on size scales larger than the allowed spatial resolution of the observations, a discrepancy will arise between the two measurements. The radio continuum measurements will detect the entire ionized gas, and the radio-optical method will measure the total extinction. On the other hand, the optical measurements will be weighted toward those regions which suffer the least extinction and the optical method will underestimate the extinction for the entire GEHR. Hawley and Duncan (1976) ran a series of numerical calculations that showed that the discrepancy in the measured extinction can be as large as a factor of 2 if only 30 percent of the nebula is covered by an optically opaque material. Note that the value of extinction derived from the optical

method will be the more appropriate value for dereddening the optical spectrum. If there is dust internal to the GEHR, the situation will be comparable to the clumpy distribution of foreground dust,: the radio-optical method will correctly measure the total extinction, but the optical method will underestimate the total extinction.

There is no unambiguous way to attribute the reddening discrepancy for GEHRs to clumpy foreground dust or internal dust. For a simplistic model of a spherical, uniform density, H II region, the two can be distinguished. For the case of internal dust, the discrepancy should be greatest in the center where the light path length is the longest and should disappear at the edges of the H II region. Clumpy foreground dust should not correlate with the structure of the H II region, and therefore the reddening attributed to foreground dust will vary randomly across the face of the GEHR. This admittedly simplistic model may be used as a starting point in determining the influence of internal versus external dust. If the reddening discrepancy correlates with region structure, then it may be evidence of internal dust. Conversely, no correlation between region structure and the reddening discrepancy argues for external clumpy dust.

The Observations

The extinction in GEHRs has been studied via the optical method in two different ways. Optical spectrophotometry allows the simultaneous measurement of several Balmer lines. The measurements represent averages over an area represented by the convolution of the seeing disk with the instrument aperture. In this study, both small apertures (~ 4") and a large aperture (23") were used for measurements. Spatial variations are noted by comparing the results for small aperture measurements and different positions, or by comparing the small aperture results with the global mean as measured by the large aperture. Narrow band optical images in the light of Hα and Hβ allow a point by point evaluation of the reddening with the resolution of the seeing disk. The Hα images can then be compared with radio continuum images of a comparable spatial resolution in order to determine the extinction via the radio-optical method.

The determination of c(Hβ), the logarithmic reddening correction at Hβ, from the optical spectroscopy has been described, and the results tabulated in chapter III. The results from the image ratios will be described and presented here.

Producing a map of the Hα/Hβ ratio is as simple as dividing the two continuum-free images. Unfortunately, there are complications that lead to less than satisfactory results for this simple procedure. A first consideration is the potential for differences in the spatial resolution of the two images. Changes in the atmospheric conditions can cause the seeing to change over the course of a night,

and this must be corrected for. The seeing was measured by fitting two dimensional Gaussian profiles to stars in each of the continuum frames. In most cases, there were no measurable changes in the seeing over the course of the observations of one object (usually less than two hours). In the few cases where the 2 arc minute field of view did not contain a star of sufficient intensity to allow a seeing measurement, the stellar continuum of the H II region itself was used.

The second problem encountered in making image ratio maps is the finite signal to noise in the images. In those regions of the image where the signal to noise ratio is less than or comparable to unity, the ratio image is rather messy. Two things can be done to reduce this problem. The first action is to increase the signal to noise ratio in the maps. Since the average image was taken during 2" (FWHM ~ 4 pixels) seeing conditions, convolving the image with a smoothing function of area less than the seeing disk will decrease the uncorrelated pixel-to-pixel r.m.s. fluctuations in the map without a significant loss in spatial resolution. For example, smoothing an image with a seeing disk of FWHM of 2" with a two dimensional Gaussian of FWHM of 1.5" results in an image seeing disk of FWHM of 2.5" (a loss in spatial resolution of 25 percent), and a decrease in the r.m.s. noise in the blank sky parts of the image by nearly a factor of 5. Also, in this smoothing process, any differences in seeing between the two images can be partially compensated for.

Finally, the ratio map can be made presentable by blanking all areas of the ratio image where the signal to noise ratio in the smoothed emission line images is below a threshold value. A reasonable cutoff is two times the r.m.s. variation in the blank sky regions of the smoothed maps.

Comparing the optical images with the radio maps also presents difficulties. There is a large inherent difference between the response function of an optical imaging device and that of a radio interferometer array. The response function for the optical imaging detector is dominated by the effects of the atmosphere ('seeing'). For the dynamic range of the video camera images, the response function is well described by a two dimensional Gaussian. The response function of a multi-element interferometer is very dependent upon how the observed visibilities are transformed into a surface brightness map. The primary concern for this discussion is the shape of the synthesized beam. This is affected by the completeness of sampling at different spatial frequencies, the type of Fourier transform used to produce the map, and how the observed data is weighted.

Another difficulty associated with comparing optical and radio images is the fact that some of the radio signal may be 'invisible' to the radio interferometer array. The minimum antenna separation in the interferometer sets an upper limit on the size scale of structures that can be detected. For the scaled array observations

in the A/B configuration for λ20/λ6 cm, this upper limit is about 25". Therefore, diffuse emission of this size scale or larger will not be detected. The 'missing flux' problem can be deceptive. Fortunately the major effect is to underestimate the radio surface brightness of faint, extended structure, whereas the regions of primary interest here are small, bright ones. One way to assess the effects of missing shorter spacings is to compare the total flux measurements with total flux measurements from interferometric observations with shorter spacings, or single disk measurements. The single dish measurements are not reliable for this purpose because quite frequently they are contaminated by emission from background sources. When possible, such comparisons will be made.

Since the optical response function is relatively simple and well behaved, and the radio response function is just the opposite, the natural course to take is to try to make adjustments to the radio map to allow a straightforward comparison to the optical map. Given the limited amount of time awarded on the VLA for this project, the ideal goal of a full sampling of all spatial frequencies was not possible. Nonetheless, the 'wye' shape of the VLA affords good coverage in even very short observations. Figure 4.1 shows the coverage for a typical observation. By choosing to construct a map using a fast Fourier transform (FFT), weighting functions can be employed that artificially improve the sampling coverage.

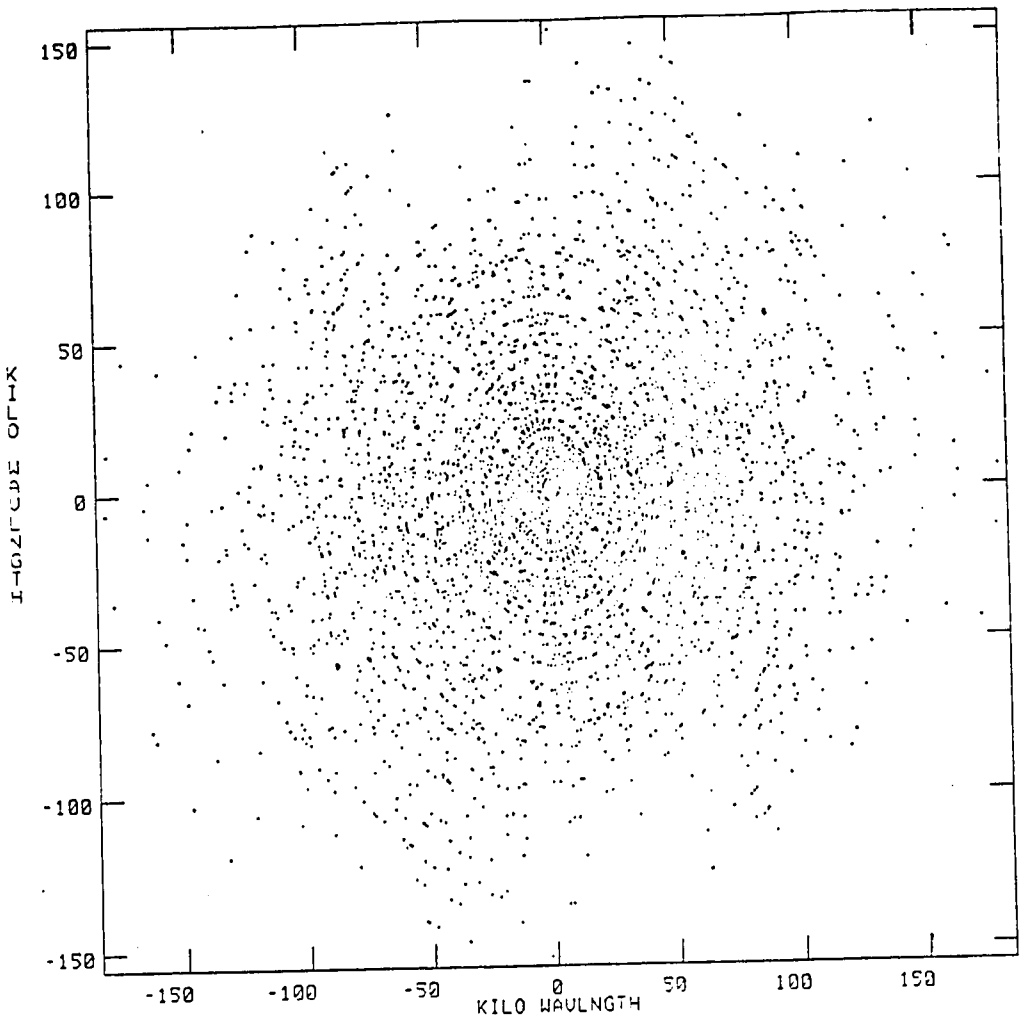

Figure 4.1 Sample UV Coverage

A plot of the sampling of the spatial frequencies for a two hour integration of NGC 2363. The plot represents one tenth of the total visibilities measured for the observation. Note the relative lack of coverage for the areas of the plot corresponding to the longest baselines.

Specifically, uniform weighting of the data and application of a taper will yield a beam shape more closely approximating a Gaussian and reduce sidelobe structure. If the sidelobe level is still larger than or comparable to the r.m.s. fluctuations in the map, then the adverse effects of the sidelobes can be effectively removed by using the CLEAN algorithm first developed by Hogbom (1974) and later based on an FFT by Clark (1980). After these several steps of data manipulation, it is possible to check the synthesized beam to determine the propriety of a direct comparison of the radio map with the optical image. For all comparisons in this study, the resultant synthesized clean beam is approximated very well by a two-dimensional Gaussian.

Individual Objects

A.) NGC 5471

Figure 4.2 shows the Hα/Hβ ratio map for NGC 5471. The Hα/Hβ map is normalized to the ratio obtained with the large aperture IRS observation. The contour levels are set at increments of 15 percent of the global ratio with negative contours dashed and positive contours solid. In this way, solid contours should represent increased reddening. The most striking features in the Hα/Hβ map are the strongly reddened areas in the center and the southwest.

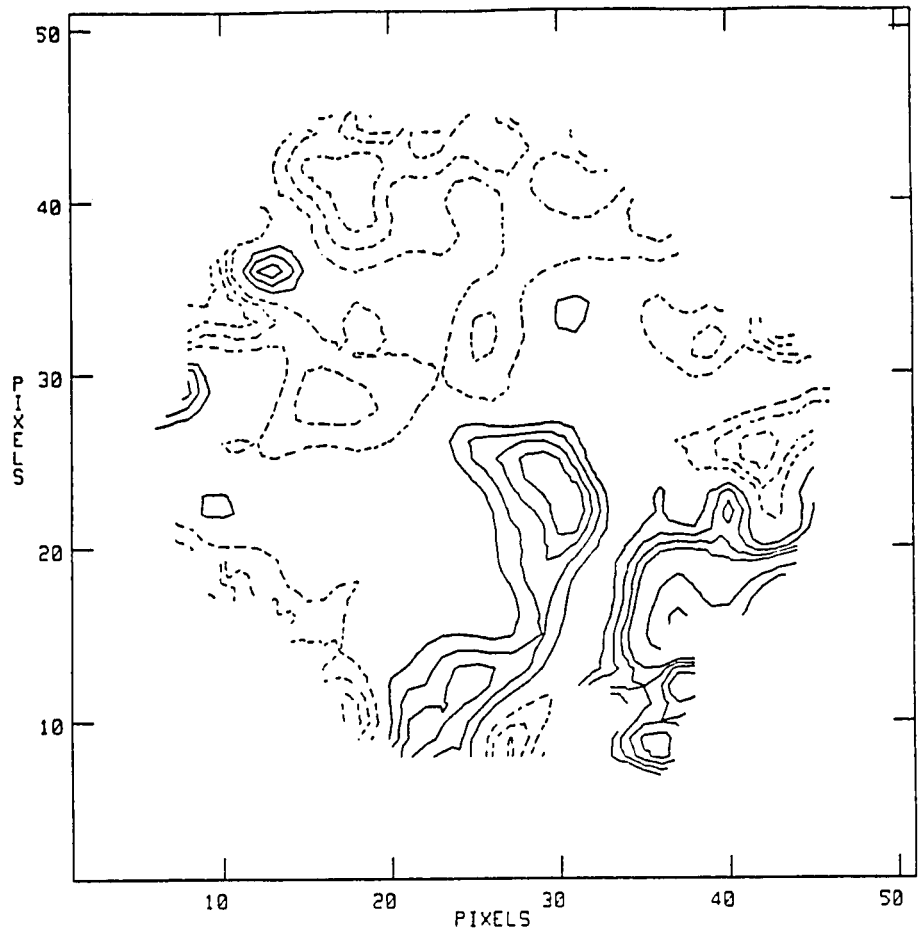

4.2 Hα/Hβ Ratio Map for NGC 5471

A contour map representation of the Hα/Hβ ratio for NGC 5471. The solid contours are positive and the dashed contours are negative. The image has been offset so that the zero point in the map corresponds to the image mean of 3.0. The contour intervals correspond to intervals of 5% of the image mean up to 20 Percent, and additional levels are placed at +40%, +60%, and +80%.

The contour map of the Hα/Hβ ratio does not present the error associated with this ratio. Figure 4.3, which shows the ratio and error bars at constant declination slices, was produced as follows. A map of the error corresponding to the ratio at each pixel was calculated using the CORMS routine available in the NRAO AIPS system. This error map was then added to and subtracted from the ratio map, and slices were taken through all three maps. The solid lines represent the Hα/Hβ ratio, the short dashed lines represent the associated 1 σ errors, and the line of long dashes shows the theoretical case B value for a gas at 12,000K. The dust lane appears prominently, but in most places the Hα/Hβ ratio shows little sign of significant amounts of reddening.

Figure 4.4, the Hα/λ6 cm ratio map, is less extensive due to the lower signal to noise ratio in the λ6 cm map. In this map contours are set at 5 percent levels. The Hα/λ6 cm map is very different from the Hα/Hβ map. The radio continuum is relatively strong in the northeast corner. This corresponds to the position of nucleus B. The radio continuum at this position is definitely nonthermal and it is most certain that the enhanced radio continuum is due to the presence of a supernova remnant (SNR) (see chapter VI). The λ6 cm emission is relatively weak (below the S/N cutoff used when producing the map) at the strongly reddened central position identified in the Hα/Hβ map, so that the map does not cover the entire region. However, there is evidence that the Hα/λ6 cm ratio is decreasing near

Figure 4.3 Hα/Hβ Slices for NGC 5471

Slices in constant declination of the Hα/Hβ map for NGC 5471. The slices correspond to the declinations of nuclei B and C, nucleus D, nucleus A, and nucleus E. The solid lines show the actual ratio and the short dashed lines show the one sigma error bars in the ratio. The horizontal dashed lines show the theoretical Hα/Hβ value for a temperature of 12,000 K.

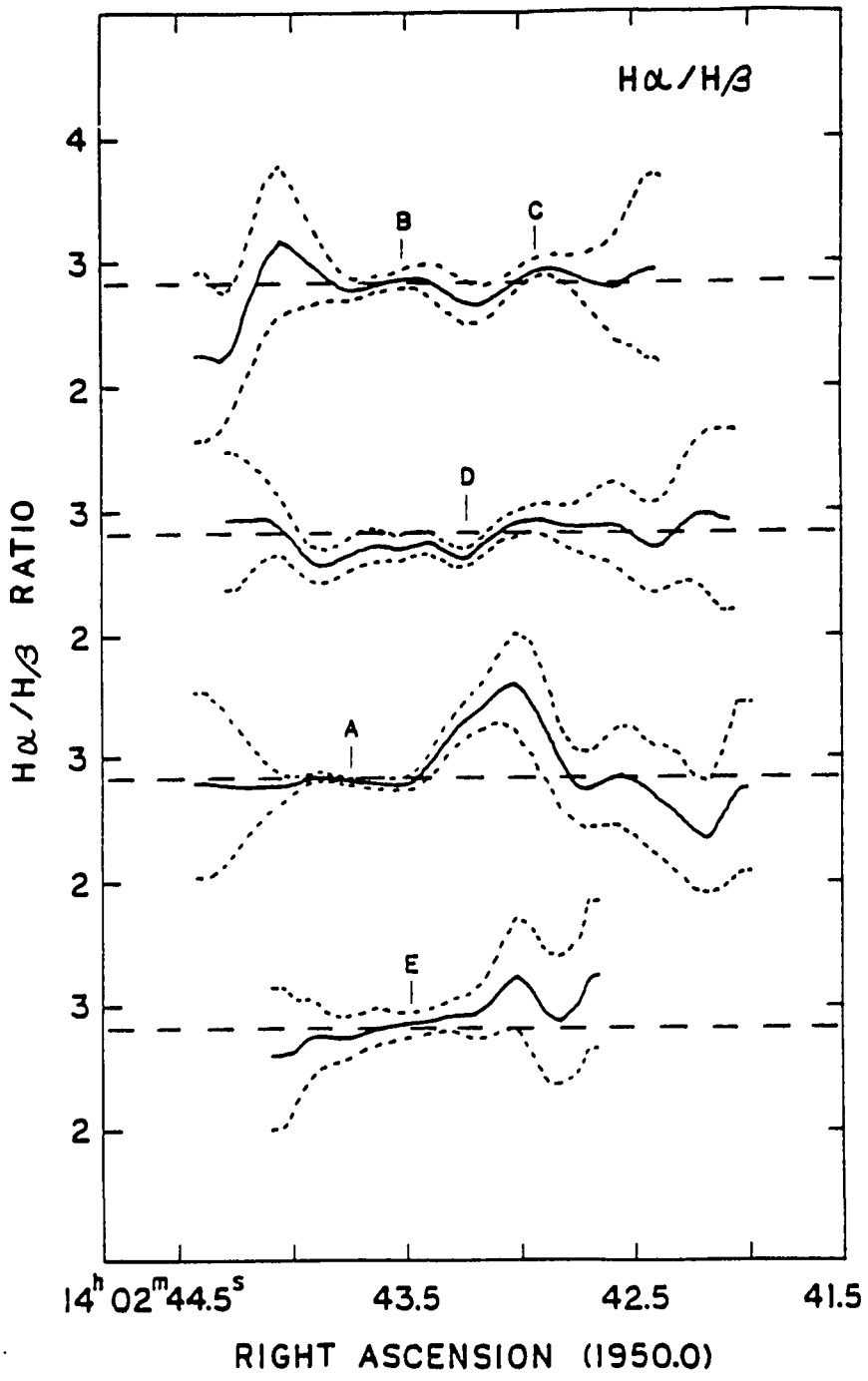
Hα/Hβ
B
C
D
A
E
4
3
2
3
2
3
2
3
2
Hα/Hβ RATIO
14h 02m 44.5s
43.5
42.5
41.5
RIGHT ASCENSION (1950.0)

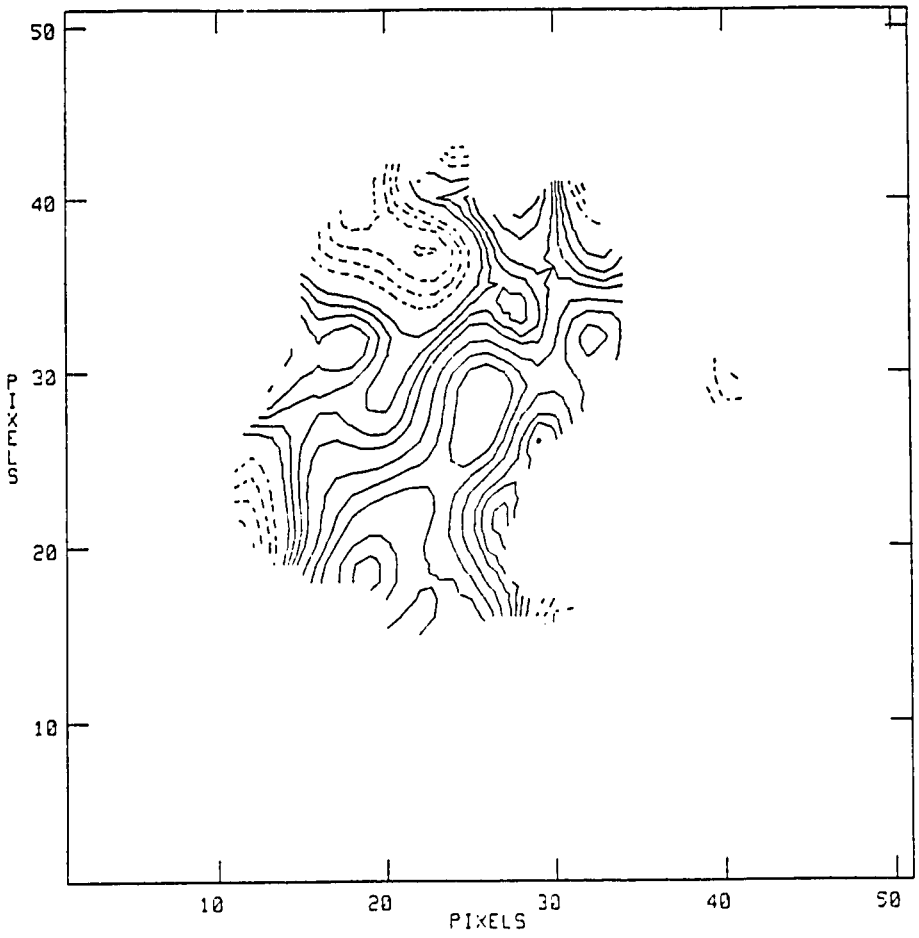

Figure 4.4 Hα/λ6 cm Ratio Map for NGC 5471

A contour map representation of the Hα/λ6 cm map for NGC 5471. Positive contours are solid and dashed contours are negative. The map has been offset such that the zero point corresponds to the image mean. Contour levels are set at intervals of 5 percent of the image mean up to 20 percent, with additional levels at +30%, +40%, +50%, +70% and + 90%.

this position. This would be the expected trend for foreground reddening. The most notable fact is the absence of a correlation between details in the two ratio maps. In a simple screen model interpretation, the negative contours in the Hα/Hβ map should correspond to the positive contours in the companion Hα/λ6 cm map. No such trend is noted.

The one simplistic test of internal versus external dust proposed appears to favor external dust for NGC 5471. Under the assumptions stated, evidence of internal dust would appear in the form of increased reddening or extinction at the positions of the nuclei. There is no strong evidence for differences of this nature. To investigate this possibility further, flux measurements were made with a series of concentric apertures at each of the nuclear positions in the video camera images. For nuclei A, B, and C, the Hα/Hβ ratio decreased with increasing aperture size. The measurements for nuclei D and E were contaminated by the close proximity of the strongly reddened central region. The observed differences were small (about 10 percent less in 6" aperture than in a 3" aperture), and, as such, may be susceptible to systematic errors, but the trend is suggestive. Comparing the Mt. Lemmon and KPNO small aperture spectrophotometry shows that c(Hβ) is generally smaller for the larger apertures, again confirming this trend (see table 3.4).

In summary, the evidence for NGC 5471 points to a non-uniform distribution of foreground dust, with evidence supporting the possibility of internal reddening in the nuclei.

B.) NGC 4214 #1

In contrast to the case of NGC 5471, the Hα/Hβ map of the largest H II region in NGC 4214 (figure 4.5) shows no distinct features across the areas of highest surface brightness. Here the contour levels have been set at intervals of 10 percent of the normalized ratio. It is notable that most of the region where there is significant signal to produce a ratio map shows relatively little or no reddening. Figure 4.6 shows a slice at constant right ascension taken through nucleus C. This plot was produced in the same way as figure 4.3 for NGC 5471, except that the long dashed line corresponds to the Hα/Hβ ratio for a gas at 10,000 K. Throughout the high signal to noise region, the Hα/Hβ ratio is nearly constant. Figure 4.7 shows a slice at constant declination at the position of nucleus B. There is a strongly reddened region on the western edge of the nebula.

The spectrophotometric determinations of c(Hβ) at positions A, B, and C show excellent agreement between the Mt. Lemmon observations and the KPNO IIDS observations. The Hα/Hβ ratio from the video camera images agree in the sense that the reddening is larger for position B than for positions A and C, but the imaging

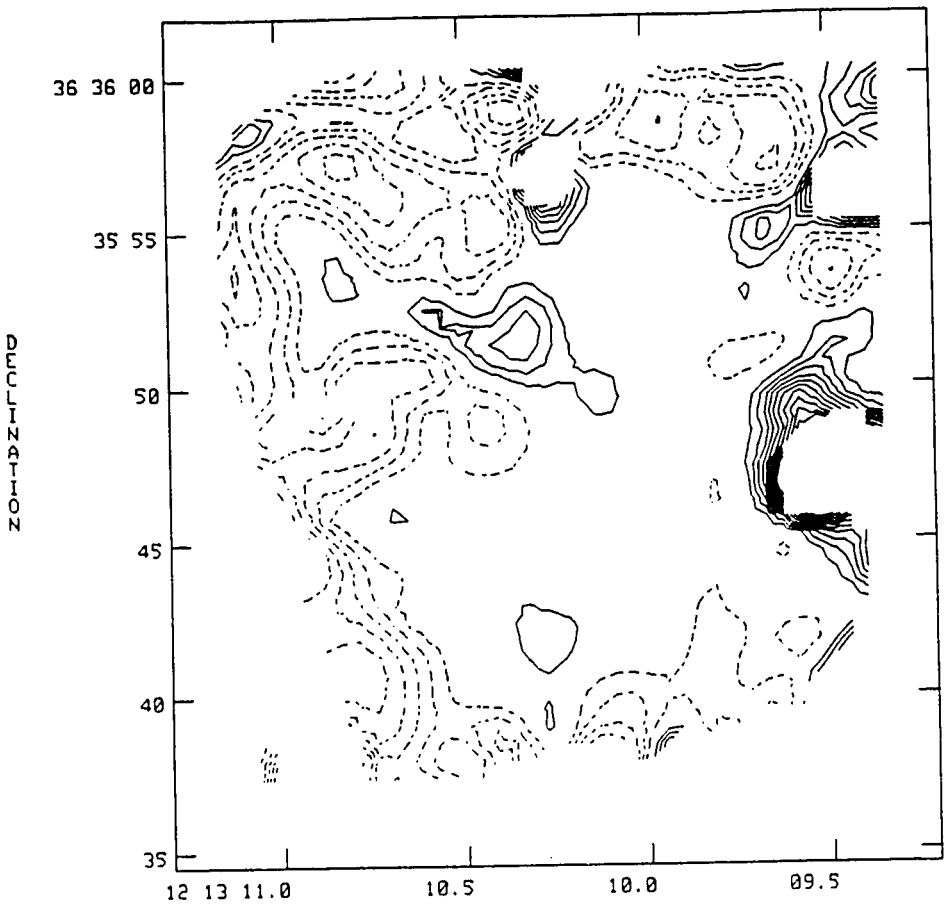

Figure 4.5 Hα/Hβ Ratio Map for NGC 4214

A contour map representation of the Hα/Hβ ratio for NGC 4214. The solid contours are positive and the dashed contours are negative. The image has been offset so that the zero point in the map corresponds to the image mean of 3.2. The contour intervals correspond to intervals of 10% of the image.

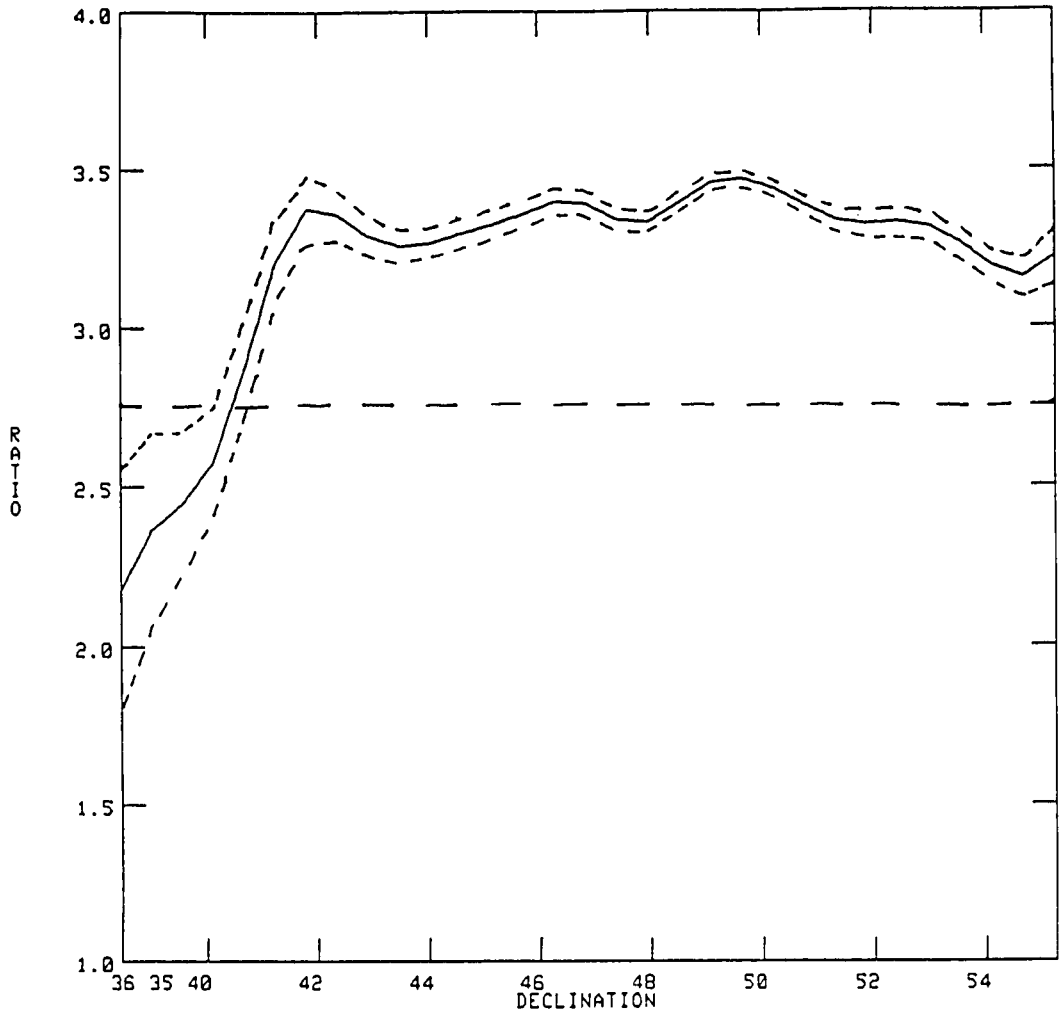

Figure 4.6 Hα/Hβ Slice at Constant R. A. for NGC 4214

A slice in constant Right Ascension of the Hα/Hβ map for NGC 5471. The slice corresponds to the R. A. of nuclei A and C, The solid line shows the actual ratio and the short dashed lines show the one sigma error bars in the ratio. The horizontal dashed lines show the theoretical Hα/Hβ value for a temperature of 10,000 K.

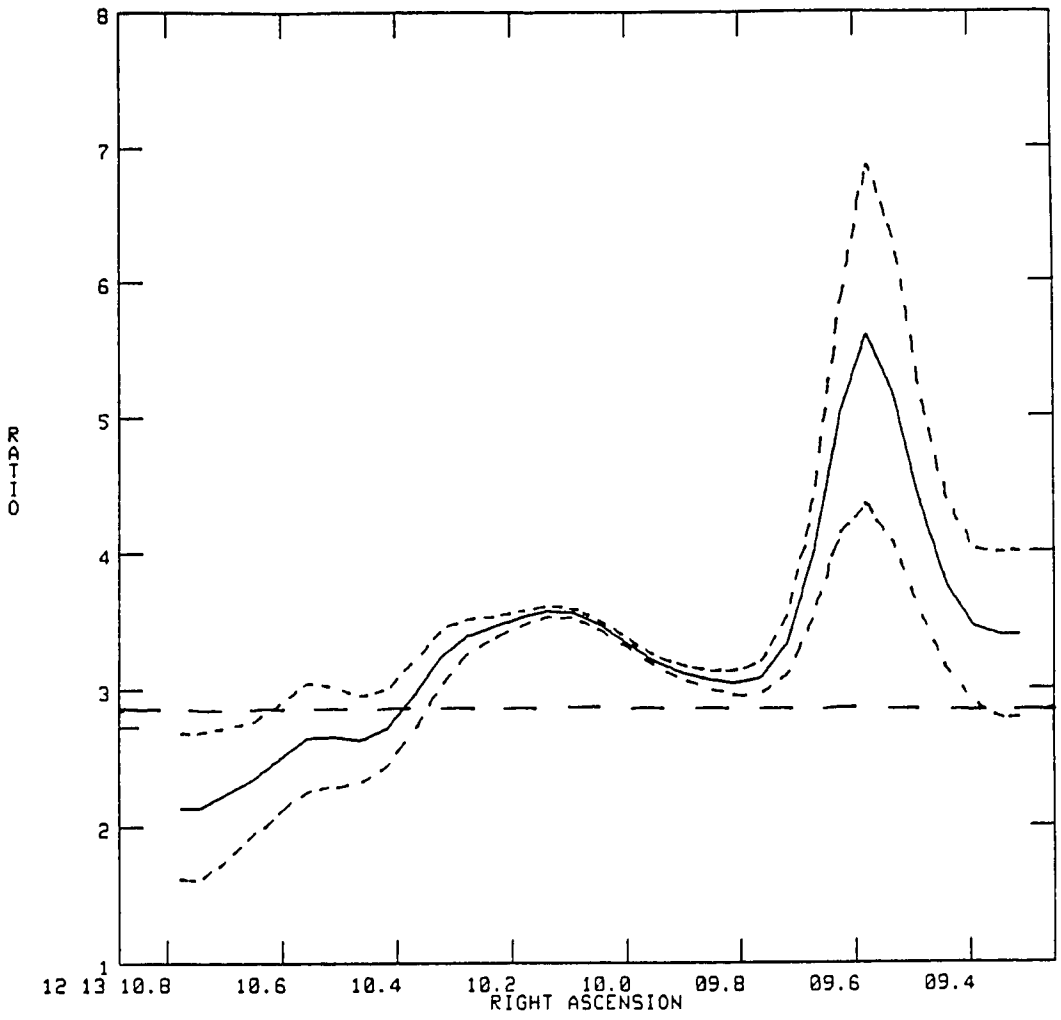

Figure 4.7 Hα/Hβ Slice at Constant Declination for NGC 4214

A slice in constant declination of the Hα/Hβ map for NGC 4214. The slice corresponds to the declination of nucleus B. The solid line shows the actual ratio and the short dashed lines show the one sigma error bars in the ratio. The horizontal dashed lines show the theoretical Hα/Hβ value for a temperature of 10,000 K.

ratios show a smaller amount of reddening at all three positions (.20, .25, and .20 at positions A, B, and C for the video camera images versus .36, .49, and .35 for the IIDS spectrophotometry). Here the agreement between the spectrophotometric measurements and the imaging measurements are much better than for the case of NGC 5471. It would appear most likely that there is a systematic errror in the calibration of the imaging ratio. Fortunately, it is the point to point differences which are most important to this investigation, and these are always consistent within errors.

The signal to noise ratio in the λ6 cm map of NGC 4214 does not warrant producing an Hα/λ6 cm map, but a visual comparison of the Hα (figure 4.8) and λ6 cm (figure 4.9) maps reveals a surprising result. The relative fluxes of nuclei A, B, and C are very different in the two maps. The Hα surface brightnesses of all three nuclei are of comparable strengths, yet, in the radio continuum, B and C are at least 3 times brighter than A. Nuclei A, B, and C all reach above the 60 percent of peak level in the Hα map, whereas nucleus A is only detected at the 20 percent of peak in the λ6 cm map. This indicates a relative overproduction of radio continuum at nuclei B and C, or a relative underproduction of radio continuum at nucleus A. Because the radio spectral index is flat (thermal) for all three positions, it is doubtful that nuclear positions B and C could contain SNRs as in the case of NGC 5471. Since the reddening as measured by the Hα/Hβ ratio map and the optical spectrophotometry is nearly identical

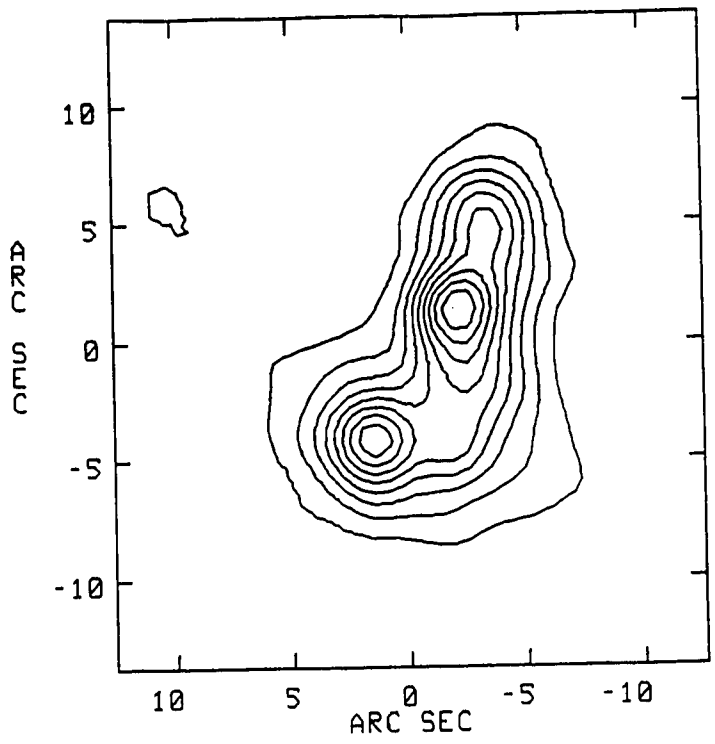

Figure 4.8 Hα Map of NGC 4214

A contour representation map of the Hα image of NGC 4214, for comparison with figure 4.9. The levels are set at intervals of 10% of the image maximum.

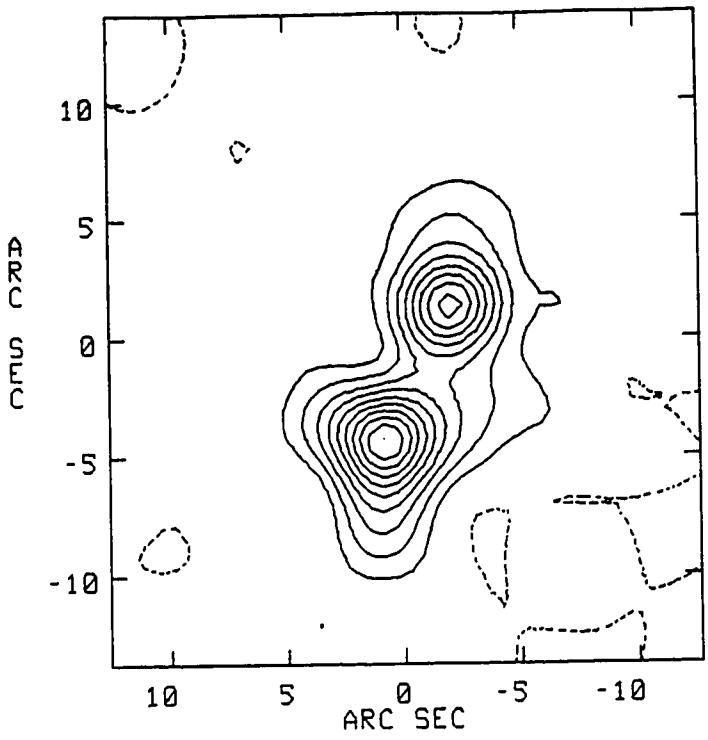

Figure 4.9 λ6 cm Map of NGC 4214

A contour representation map of the λ6 cm image of NGC 4214, for comparison with figure 4.8. The levels are set at intervals of 10% of the image maximum.

at all three positions, it can be concluded that the optical method does not correlate with the radio-optical method for this region. This observation is difficult to understand. Excessive extinction at nuclei B and C seems unlikely because of the close agreement of reddening measures at all three positions. Since any explanation based on extinction would necessarily be ad hoc, and since the presence of SNRs is unlikely, this remains an interesting puzzle.

C.) NGC 2363

The Hα/Hβ ratio map for NGC 2363 is presented in figure 4.10. This ratio map indicates that the reddening is lowest in the central (and brightest) portions of the region. This is only a global trend though as there is no correlation between reddening and brightness when examined on a point by point basis. Figure 4.11 shows a constant declination slice through the nebular ratio map, bisecting nucleus A. The slice shows that the two central regions of lowest reddening are significant and the trend of larger reddening in the outer parts of the region is quite real. The radial gradient in the Hα/Hβ ratio could arise from: a.) a calibration error such as an error in fixing the sky level in one of the two frames; b.) dust in a shell around the H II region; c.) a systematic change in temperature with distance from the center. Since other Hα/Hβ ratio images calibrated in the same way do not show radial gradients, it is less likely that possibily (a) is the explanation. To distinguish between (b) and (c), one would like spectrophotometry of a number of

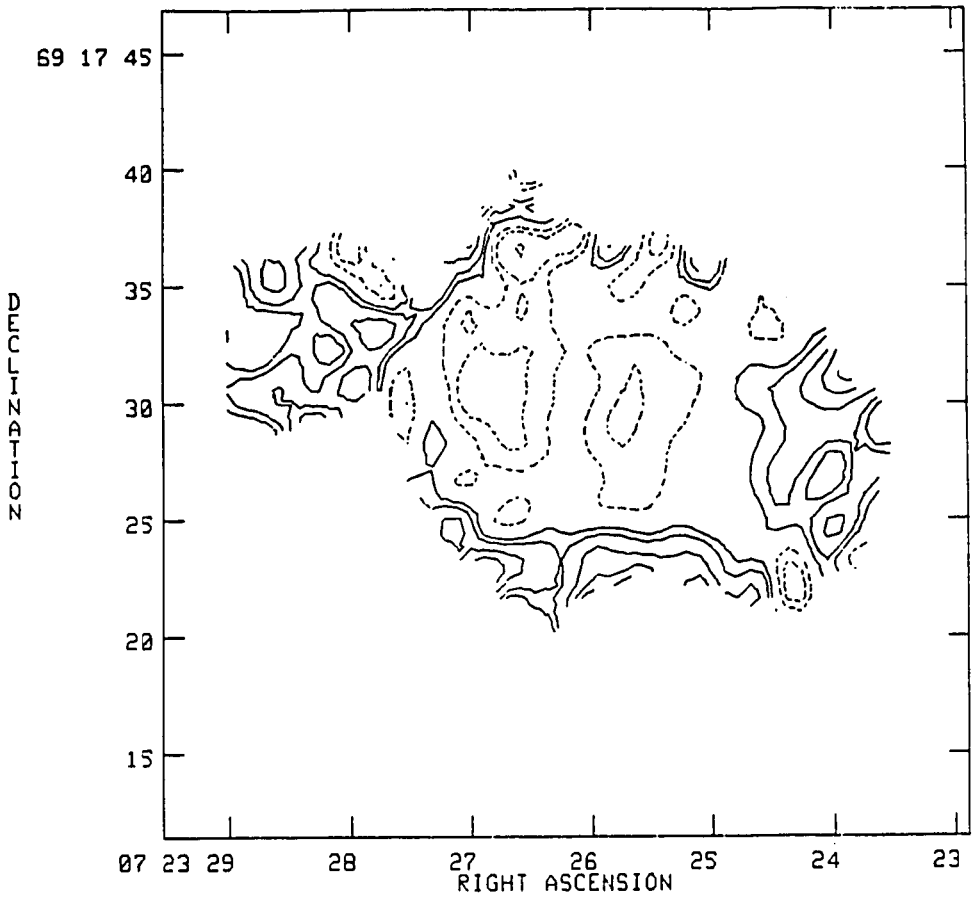

Figure 4.10 Hα/Hβ Ratio Map for NGC 2363

A contour map representation of the Hα/Hβ ratio for NGC 2363. The solid contours are positive and the dashed contours are negative. The image has been offset so that the zero point in the map corresponds to the image mean of 3.4. The contour intervals correspond to intervals of 5, 10, 20, 30, and 40% of the image mean.

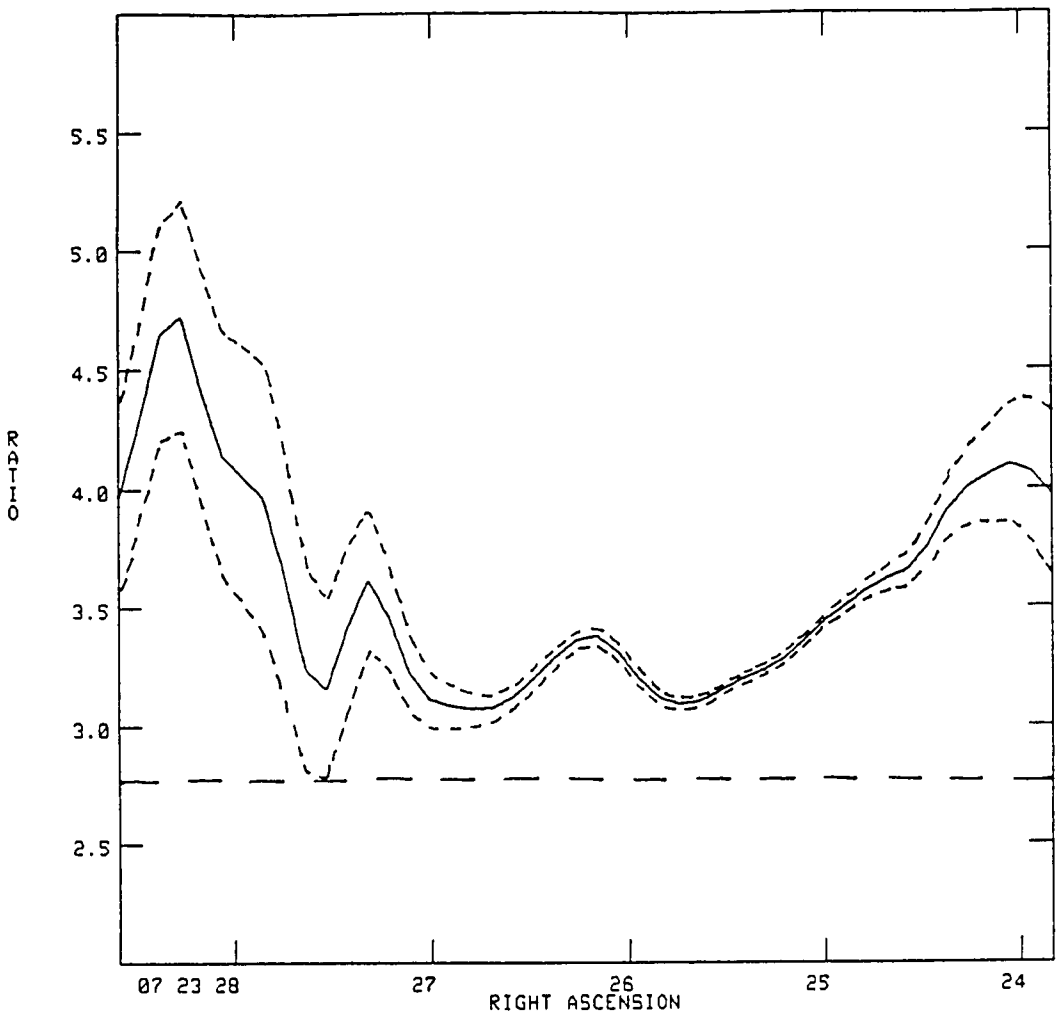

Figure 4.11 Hα/Hβ Slice at Constant Declination for NGC 2363

A slice in constant declination of the Hα/Hβ map for NGC 2363. The slice corresponds to the declination of nuclei A and B. The solid line shows the actual ratio and the short dashed lines show the one sigma error bars in the ratio. The horizontal dashed lines show the theoretical Hα/Hβ value for a temperature of 14,500 K.

positions in the halo, or a series of spectrophotometric measurements with increasing aperture size. Since NGC 2363 is above 60 degrees in declination, it is not observable with the Mt. Lemmon telescope, and, therfore, the IRS measurement is the only measruement reported here in which Hα and Hβ are observed simultaneously. Hence, more observations are necessary to answer this question unambiguously.

Figures 4.12 and 4.13 show the Hα and λ6 cm maps smoothed to resolutions of 4". In both maps, the contours are plotted at 10 percent levels of the peak. A comparison of the two maps shows that the radio emission is more centrally peaked. There is a significant discrepancy in the extent of the lowest contour level. It should be noted that comparing extended emission in optical and radio images can be deceptive. The sensitivity of the VLA to smooth emission of large size scales is determined by the shortest baselines on the array configuration. For this map of NGC 2363, the VLA should be sensitive to all structures up to 30" in size, implying that the difference observed is real and not a product of the observational technique.

The excessive strength of the λ6 cm emission relative to Hα at the position of nucleus A immediately suggests that this might be the position of an SNR as in the case of NGC 5471 B. In fact, the radio spectral index at this position is nonthermal. However, the radio spectral index throughout the entire region is relatively constant. In addition, there is no indication of the presence of an SNR from

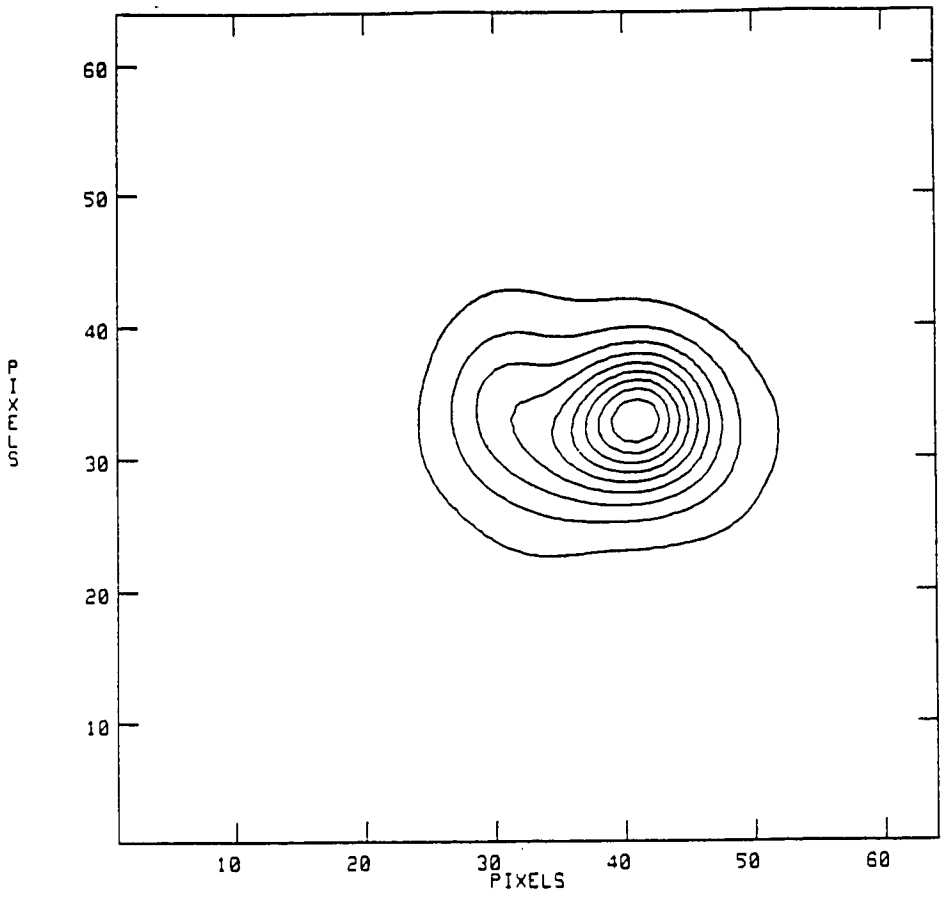

Figure 4.12 Hα Map of NGC 2363

A contour representation map of the Hα image of NGC 2363, for comparison with figure 4.13. The levels are set at intervals of 10% of the image maximum.

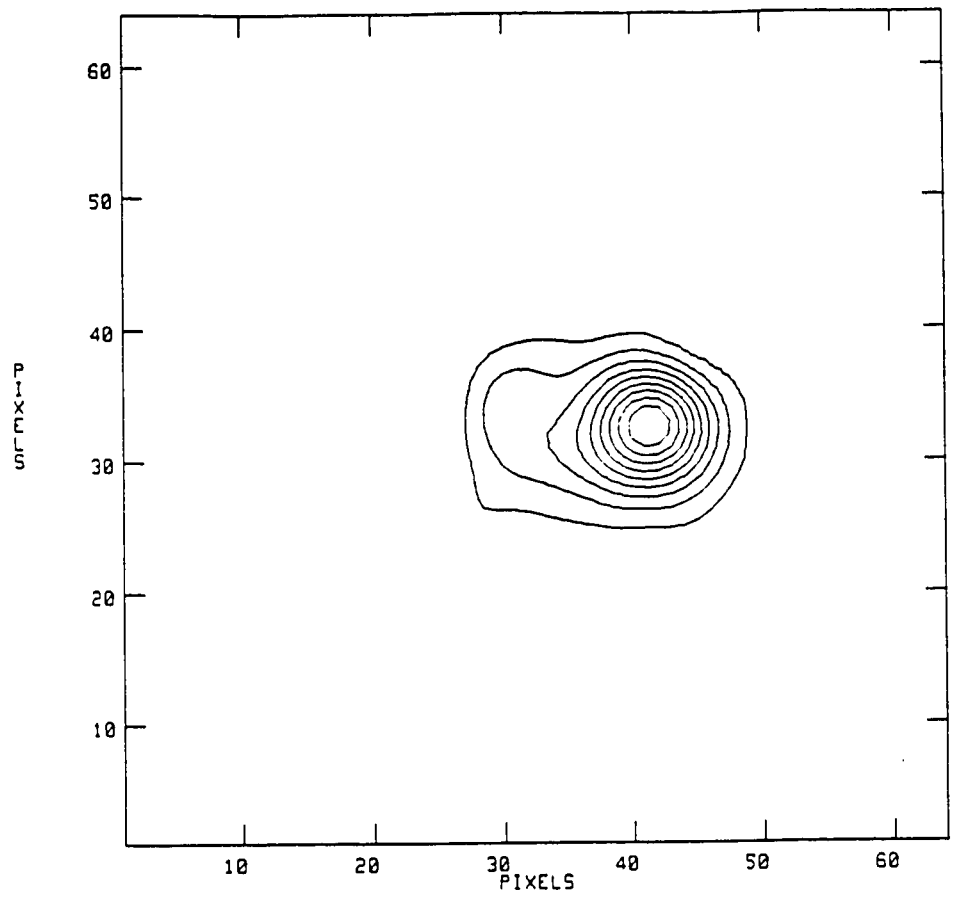

Figure 4.13 λ6 cm Map of NGC 2363

A contour representation map of the λ6 cm image of NGC 2363, for comparison with figure 4.12. The levels are set at intervals of 10% of the image maximum.

the optical spectrophotometry. This will be discussed again in chapter VI.

D.) Hubble V

Hubble V is the most luminous H II region in the local group galaxy NGC 6822. Because of its proximity it affords the best spatial resolution of any of the GEHRs observed in this study. At a distance of 616 kpc (Sandage and Tamann 1974), 1" corresponds to 3 pc. The set of observational data is not complete for Hubble V due to the lack of optical spectrophotometry, but a good set of video camera images and an excellent λ6 cm map have been obtained. Hubble V has been previously observed spectrophotometrically by others with both large and small apertures, and relevant data from these studies are presented in table 4.1.

Figure 4.14 shows the unsmoothed Hα map of Hubble V. A smoothed Hα/Hβ map was constructed and is shown in figure 4.15. Note the large variations in the Hα/Hβ ratio across the face of the nebula. If these variations are all real, it could be that the higher resolution investigation allowed by the proximity of Hubble V is revealing features that are averaged over in the observations of more distant nebulae. The Hα/Hβ ratio is largest in the southeast corner where the Hα emission is strongest. Figure 4.16 shows a diagonal slice through the Hα/Hβ map and demonstrates the range of variations, and the confidence in the ratio. Since Hubble V was not observed

Table 4.1

Optical Spectrophotometry of Hubble V

Authors	aperture size	Log I(Hβ)	c(Hβ)
Melnick (1979)	25"	-12.05	0.21
Lequeux et al. (1979)	3.8 x 12.4"	-12.05	0.8
Pagel et al. (1980)	4"	-12.9	1.05

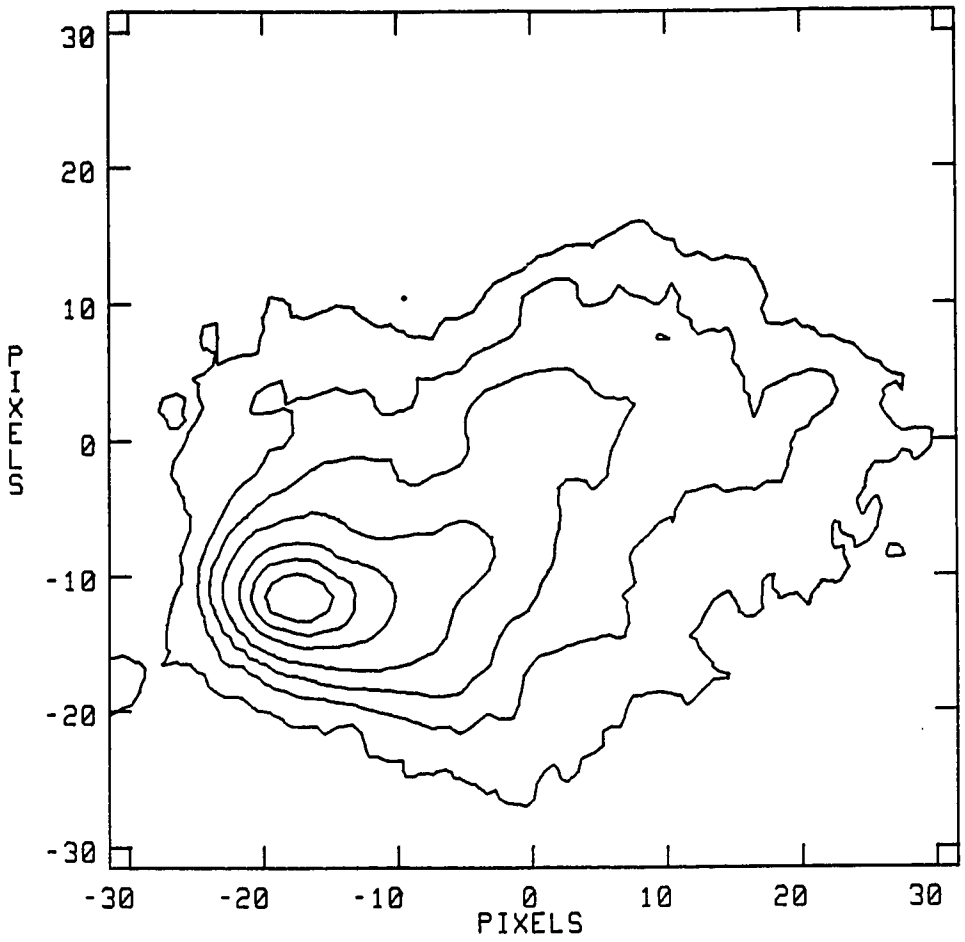

Figure 4.14 Hα Map of Hubble V

A contour map representation of the Hα image of Hubble V in NGC 6822. Contours are set at 2, 5, 10, 20, 40, 60, and 80% of the image maximum.

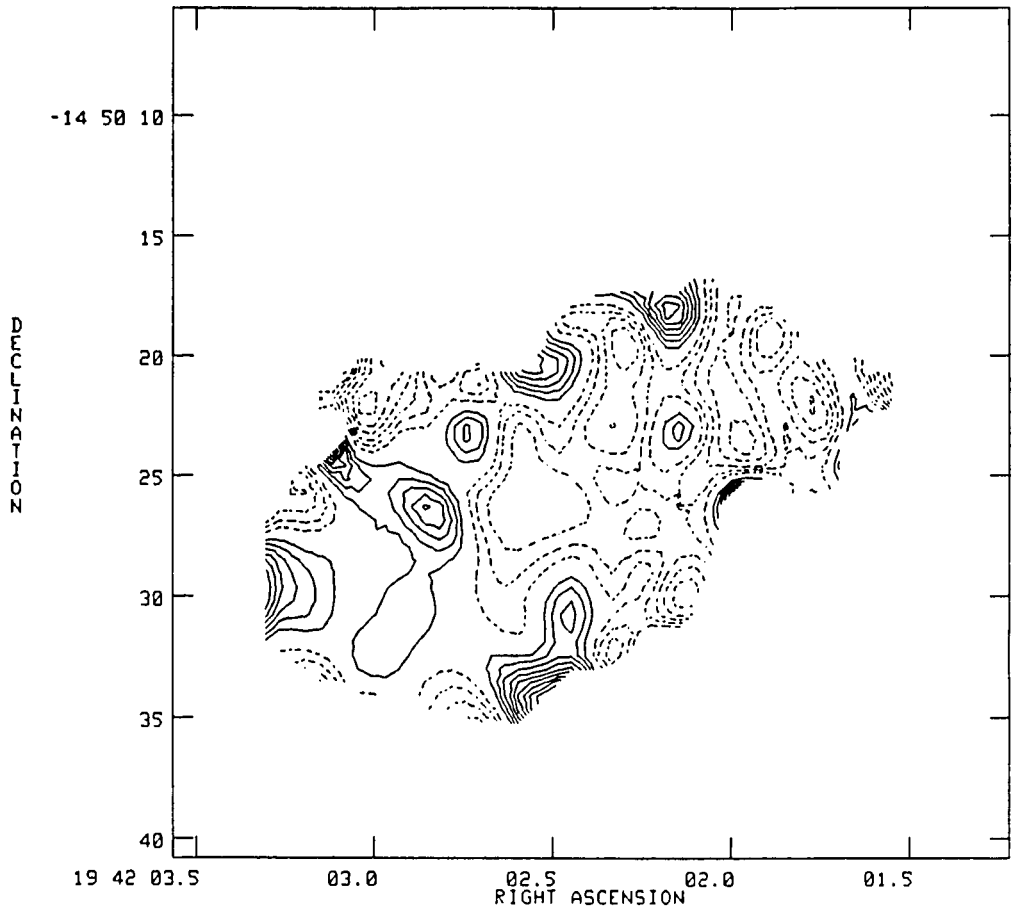

Figure 4.15 Hα/Hβ Ratio Map for Hubble V

A contour map representation of the Hα/Hβ ratio for Hubble V. The solid contours are positive and the dashed contours are negative. The image has been offset so that the zero point in the map corresponds to the image mean. The contour intervals correspond to intervals of 5 percent of the image mean.

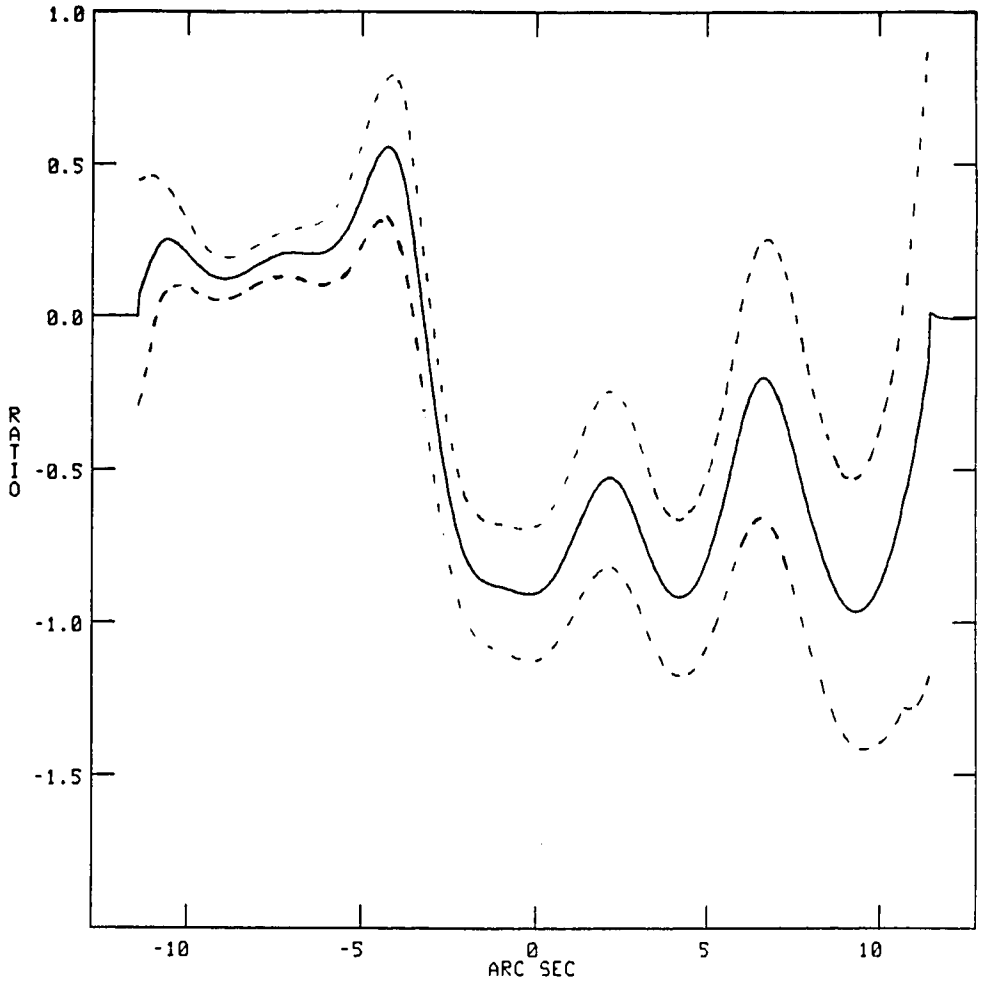

Figure 4.16 Hα/Hβ Slice for Hubble V

A diagonal slice from the southeast to the northwest of Hα/Hβ ratio map of Hubble V. The slice is at a position angle of 57 degrees and passes through the brightest part of the nebula in the southeast. The image has been offset such that the image mean is set to zero and the scale is set relative to the image mean.

with the IRS, the image ratio has been normalized to zero. Melnick (1979) obtained a value of 3.3 for the global Hα/Hβ ratio. Here it can be seen that the Hα/Hβ ratio is significantly stronger in the southeast corner. The variations in the rest of the map are less certain, and are not inconsistent with statistical fluctuations.

The λ6 cm observations were obtained with the VLA in the C configuration, and therefore have a spatial resolution of 5" FWHM. In order to compare the Hα map to the λ6 cm map, the Hα map was smoothed to an identical resolution. A comparison of the two maps (figures 4.17 and 4.18) shows that the radio is more strongly peaked than the Hα in the bright region to the southeast. Because the radio observations were made in the C array, the VLA should be sensitive to structures at least as large as 50", and therefore, the relatively stronger concentration of radio continuum emission in the brightest component is not due to a missing flux problem.

Taking all of the observations together, a very strong case can be made for increased extinction in the brightest part of the nebula. The values of c(Hβ) as measured from optical spectrophotometry increase with decreasing aperture size. Since the small aperture observations can be presumed to be centered on the brightest part of the nebula, this implies that the extinction is greatest at this position. This is confirmed by the Hα/Hβ imaging. The increased λ6 cm/Hα ratio at this position also means that Hubble V represents the first case in which the extinction as measured from the radio-optical

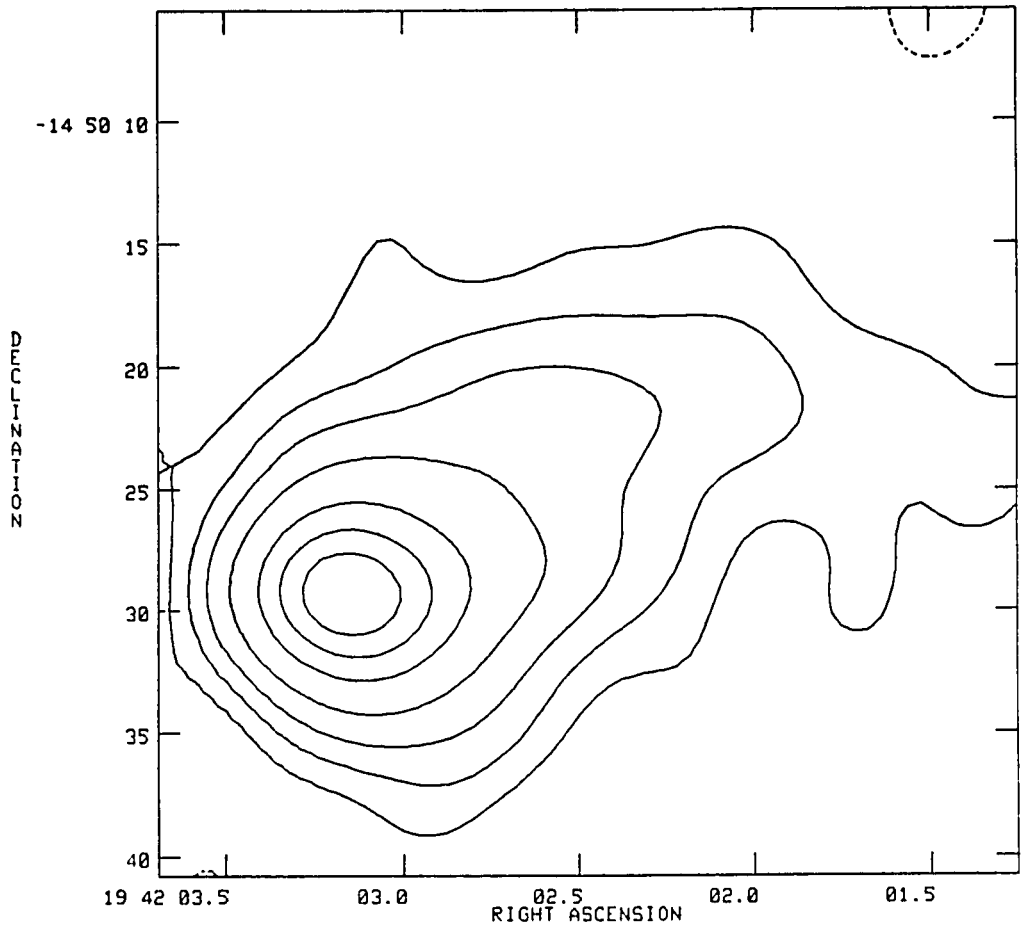

Figure 4.17 λ6 cm Map of Hubble V

A contour representation map of the λ6 cm image of Hubble V, for comparison with figure 4.18. The levels are set at intervals of 2, 5, 10, 20, 40, 60, and 80% of the image maximum.

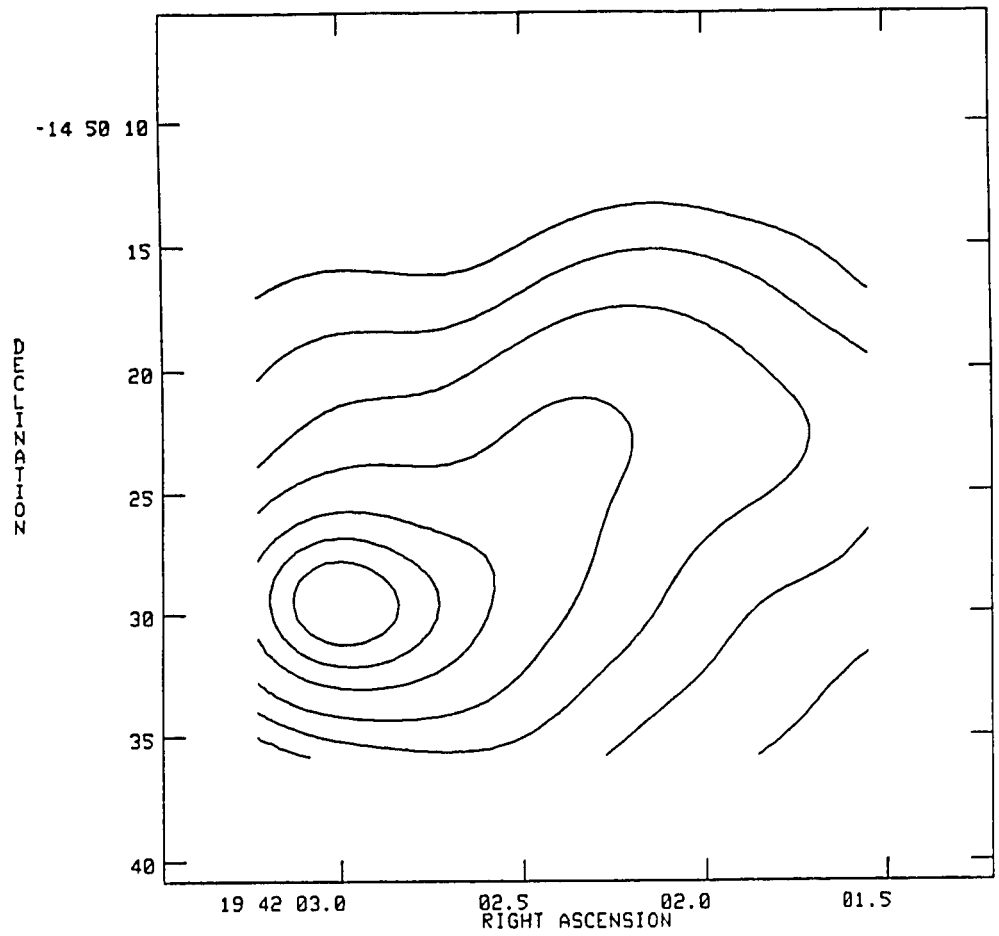

Figure 4.18 Smoothed Hα Map of Hubble V

A contour map representation of the Hα image of Hubble V smoothed to the same spatial resolution as the λ6 cm map in figure 4.17. Contours are set at 2, 5, 10, 20, 40, 60, and 80% of the image maximum.

method correlates with the extinction as measured by the optical method, at least at 5" resolution.

Under the simple model interpretation outlined above, the correlation of strongest extinction with strongest emission might be taken as evidence for internal reddening. However, there is also good evidence that the increased extinction in the southeast of Hubble V may be due to foreground dust. The Ha map shows a very steep gradient to the south and southeast. This could indicate the presence of a large neutral cloud at this position. If there is a large molecular cloud on the southeast border of Hubble V, then the increased extinction in that part of the region could be attributed to foreground dust associated with this cloud. On the other hand, the flux in the radio map also decreases rapidly in the south and southeast. Higher resolution radio observations would be necessary to determine if the gradient in the radio map is as steep as the gradient in the Hα map.

Interpretation

The individual objects described above have provided a large diversity of physical phenomena. There is evidence of reddening by foreground dust, internal reddening, confusion by non-thermal radio emission, and generally a lack of correlation between the extinction determined via the optical method and that determined via the radio-optical method. Perhaps the most striking result is this lack

of correlation between the features in the Hα/Hβ maps and the features in the Hα/λ6 cm maps. In this section this observation will be quantified.

First, it is necessary to put all of the observations on a common ground, in common units. To do this, the formalism of Mathis (1983) is adopted, where extinction is described as an optical depth of dust at Hβ. For the optical method, the measurement of the extinction will be labeled $\tau_{\alpha\beta}$ as derived from the measurements at Hβ and Hα as:

$$\tau_{\alpha\beta} = \frac{A_\beta}{A_\beta - A_\alpha} \ln \frac{F_\alpha j_\beta}{F_\beta j_\alpha}$$

where F_λ are the observed fluxes, j_λ the calculated emissivities, and A_λ the extinction with an assumed wavelength dependence. The conversion from a value of c(Hβ) to $\tau_{\alpha\beta}$ consists of simply multiplying by the natural log of 10.

For the radio optical method, $\tau_{\beta R}$ is defined as:

$$\tau_{\beta R} = \ln \frac{F_\beta j_R}{F_R j_\beta}$$

The adoption of this formalism allows both a direct comparison of the different measures of extinction, and a comparison to the models of extinction by dust in Mathis (1983).

In Table 4.2, the results are listed for three types of calculations of the extinction at Hβ for three GEHRs. The first is a measurement of the ratio of absolute fluxes at λ6 cm and Hβ. The ratio was determined from Hβ and λ6 cm images of equal spatial resolution, by summing over equal areas (5" square apertures). It was found that the ratio at each position was only slightly dependent on the size of the area chosen for the comparison. Factors of two changes in aperture area generally resulted in changes of less than 10 percent in the ratio. The results of these measurements are listed in the first column of table 4.2 and labeled $S_\nu/H\beta_i$. The second set of data consists of measurements of the Hα/Hβ ratio in the same areas. Since these values are based on the ratio determined from the IRS measurements, the value for the total core of the nebula is placed in parentheses. These values were found to be even less sensitive to aperture size. These ratios are listed in the second column of table 4.2 and labeled $H\alpha_i/H\beta_i$. The third list of data is simply the values of c(Hβ) determined from the small aperture spectroscopy. It is important to remember that the IIDS values are determined from observations limited to the blue part of the spectrum and therefore do not include a measurement of the Hα/Hβ ratio. The IIDS measurements are listed in column 3 and the IRS and Mt. Lemmon measurements in column 4.

Table 4.2

Comparison of Extinction Measures

position	$S_\nu/H\beta i$ ($\times 10^{-9}$)	$H\alpha i/H\beta i$	$c(H\beta)$ IIDS	$c(H\beta)$ IRS/IDS	$\tau_{\beta Ri}$	$\tau_{\alpha\beta i}$	$\tau_{\beta s}$	$\tau_{\alpha\beta s}$	$\tau_{\beta Ri}-\tau_{\beta s}$	$\tau_{\beta Ri}-\tau_{\alpha\beta s}$
N5471 IRS	12.0	(2.88)	...	.07	1.37	(.08)	...	.16	...	1.21
A	10.0	2.82	.54	.18	1.19	.02	1.24	.41	-.05	.78
B	16.1	2.77	.51	.18	1.66	-.03	1.17	.41	.49	1.25
C	10.3	2.84	.33	.25	1.22	.04	.76	.58	.46	.64
D	9.4	2.88	.21	.00	1.12	.08	.48	.00	.64	1.12
E	7.7	2.96	...	...	.93	.17	...	...	...	...
(no dust)	3.1	2.80								
N4214 IRS	6.6	(3.22)	...	.13	.85	(.45)	...	.30	...	.55
A	5.7	3.08	.36	.31	.71	.32	.83	.71	-.08	.00
B	14.6	3.16	.49	.51	1.65	.39	1.13	1.17	.52	.48
C	10.1	3.13	.35	.38	1.28	.37	.81	.87	.47	.41
(no dust)	2.8	2.85								
N2363 IRS	8.0	(3.38)	...	.27	.92	(.51)	...	.62	...	.30
A	15.2	3.22	.39	...	1.56	.36	.90	...	.66	...
B	10.3	3.25	.56	...	1.17	.39	1.29	...	-.12	...
C	11.2	3.32	.00	...	1.26	.46	.00	...	1.26	...
(no dust)	3.2	2.77								

The next four columns show all of the data from the first four columns converted to extinctions at Hβ and represented as optical depths of dust. The values derived from imaging measurements are noted with a 'i' subscript, and the values from the spectrophotometry are noted with an 's' subscript. The errors for all values of τ listed in columns 5 - 8 should be less than 0.3. The last two columns show the difference between the values of optical depth between the radio-optical method and the optical method from the small aperture spectroscopy.

The first detail to check is the agreement between the values of $\tau_{\alpha\beta}$ derived from the imaging ratios and the Mt. Lemmon spectrophotometry. Since the Mt. Lemmon values are based primarily on the Hα/Hβ ratio, one should expect close agreement. This is not the case for either NGC 5471 or NGC 4214. In both cases, the extinction measured from the image ratios (as based on the calibration for the large aperture spectrophotometry) is much less than the extinction as measured by the small aperture spectrophotometry. Since the difference is systematic, it might be a result of the calibration. The discrepancy translates to a relative deficiency in the IRS line strength measurements of Hα of 15 percent for NGC 5471 and 20 percent for NGC 4214. These values seem too large for calibration errors to be the sole source of the discrepancy.

With this in mind, further inspection reveals that, in many cases, the extinction as measured by the radio-optical method is comparable to the extinction as measured from the IIDS spectra. Except for a few positions, the difference is much less than the typical difference in A_V noted by Isreal and Kennicutt (1980). They found that the excess extinction for GEHRs ranged from factors of 1.5 to 6. This would translate to an addition of .5 to 2.2 in the optical depth of dust at Hβ. For NGC 5471 specifically, they derived a value of A_V of 1.6 which translates to a value of $\tau_{\alpha\beta} = 1.8$. This is larger than the value of $\tau_{\beta R}$ derived here for all of the positions in NGC 5471.

Figure 4.19 shows a graph of $\tau_{\alpha\beta}$ as measured with the three different spectrophotometers plotted versus $\tau_{\beta R}$. The long dashed line indicates where the points would lie for a one-to-one correlation. The upper solid line shows the average displacement corresponding to an excess extinction of 1.2 magnitudes in A_V found by Isreal and Kennicutt. The middle diagonal line shows the theoretical relationship between $\tau_{\beta R}$ and $\tau_{\alpha\beta}$ if the difference of dust albedo at λ6563 and λ4861 is taken into account (Mathis 1983). The theoretical line represents the lower limit one obtains from a homogeneous screen of foreground dust. If there are inhomogeneities in the foreground dust, or, if there is internal dust, it is possible to have values at any position above the line.

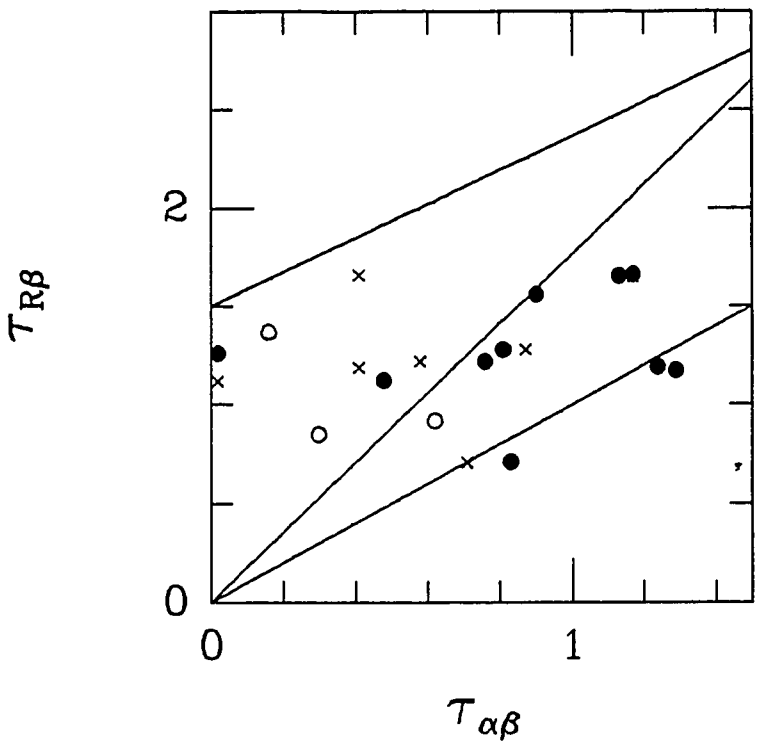

Figure 4.19 Plot of $\tau_{R\beta}$ Versus $\tau_{\alpha\beta}$

A plot of $\tau_{R\beta}$ versus $\tau_{\alpha\beta}$ as defined by Mathis (1983). Points with $\tau_{\alpha\beta}$ values from IIDS measurements are marked with a (.), points with $\tau_{\alpha\beta}$ values from the Mt. Lemmon IDS are marked with a (x), and points with $\tau_{\alpha\beta}$ values from the IRS measurements are marked with a (o). The uppersolid line corresponds to an average excess extinction of 1.3 as found by Israel and Kennicutt (1980). The dashed line corresponds to no excess extinction. The lower solid line corresponds to the lower limit of excess extinction predicted by the model of Mathis (1983).

One notes immediately that all of the observational points show less of a discrepancy than the average for the Isreal and Kennicutt sample. In fact, some points show no discrepancy at all. Note also that more than half of the points lie below the theoretical limit derived by Mathis. A simple interpretation suggested by this data is that as one observes GEHRs at comparable resolutions in the optical and the radio, the discrepancy is significantly decreased.

Despite the fact that the discrepancies between $\tau_{\beta R}$ and $\tau_{\alpha\beta}$ shown in figure 4.19 are smaller than the average discrepancy found by Isreal and Kennicutt, there is still a marked discrepancy. Most of the points are above the dashed line which indicates a one-to-one correspondence between the two methods of measurement. Mathis (1983) has shown that this may be a result of ignoring the wavelength dependence of the dust responsible for the extinction. If the albedo of the dust at λ6563 is less than the albedo of the dust at λ4861, then the Hα is absorbed more per optical depth of extinction than the Hβ. In this case, the extinction estimated from the Hα/Hβ ratio will be an underestimate of the true extinction. In the case of a homogeneous screen of foreground dust, the difference in albedo produces a linear relationship between $\tau_{\alpha\beta}$ and $\tau_{\beta R}$ as shown in figure 4.19. The slope of the line is greater than 1.0, and is fixed by the difference in albedo. The line shown in figure 4.19 uses albedo values from a theoretical model of Mathis, Rumpl, and Nordsieck (1975). In theory, if the model correctly matched the properties of

the dust, all of the points would lie on or above the line. (Clumpiness in foreground dust or internal dust would increase the $\tau_{\beta R}/\tau_{\alpha\beta}$ ratio as noted before.) Therefore, figure 4.19 suggests that the dust causing the extinction in these GEHRs does not have as great a wavelength dependence of albedo as the dust in the model of Mathis, Rumpl, and Nordsieck. The large uncertainties associated with the data points (both statistical and systematic) do not allow any further statements about the adequacy of the dust model.

Conclusions

Images in the light of Hα, Hβ, and λ6 cm have been combined with optical spectrophotometry to investigate the reddening and extinction in GEHRs. The motivation has been to search for the source of the anomalous extinction detected when comparing radio-optical extinction values with optical extinction values. The images were used to map the distribution of the extinction. In some cases there is good evidence of foreground clouds from the Hα/Hβ ratio maps. Because they cover only a small fraction of the nebular surface, the foreground clouds detected cannot account for the discrepancy between the radio-optical method and the optical methods of determining extinction. The limited resolution of the optical images cannot rule out a homogeneous distribution of small (less tha 100 pc) clouds.

There is some evidence of increased extinction at the positions of the intensity maxima. Using an admittedly simplistic model, this could be interpreted as evidence of extinction due to internal dust. It should be noted that anomalous extinction is a property of all GEHRs, and the coincidence of increased extinction and nebular emission is noted in only certain observations. Given the fact that the interpretation is model dependent, extinction by internal dust remains difficult to detect or dismiss.

There is almost no correlation among the point to point differences in the two extinction measures. The Hα/Hβ maps often show no resemblance to the Hα/λ6 cm maps. Any explanations of the anomalous extinction based on systematic trends can be held in doubt.

In one case (NGC 5471) there is clear evidence of nonthermal radio emission produced by an SNR. This leads to an overestimate of the extinction using the radio-optical method. The position of the SNR represents the highest value of anomalous extinction. In a second GEHR (NGC 2363) the radio continuum is non-thermal, but there is no single isolated nonthermal source to attribute this emission to (see chapter VI). From this it can be concluded that unrecognized non-thermal emission may lead to false measurements of extinction in several GEHRs, but it cannot be the universal explanation.

Comparing the results of this study with the work of Israel and Kennicutt yields evidence that a significant fraction of the anomalous extinction may be due to resolution effects, and that even better spatial resolution than 1 - 3" would be useful in order to understand the distribution of dust across the face of the nebula and along any line of sight. At some of the positions, the results of the optical and radio-optical methods actually agree quite well. The fact that the anomalous extinction did not disappear altogether may be due to the limited resolution of these observations.

Finally, it is noted that the basic method of interpretation may be at fault. Throughout the discussion the standard reddening law as derived from galactic sources has been assumed. This could prove to be an erroneous assumption, especially considering the fact that GEHRs are always found in regions of relatively low heavy element abundances. The theoretical work of Mathis has shown that the wavelength dependence of the dust grain albedo can have a significant effect on the optical method of determining extinction. It is not possible to use the observations of this study to put significant constraints on the properties of the dust as modeled by Mathis, but future observations may show that this effect is indeed important.

Chapter V Abundance Measurements in GEHRs

The emission line spectrum of an ionized gas can be used to analyze the chemical composition of that gas. Astronomers have made use of this fact to determine the chemical abundances in H II regions. This chapter will begin with a brief overview of the methods for calculating abundances with emphasis on the problems associated with GEHRs. Next, the choice of methods used in this study will be described and justified. Following this, the results of the abundance calculations will be reported with a comparison to the other results in the literature. The relative importance of the different sources of error will be discussed. Finally, the relevance of these results to other research will be explored.

Historical Background of H II Region Abundance Calculations

In the last few decades, there has been considerable progress in both the observational and theoretical aspects of chemical abundance determination from H II region spectra. Numerous review articles exist (e.g. Osterbrock, 1970; Peimbert, 1975; Pagel and Edmunds, 1981). The underlying assumption of chemical abundance analysis requires that the sole source of energy input is photo-ionization. Given this assumption, the basic method consists of a three part approach:

1.) Determine the physical conditions in the gas (i.e. electron temperature and electron density).

2.) Calculate the relevant physical parameters governing the emission process (e.g. photoionization cross-sections, recombination coefficients, transition probabilities, and collision strengths).

3.) From the emission line strength ratios calculate the abundances of the different ionic species relative to hydrogen.

If one has the abundances of all of the stages of ionization for a particular element, then a simple sum results in the relative elemental abundance.

There are several complications to this process, even ignoring all of the complications of getting accurate relative line strength ratios. Starting with the first step, variations in temperature along the line of sight are impossible to detect and difficult to estimate for purposes of error analysis. (At the densities normal for H II regions, the physical parameters are nearly insensitive to differences in density and therefore density variations are not thought to be a problem.) Because temperatures are derived from forbidden line ratios (such as R[O III] = (λ5007 + λ4959)/λ4363) which are exponentially sensitive to temperature (R[O III] $\propto$ $\exp(3.29\times10^4/T)$), the derived temperatures will actually be larger than the average temperature along the line of sight if variations in the electron temperature are present. Peimbert and Costero (1970) developed a method of calculating abundances assuming a mean temperature fluctuation along the line of sight. It is generally assumed that the temperature fluctuations in a GEHR are very small

(t^2 = .01; Rayo, Peimbert, and Torres-Peimbert 1982). If this is true, then the effects of temperature fluctuations on the abundance determinations are generally smaller than the effects of observational errors.

Insufficient information about certain ionic states is also a problem. If a study is limited to optical wavelengths, then there is no information for the ionic species that do not produce strong emission lines in the optical spectrum. Recent ultra-violet spectroscopy, most notably the work done with the International Ultraviolet Explorer satellite, has produced measurements of several ionic species unobtainable in the visible. The most important of these additions are the ionized states of carbon. Still, there are important ionic species which lack measurements.

The accepted solution to this incompleteness problem is to rely on the near-coincidence of ionization potentials. For example, since the ionization potentials of O^{++} and He^{+} are similar, when the λ4686 line of He^{++} is weak or absent in an H II region spectrum, it can be safely assumed that there is an insignificant fraction of oxygen in the O^{+++} stage. The oxygen abundances can then be calculated from the sum of the O^{++}, O^{+}, and O^{o} ionic stages. This type of assumption is involved in a more treacherous way when measuring the nitrogen abundance. Since the ionization potentials of O^{+} and N^{+} are similar, the nitrogen abundance is usually calculated from the product of the N^{+}/O^{+} ionic abundance ratio and the total oxygen abundance. In this

type of calculation, the ratio of the O^+ abundance to the total oxygen abundance is referred to as the 'ionization correction factor'. This procedure can be especially dangerous because in many cases the majority of the nitrogen is ionized to the N^{++} stage. Thus the total abundance measurement is based on the measurement of a small fraction of the total species. Additional uncertainty has been cast on this method by Rubin (1983) in which it has been pointed out that the opacity effects of elements heavier than helium can significantly alter the ionization structure of an H II region.

The spectral dependence of the ionizing radiation (the distribution of stellar flux shortward of $\lambda 912$) is yet another important factor that can be difficult to measure, yet can potentially affect the emitted spectrum of the H II region. Internal dust will 'soften' the radiation field, resulting in nebula of lower excitation. Balick and Sneden (1976) showed that the metal abundances of the exciting stars can alter the nebular spectrum such that abundance determinations could differ by factors of two to three.

The best way to take these many uncertainties into account when interpreting H II region spectra is to develop a detailed model of the region producing the spectrum. In this way, the effective temperature of the exciting stars can be considered, and realistic estimates of the fractional volume of the different ionization zones can be calculated. Such models usually divide the nebula into high

and low ionization zones. The high ionization zone is the volume in which oxygen exists primarily in the O^{++} state. In the low ionization zone, oxygen is in the O^{+} state. Shields and Searle (1978) have applied this method to three H II regions in M 101. In general, the agreement between the observed and model spectra adequately constrained the abundance calculations. Dufour, Talbot, Jensen, and Shields (1980) developed a differential modeling technique based on the adoption of a single model as a reference model. A grid of models is run wherein only one parameter is changed, and thus the dependence of the output on each input parameter is measured. Using this method, individual models do not need to be calculated for each H II region. Instead, measurements of the differences between the calculated reference model spectrum and the observed H II region spectrum will suffice for abundance determination. Of course, large differences between the reference model and the observed H II region will add uncertainty to the results of this method.

Given all of the uncertainties described above, one's first impression might be that the results of chemical abundance analyses of H II regions, especially large H II regions in other galaxies, would carry with them large uncertainties. In fact, this is not the case. The large body of theoretical and observational work has bolstered the confidence of researchers in this field such that the quoted errors in the helium abundance are typically of the order of 3

percent or less, and oxygen, neon, and nitrogen abundances are typically reported with 10 percent uncertainties. Recent theoretical work has concentrated on measuring the effects that variations in physical conditions will have on the emission spectra of H II regions. Both Stasinska (1980) and French and Grandi (1981) have produced extensive grids of model H II regions. These studies concluded that the abundance determinations were insensitive to density fluctuations and the variations introduced when an H II region is excited by a number of stars covering a range of stellar effective temperatures.

On the observational side, the exhaustive study of McCall (1982) resulted in the conclusion that H II region spectra make up a one parameter family. From a study of 99 H II regions in 20 galaxies, he concludes that the total oxygen abundance is the primary determinant of the emission line spectra of an H II region. Strong correlations with the lines of [N II] and [S II], and the equivalent width of Hβ are reported. Following the premise that H II region spectra comprise a single parameter family, it is then possible to determine the elemental abundances in H II regions by measuring only λ3727, λ5007, and λ4861.

Method for this Study

Given the prevailing view of extragalactic H II regions, one would expect the emission line spectra observed at different places within a single nebula to be identical. If there are significant departures from the mean spectrum within a single H II region, then one of the assumptions has broken down. These assumptions are: a.) that the sole energy input is photoionization, b.) that the chemical abundance is uniform throughout the region, c.) that geometrical effects are unimportant, and d.) that the distribution of types of exciting stars is constant throughout the nebula, or that differences are not important. Since this study constitutes a search for significant departures, what is of interest are variations in the emitted spectra. In fact, converting these spectra into estimates of chemical abundances will only translate the differences into more meaningful units. For this purpose, the simplest interpretive scheme will suffice.

For this reason, a one-zone model will be used. The model calculations will use the temperature derived from the [O III] lines and an electron density of 100 cm^{-3}. In order to confidently calculate abundances based on a two zone model, one must be able to calculate the conditions in both zones. Typically, temperatures for the lower ionization zone come from the [N II] λ6548 + λ6584/λ5755 ratio. In most GEHRs, the λ5755 line strength is approximately a thousand times weaker than that of Hα, and as such, is not detected in most of the spectra in this study. This is the case for most

observations of GEHRs. However, it is common in such studies to adopt a temperature for the lower ionization zone based on model calculations. Since this is a search for variations in GEHRs, there is no need to use such an assumption. By assuming a single temperature for both the O^{++} and O^{+} zones, it is most likely that the temperature in the O^{+} zone is being overestimated. This leads to an underestimate of the O^{+} abundance. However, the interest here is in differences within a single GEHR. Certainly a one zone model will suffice.

Obviously the strength of the result depends on the error analysis. The data input will be line strengths, relative to Hβ, with associated uncertainties derived from the statistical uncertainties of the line strength measurements and the uncertainty of the reddening correction. The uncertainties in the relative ionic abundances will be a result of the line strength uncertainties and the uncertainty in the temperature estimate. It is necessary to assume that the physical parameters (emission coefficients) for a given temperature are correct. By carrying out the calculations at three different values of the electron temperature (the [O III] temperature and + and - 1σ) and accounting for the propagation of the line strength errors, the relative importance of both can be assessed. The calculations were limited to ionic species for which strong lines could be measured and good ionization correction factors exist. Five ionic species meet these criteria (He^{+}, λ5876, λ4471,

λ6678; O^{+}, λ3727; O^{++}, λ5007, λ4959; N^{+}, λ6584; Ne^{++}, λ3869). The helium lines are listed in order of decreasing strength.

The emission coefficients for hydrogen and helium came from the studies of Brocklehurst (1971,1972). The emission coefficients for the heavier elements were calculated using a five level atom program originally developed by Brugel (1980) and later modified by A. Raga at the University of Washington.

The Abundance Calculations

The relative line strengths in tables 3.1, 3.2, and 3.3 show that, in general, the differences between the regions are larger than the point to point differences within a single nebula. However, there are noticeable exceptions to this trend. For example, note the differences in the λ5007 strength in NGC 5471. Figures 5.1, 5.2, and 5.3 show maps of the λ5007/λ6563 ratio for NGC 5471, NGC 4214, and NGC 2363. In all three regions there are significant differences from point to point and a noticeable radial gradient in the sense that the [O III] emission is strongest in the central cores of the regions observed. Remembering that the Hα/Hβ ratio maps, in general, showed very small variations, one can conclude that the observed differences are produced by real differences in the emitted spectra, and not differences caused by reddening effects.

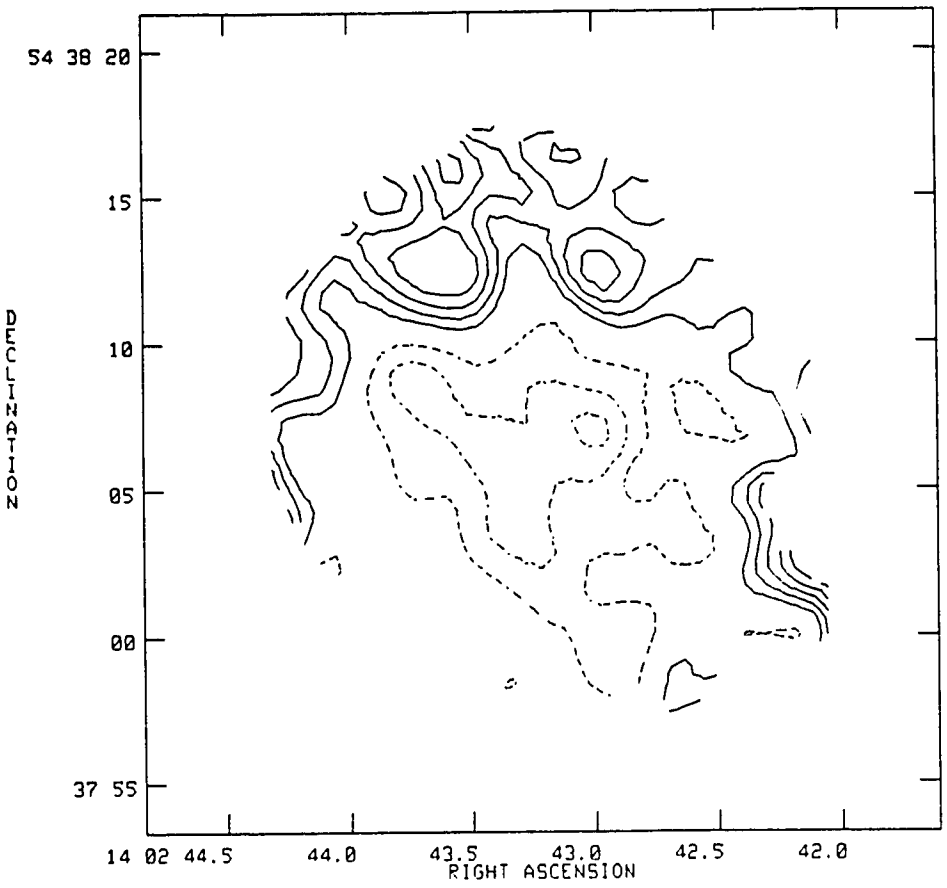

Figure 5.1 Hα/λ5007 Ratio Map for NGC 5471

A contour map representation of the Hα/λ5007 ratio for NGC 5471. The solid contours are positive and the dashed contours are negative. The image has been offset so that the zero point in the map corresponds to the image mean. The contour intervals correspond to intervals of 10 percent of the image mean.

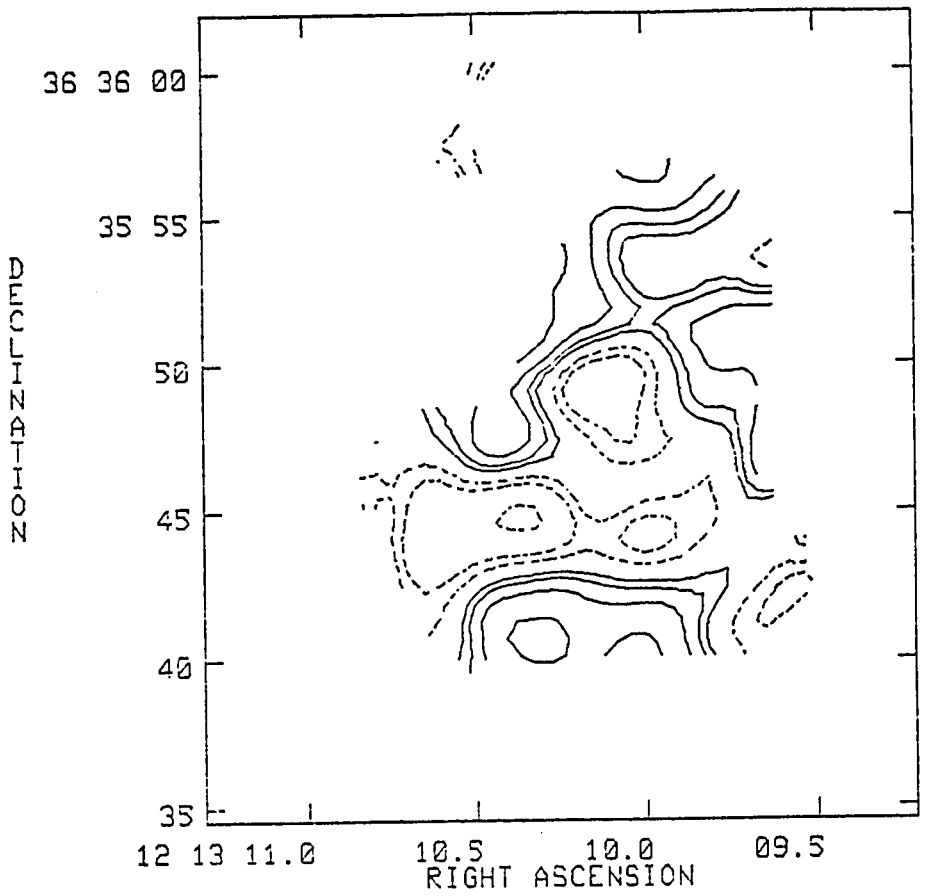

Figure 5.2 Hα/λ5007 Ratio Map for NGC 4214

A contour map representation of the Hα/λ5007 ratio for NGC 4214. The solid contours are positive and the dashed contours are negative. The image has been offset so that the zero point in the map corresponds to the image mean. The contour intervals correspond to intervals of 10 percent of the image mean.

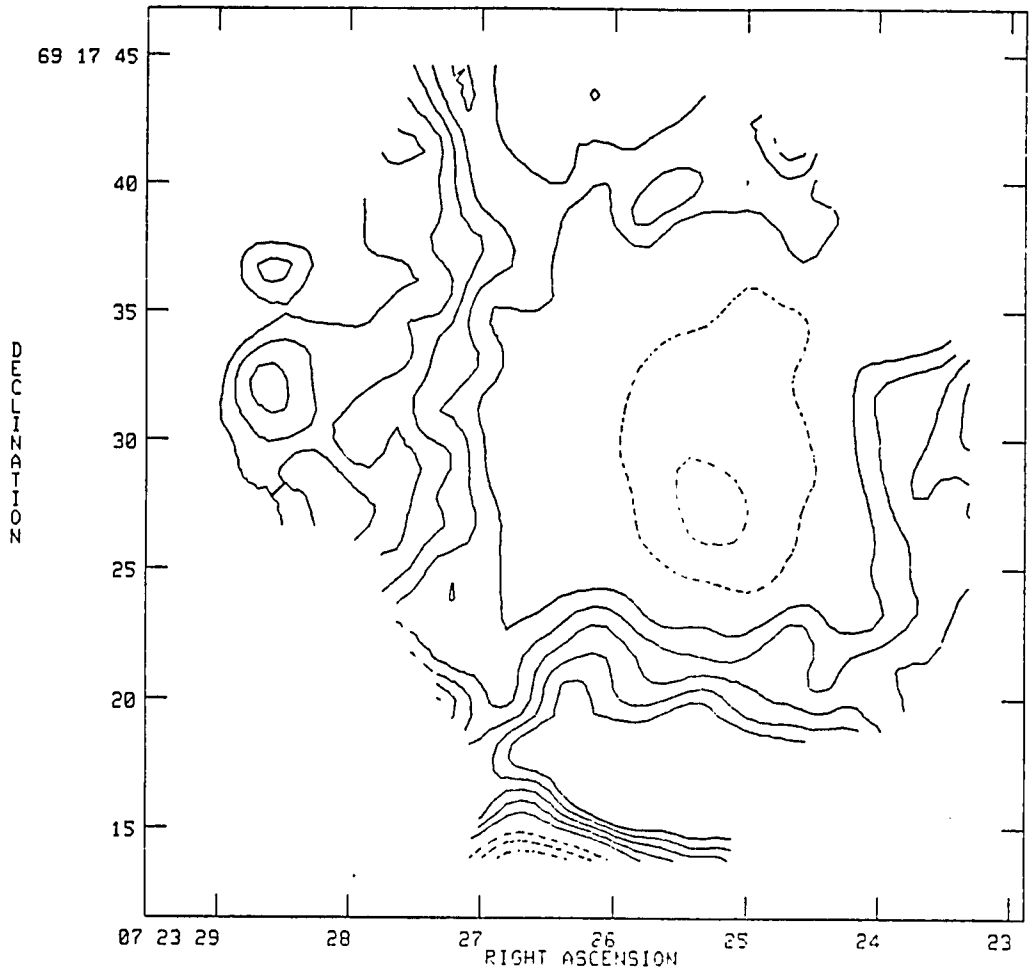

Figure 5.3 Hα/λ5007 Ratio Map for NGC 2363

A contour map representation of the Hα/λ5007 ratio for NGC 2363. The solid contours are positive and the dashed contours are negative. The image has been offset so that the zero point in the map corresponds to the image mean. The contour intervals correspond to intervals of 10 percent of the image mean.

Table 5.1 shows other line ratios of interest for these GEHRs. The λ5007+λ4959/λ4861 ratio is used to determine the O^{++} ionic abundance, and is almost independent of reddening effects. Note the good agreement between the KPNO IIDS values and the Mt. Lemmon IDS values. Note also the large range of values in the λ5007+λ4959/λ4861 ratio for an individual region. The λ3727/λ5007 and the λ6300/λ5007 ratios are indicative of the relative populations of the different ionic species of oxygen. These ratios are insensitive to elemental abundance, and therefore differences in these ratios should point to differences in physical conditions. There is a large range in these values also. The λ6584/λ3727 and λ6717+λ6731/λ3727 ratios show the relative strengths of emission from low ionization species and the λ3869/λ5007 ratio shows the relative strengths of two lines from high ionization species. Because these ratios compare lines from the same ionization zones, these ratios should be less sensitive to variations in physical conditions than comparisons of lines from different zones. Therefore significant differences in these line strength ratios would point to differences in elemental abundances. Again, significant differences are found.

Next, the line strength ratios are converted into relative ionic abundances. It should be noted here that in NGC 5471, the line strengths of certain low ionization species in nucleus B are quite high relative to the other nuclei. This is attributed to the contaminating effects of a supernova remnant at this position. This

Table 5.1

Line Strength Ratios

		5007+4959/4861		3727/5007		6300/5007		6584/3727		6717+6731/3727		3869/5007	
N5471	A	9.18	.07	.188	.007	.0047	.0005	.047	.007	.107	.006	.081	.003
	AL	9.09	.11	...	...	.0033	.0002	...	...	...	...	...	...
	B	5.17	.04	.766	.028	.035	.001	.044	.004	.159	.008	.096	.004
	BL	6.20	.10	...	...	.022	.001	...	...	...	...	...	...
	C	6.04	.06	.442	.016	.0085	.0008	.079	.008	.131	.007	.086	.003
	CL	6.21	.06	...	...	.0087	.0005	...	...	...	...	...	...
	D	8.19	.08	.203	.008	...	...	...	...	...	...	.079	.003
	DL	7.84	.10	.270	.014	.0022	.0002	.056	.006	.102	.006	.094	.008
	IRS	7.44	.21	.276	.012	.0092	.0007	.107	.011	.139	.008	.067	.004
N4214	A	3.97	.03	1.09	.04	.0042	.0012	.062	.004	.097	.005	.051	.003
	AL	4.60	.05	...	...	.0053	.0006	...	...	...	...	...	...
	B	5.96	.05	.572	.021	.0046	.0004	.057	.004	.094	.005	.074	.003
	BL	6.18	.05	...	...	.0034	.0005	...	...	...	...	...	...
	C	4.63	.03	.901	.033	.0068	.0006	.049	.003	.076	.004	.055	.002
	CL	5.20	.06	...	...	.0039	.0004	...	...	...	...	...	...
	N	5.04	.08	.534	.040	.0036	.0011	.080	.010	.131	.013	.077	.007
	NL	4.66	.08	.634	.041	.0077	.0010	.099	.009	.160	.012	...	...
	IRS	4.54	.11	.838	.036	.0089	.0013	.103	.008	.122	.008	.050	.006
N2363	A	10.18	.07	.057	.002	.0010	.0001	.050	.014	.124	.006	.074	.002
	B	10.23	.38	.129	.005	.0016	.0002	.036	.009	.109	.005	.075	.003
	C	7.93	.06	.166	.006	.0030	.0003	.036	.007	.126	.006	.084	.003
	IRS	9.44	.38	.082	.004	.0014	.0003	.158	.024	.144	.010	.066	.003

supernova remnant and its effects on the spectrum at position B will be discussed in detail in chapter VI. Nevertheless, nucleus B is included in the calculations of abundances in this chapter, even though it is clear that the presence of collisional ionization negates the validity of the assumption of a purely photoionized nebula. In this way the effects of contamination by a supernova remnant on standard abundance calculations can be gauged.

The results of the calculations of ionic abundances relative to hydrogen are listed in tables 5.2, 5.3, and 5.4. There are interesting points to be made by comparing the results from different spectrographs, different regions, and different nuclei. The errors reported in these tables represent a propagation of the errors in the line strength measurements, the reddening correction, and the calculated temperature. The calculations were performed in a two step process in order to distinguish the most important contribution to the total error. First, the electron temperature and an associated error were calculated from the [O III] line strengths and the errors in the line strengths derived from both the uncertainties in the profile fitting and the reddening correction. Then, ionic abundances were calculated for the derived temperature and that temperature plus and minus the one sigma error. By comparing the errors for the individual calculations with the range in values for the three calculations at different temperatures, it is possible to determine the chief source of uncertainty. In the tables, the larger

Table 5.2

Ionic Abundances for NGC 5471

position	O^+/H^+ ($\times 10^5$)	O^{++}/H^+ ($\times 10^5$)	N^+/H^+ ($\times 10^7$)	Ne^{++}/H^+ ($\times 10^5$)	He^+/H^+ λ5876	He^+/H^+ λ4471	He^+/H^+ λ6678
A	1.66	9.45	5.71	2.03	.068	.076	.058
	(.07)	(.31)	(.83:)	(.08)	(.0035:)	(.0039:)	(.0086:)
AL	...	10.3	7.77	...	.072	.079	.058
	...	(.36)	(1.0:)	...	(.0020:)	(.0071:)	(.0046:)
B	3.19	4.60	10.9	1.14	.074	.067	.066
	(.24)	(.27)	(.83:)	(.08)	(.0032:)	(.0047:)	(.010:)
BL	...	4.71	11.6	...	.068	.080	.063
	...	(.20)	(.64:)	...	(.0025:)	(.0098:)	(.0070:)
C	3.36	7.75	18.0	1.84	.072	.067	.053
	(.36)	(.74)	(1.6:)	(.19)	(.0030:)	(.0080:)	(.0093:)
CL	...	7.93	18.9	...	.066	.085	.071
	...	(.45)	(1.2:)	...	(.0024:)	(.0091:)	(.0083:)
D	2.13	10.7	...	2.34	...	.068	...
	(.21)	(.94)	...	(.23)	...	(.0082:)	...
DL	3.06	11.3	11.1	2.96	.071	.063	.078
	(.23)	(.71)	(1.1:)	(.24:)	(.0027:)	(.0086:)	(.0088:)
IRS	1.90	7.44	15.2	1.31	.087	.072	.051
	(.15)	(.52)	(1.4:)	(.11)	(.0037:)	(.014:)	(.013:)

Table 5.3

Ionic Abundances for NGC 4214

position	O^+/H^+ ($\times10^5$)	O^{++}/H^+ ($\times10^5$)	N^+/H^+ ($\times10^7$)	Ne^{++}/H^+ ($\times10^5$)	He^+/H^+ $\lambda5876$	He^+/H^+ $\lambda4471$	He^+/H^+ $\lambda6678$
A	11.2	9.2	3.7	1.4	.082	.072	.092
	(.2)	(1.4)	(.45)	(.3)	(.005:)	(.007:)	(.017:)
AL	...	7.3	2.7	...	.086	.083	.062
	...	(.8)	(.2)	...	(.003:)	(.013:)	(.006:)
B	8.3	13.2	2.6	2.9	.074	.078	.072
	(1.2)	(1.6)	(.3)	(.4)	(.002)	(.006:)	(.007:)
BL	...	25.1	4.8	...	.076	.107	.051
	...	(3.7)	(.6)	...	(.003:)	(.011:)	(.006:)
C	11.7	11.6	2.9	1.9	.071	.070	.077
	(1.5)	(1.2)	(.3)	(.2)	(.003:)	(.005:)	(.008:)
CL	...	10.0	2.8	...	.081	.114	.097
	...	(.7)	(.2)	...	(.003:)	(.008:)	(.007:)
N	8.0	13.1	3.2	3.1	.067	...	.084
	(3.1)	(4.3)	.9	(1.1)	(.005:)	...	(.017:)
NL	5.7	8.5	3.3	...	.082	.035	.056
	(1.6)	(2.1)	(.6)	...	(.003:)	(.025:)	(.011:)
IRS	10.1	10.9	5.4	1.6	.086	.058	...
	(3.4)	(3.1)	(1.3)	(.5)	(.006:)	(.021:)	...

Table 5.4

Ionic Abundances for NGC 2363

position	O^+/H^+ ($\times 10^5$)	O^{++}/H^+ ($\times 10^5$)	N^+/H^+ ($\times 10^7$)	Ne^{++}/H^+ ($\times 10^5$)	He^+/H^+ λ5876	He^+/H^+ λ4471	He^+/H^+ λ6678
A	3.3	6.8	1.5	1.3	.079	.072	.062
	(.1)	(.2)	(.4:)	(.1)	(.002:)	(.004:)	(.003:)
B	7.0	6.2	2.1	1.2	.076	.064	.068
	(.3)	(.2)	(.5:)	(.1)	(.002:)	(.005:)	(.004:)
C	7.9	5.6	2.4	1.2	.070	.079	.057
	(.3)	(.2)	(.5:)	(.1)	(.002:)	(.004:)	(.006:)
IRS	4.2	6.1	6.0	1.0	.088	.073	.055
	(.3)	(.4)	(.9:)	(.1)	(.004:)	(.018:)	(.011:)
II	5.1	3.3	...	.3	...	...	...
	(1.1)	(.5)	...	(.1)	...	...	...

of the two errors is always reported. If the error is followed by a colon, then the main source of error lies in the line strength and reddening uncertainties. This is the case for all of the helium abundance calculations because the ratio of hydrogen to helium emissivities varies only slowly with temperature. The other uncertainties are due primarily to the uncertainty in the estimated temperature. In high excitation regions, the uncertainty in temperature is usually due to the uncertainty in the reddening correction. Because of the wavelength difference between λ4363 and λ4959+λ5007, small uncertainties in the reddening correction are amplified into large uncertainties in the temperature estimate. In low excitation regions, the λ4363 line can become so weak that it is difficult to deconvolve from the strong λ4340 hydrogen Balmer line. In these cases, the uncertainty in the line strength of the λ4363 line will become an important factor in determining the uncertainty in temperature.

The effect of the temperature estimate can be seen by comparing the KPNO and Mt. Lemmon measurements for nucleus B in NGC 4214. In Table 5.1, there is excellent agreement between the [O III]/Hβ values for this nucleus. However, the ionic abundances reported in Table 5.3 show a discrepancy of a factor of two. This is attributable to a difference in the λ4363 line strength measurement which has resulted in a temperature estimate difference of 15 percent. This indicates that in some cases the statistical errors calculated by the line

fitting program must be considered to be lower limits to the true uncertainty in the line strength.

Ignoring, for now, the unique properties of nucleus B in NGC 5471, there are many notable points in tables 5.2 - 5.4. In NGC 5471, the N^+ abundance shows excellent agreement between the KPNO and Mt. Lemmon values, but the differences between nuclei span a factor of 3. The O^+ abundance varies by a factor of two in both NGC 5471 and NGC 2363 - a range significantly larger than the 10 percent or less errors would tolerate. The N^+ abundances measured by the IRS are always at the high end of the range for all three of these regions. For the most part, the helium abundances do not show a large range in values typical for the heavier elements.

The main results of the abundance analyses are presented in table 5.5. Here the IIDS values for positions in the three regions have been converted to total chemical abundances. The total oxygen abundance is assumed to be a sum of the O^+ and O^{++} ionic abundances. The nitrogen abundance is calculated by multiplying the N+ abundance by the ionization correction factor of $(O^+ + O^{++})/O^+$. Finally, the neon abundance comes from the Ne^{++} abundance multiplied times the ionization correction factor of $(O^+ + O^{++})/O^{++}$. An alternative way of considering the ionization correction factors is a multiplication of the relative abundances in similar ionization zones times the total oxygen abundance. The relative abundance of N^+/O^+ and Ne^{++}/O^{++} are presented in

Table 5.5

Ionic Abundance Ratios and Total Elemental Abundances

position	N^+/O^+ ($\times 10^2$)	Ne^{++}/O^{++}	$(O^+ + O^{++})/H^+$ ($\times 10^5$)	[N/H] ($\times 10^6$)	[Ne/H] ($\times 10^5$)
			NGC 5471		
A	3.4 (.5)	.22 (.01)	11.1 (.3)	3.8 (.6)	2.4 (.1)
B	3.4 (.4)	.24 (.02)	7.8 (.4)	2.7 (.3)	1.9 (.2)
C	5.4 (.8)	.24 (.03)	11.1 (.8)	6.0 (1.0)	2.7 (.4)
D	... ...	.22 (.03)	12.8 (.9)	... ...	2.8 (.4)
DL	3.6 (.5)	.26 (.03)	14.4 (.7)	5.2 (.8)	3.7 (.5)
IRS	8.7 (1.3)	.18 (.02)	9.3 (.5)	8.1 (1.3)	1.7 (.2)
IRS c(Hβ)=.5	4.6 (.5)	.23 (.02)	7.9 (.4)	3.6 (.4)	1.8 (.2)
			NGC 4214		
A	3.3 (.7)	.15 (.04)	20.4 (1.4)	6.9 (1.8)	3.2(1.0)
B	3.1 (.5)	.22 (.03)	21.5 (2.0)	6.8 (1.3)	4.8 (.8)
C	2.5 (.4)	.17 (.03)	23.3 (1.9)	5.8 (1.1)	3.9 (.8)
IRS	5.4 (2.2)	.15 (.07)	21.0 (4.6)	11.3 (5.4)	3.2(1.7)
			NGC 2363		
A	4.4 (1.2)	.18 (.01)	7.2 (.2)	3.2 (.9)	1.3 (.1)
B	3.1 (.7)	.19 (.01)	7.0 (.2)	2.2 (.5)	1.3 (.1)
C	3.1 (.6)	.21 (.01)	6.4 (.2)	2.0 (.4)	1.3 (.1)
IRS	14.2 (2.3)	.16 (.02)	6.5 (.4)	9.2 (1.6)	1.0 (.2)

table 5.5 along with the calculated total abundances.

The internal consistency for the oxygen abundances for each GEHR is really quite striking. This is strong support for the assumption that oxygen abundances are constant throughout a GEHR, and the credibility of this method of measuring the total oxygen abundance. The only exception to this is the IRS value for NGC 5471. The discrepancy is attributable to a higher value of the electron temperature.

The scatter in the neon abundances is significantly larger, as might be expected due to the weaker line strengths, the greater dependency on the reddening correction, and the necessity of the ionization correction factor. It may be significant that the IRS measurements give the lowest values of the total neon abundance for all three GEHRs.

It is the total nitrogen abundance values that show the largest scatter. There are a number of potential sources of error to cause this scatter, besides actual differences in the nitrogen abundance. Although the proximity of the [N II] lines λ6548 and λ6584 to Hα almost completely eliminates any dependence on the reddening correction, the ionization correction factor, based on the λ3727 line is strongly influenced by the reddening correction. To demonstrate this, a second abundance analysis was run on the IRS spectrum of NGC 5471 with a value of c(Hβ) consistent with the small aperture

observations. As shown in table 5.5, this results in a reduction of the total nitrogen abundance by more than a factor of two. The large value of the nitrogen abundance for the IRS measurement in NGC 2363 may be partially due to instrumental effects. The nitrogen lines are very weak and the line fitting routine may be attributing flux from the shoulders of the λ6563 line to the nitrogen lines. On the other hand, the large difference between the small aperture results may be quite real, as the errors suggest. Kennicutt, Balick and Heckman (1980) observed nucleus A with the KPNO IIDS, but used a larger aperture covering twice as much area. Their data, when reduced in an identical fashion, yield ionic and total nitrogen abundances of more than a factor of two greater than the abundances from the small aperture observations reported here. This observation, combined with the fact that the IRS nitrogen abundances are always the largest for an individual GEHR, implies that the calculated nitrogen abundance is strongly dependent on the ratio of aperture size to H II region size.

Interpretation

The observations and calculated abundances outlined in the last section have shown significant variations in emitted spectra and abundances in every GEHR observed. These point to point differences are somewhat surprising. Two questions are prompted by the data: What is(are) the physical cause(s) for the differences in the emitted spectra, and can the different methods of abundance calculations properly deal with these variations in physical conditions?

The first observation needing explanation would be the strong radial gradient observed in all of the Hα/[O III] ratio maps. This can be interpreted as a temperature gradient, ionization structure, or a combination of both. There is insufficient data to distinguish between these choices unambiguously, however, certain clues do exist. To first order, the temperature in the gas is determined by the abundances of the heavy elements that are responsible for cooling. Again, to first order, changes in the ionization structure are due to changes in the radiation field. For this reason, it might be more reasonable to expect that the Hα/[O III] gradient is due to ionization structure. The range of Hα/[O III] values shown in the image ratio maps covers a factor of two. Interpreted as strictly a temperature difference, this would indicate a range in temperature of about 2000K. This range for the Hα/[O III] ratio is roughly equal to the range of values determined from the small aperture spectrophotometry, yet the maximum range of temperatures derived for the nuclear positions in a single GEHR is only about 1000K. An attempt was made to observe temperature variations directly by obtaining an image of NGC 2363 in the light of [O III] λ4363. The resultant λ4363/λ5007 image is shown in figure 5.4. The contour levels, set at 10, 20, 40, and 80 percent of the total image ratio, show variations of as much as 50 percent in the central parts of the region. This would correspond to variations of about 2000K, but these results must be regarded as preliminary. The relatively small equivalent width of the λ4363 line makes these results very

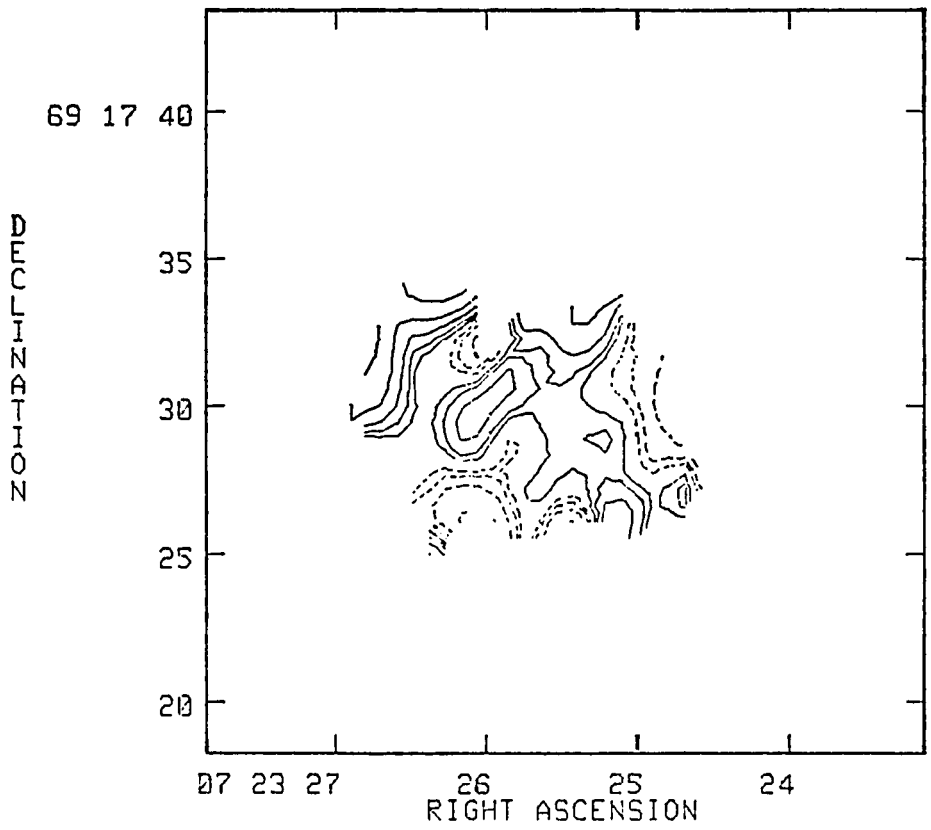

Figure 5.4 λ4363/λ5007 Ratio Map for NGC 2363

A contour map representation of the λ4363/λ5007 ratio for NGC 2363. The solid contours are positive and the dashed contours are negative. The image has been offset so that the zero point in the map corresponds to the image mean. The contour intervals correspond to intervals of 5, 10, 20, 40, and 80 percent of the image mean.

susceptible to continuum subtraction errors. It was also found that the ratio map changed significantly with alignment errors of only one half of a pixel. Finally, the signal to noise ratio in the outer parts of the nebula was much too small to allow a search for a radial gradient.

If the observed Hα/[O III] gradient is due to ionization structure, then there should be gradients in the strengths of other forbidden lines. Optical imaging is not available for these other emission lines, but this trend may be reflected in differences between the large and small aperture spectrophotometry. In fact, there is a systematic difference for the [Ne III] and [N II] lines, but not for the [O II] line and, surprisingly, not for the [O III] line. In sum, there is evidence in support of ionization structure, but a temperature gradient cannot be ruled out.

If point-to-point differences in the temperature are the major cause of the observed variations in the Hα/[O III] ratio, then the abundance analysis technique of Peimbert and Costero is appropriate, and can be used to measure the affects of temperature variations on calculated abundances. Table 5.6 lists the results of several abundance calculations for the IIDS spectra of one nucleus in each of three GEHRs. The first column lists the results of the calculations described so far. The next four columns show the results of abundance calculations following the method of Peimbert and Costero with increasing values of the fractional mean squared temperature

Table 5.6

A Comparison of Abundance Calculation Methods

Abundance	one zone	t^2=0.0	t^2=0.01	t^2=0.03	t^2=0.06
		NGC 5471 A IIDS			
O^+/H (x 10^5)	1.66	1.77	1.87	2.19	2.86
O^{++}/H (x 10^5)	9.45	10.94	11.70	13.49	17.22
N^+/H (x 10^7)	5.71	5.65	5.99	6.79	8.43
Ne^{++}/H (x 10^5)	2.03	2.39	2.57	3.00	3.89
[O/H] (x 10^5)	11.11	12.68	13.57	15.69	20.08
[N/H] (x 10^6)	3.82	4.13	4.34	4.85	5.91
[Ne/H] (x 10^5)	2.39	2.77	2.98	3.49	4.54
		NGC 2363 A IIDS			
O^+/H (x 10^5)	0.33	0.38	0.40	0.45	0.55
O^{++}/H (x 10^5)	6.84	8.65	9.11	10.16	12.20
N^+/H (x 10^7)	1.46	1.55	1.63	1.79	2.10
Ne^{++}/H (x 10^5)	1.26	1.59	1.69	1.90	2.31
[O/H] (x 10^5)	7.17	9.03	9.50	10.60	12.70
[N/H] (x 10^6)	3.14	3.74	3.88	4.22	4.88
[Ne/H] (x 10^5)	1.32	1.66	1.76	1.98	2.42
		NGC 4214 A IIDS			
O^+/H (x 10^5)	11.19	10.39	11.66	14.97	23.30
O^{++}/H (x 10^5)	9.21	9.15	10.14	12.70	18.93
N^+/H (x 10^6)	3.66	3.18	3.48	4.24	6.04
Ne^{++}/H (x 10^5)	1.42	1.49	1.67	2.13	3.29
[O/H] (x 10^5)	20.40	19.50	21.80	27.70	42.20
[N/H] (x 10^6)	6.67	5.98	6.50	7.83	10.95
[Ne/H] (x 10^5)	3.15	3.18	3.59	4.64	7.33

fluctuation (t^2). In theory, the first two columns should be identical, and, in fact, the agreement is generally good. The differences are largest for NGC 2363 and smallest for NGC 4214. This is as expected as the interpolation formulae of Peimbert and Costero were derived for the temperature range of 5000K to 10000K. The important point of table 5.6 is the growth of the abundances with an increase in the value of t^2. It is true that for a value of t^2 less than or equal to 0.01, temperature fluctuations will not significantly alter the results of abundance calculations. However, for larger values of t^2, abundances are seriously underestimated if the effects of temperature variations are not taken into account. Knowledge of temperature variations in H II regions is very limited, and even the results for the best studied region, the Orion Nebula, are uncertain. Peimbert and Costero (1969) derived a value of t^2 = .055 for Orion, but Peimbert and Torres-Peimbert (1977) derived a value of t^2 = .035. A more recent study based on IUE observations, has resulted in a value of t^2 = .016 (Torres-Peimbert, Peimbert, and Daltabuit 1980). Considering the simplicity of the Orion nebula in comparison to the typical GEHR, in would not be unreasonable to expect temperature variations large enough to significantly affect the abundance estimates in GEHRs.

The effects that variations in ionization structure can have on chemical abundance analysis are strongly dependent on nebular geometry, and therefore are not predictable in a way comparable to

the effects of temperature variations. If there is a radial gradient in the ionization structure, then the line strengths of the lower ionization species should increase with increasing aperture size. The calculated temperature would not be expected to change with aperture size. Thus, the calculated ionic abundances of the low ionization species should increase with increasing aperture size. However, the relative abundances should not be affected. For example, the N^+ and O^+ abundances should increase with increasing aperture size, but the N^+/O^+ ratio, and therefore the N/O ratio, should remain constant. In fact, the N+ abundance is observed to increase with increasing aperture size, but the O^+ abundance does not show this trend. Thus, the N^+/O^+ ratio is not constant, and, as can be seen in table 5.5,it is systematically larger in the large aperture measurements.

There are several possible explanations for the systematic difference in the N/O ratio between the large and small aperture observations. Random observational errors can be ruled out as a cause because the difference is seen in all of the GEHRs. The fact that the reddening determined from the large aperture observations is systematically smaller than the reddening from the small aperture observations suggests the reddening correction as a possible explanation. The difference in c(Hβ) could account for most of the difference in N/O in NGC 5471, but is less likely for NGC 4214 and highly inadequate for NGC 2363. It could be that the volume

fractions of N^+ and O^+ are not equal, i.e. the two ionic species are not coexistent. However, the theoretical work of Rubin (1983) predicts a trend opposite to the one observed here. Perhaps a more likely explanation is a variation in temperature in the low ionization zone. In the temperature range of interest, the ratio of the O^+ to N^+ emissivities varies approximately as temperature to the 1.7 power. Thus, for a given observed $I(\lambda6584)/I(\lambda3727)$ ratio, the calculated N/O ratio decreases with decreasing estimated temperature. If the temperature in the low ionization zone is overestimated, the N/O abundance will be overestimated. Perhaps the N^+/O^+ variation can be used to argue in favor of a temperature gradient.

It is now clear that a one zone model interpretation of the spectrum of a GEHR can produce erroneous abundance ratios. Model calculations (Searle 1971, Stasinska 1980, French and Grandi 1981) have shown that in low metallicity H II regions the temperature in the low ionization zone is less than the temperature in the high ionization zone. If this is true, then assuming the same temperature in both zones will especially affect the N^+/O^+ abundance ratio. The result will be an overestimate of the N^+/O^+ ratio. Can abundance estimates based on two zone models adequately compensate? As noted earlier, due to the weakness of the [N II] $\lambda5755$ line, a direct measurement of the temperature in the low ionization zone is rarely practical. Kunth and Sargeant (1983) calculate a temperature for the low ionization zone by combining the derived [O III] temperature with

an estimate of the total oxygen abundance to calculate the effective temperature of the exciting stars. With this, they then use model H II region calculations to determine the temperature in the low ionization zone. If such a scheme is used, will the observed abundance anomalies disappear? This can be answered by further inspection of nuclei A and C in NGC 5471. From table 3.1 it is found that the estimated effective stellar temperatures are 42,500K and 37,500K respectively. The [O III] temperatures are 12,850 and 12,050. From table 5.2, the N^+ abundances are 5.71×10^{-7} and 18.0×10^{-7}. It is possible that the difference in in the calculated nitrogen abundance could be attributable to the differences in the effective temperatures of the exciting stars (and therefore a difference in the temperature of the low ionization zone). Table 5.7 shows the results of three model calculations by Stasinska (1980). These calculations show the effect of changing the effective temperature of the exciting stars for a gas of one tenth solar metallicity. The changes in the low ionization zone temperature are less than the changes in the high ionization zone. The difference between the temperatures in the two zones increases with increasing temperature. If the real abundances were identical in the two nuclei, one would expect that the calculated nitrogen abundance would be greatest in the higher temperature nucleus A. This is, of course, just opposite to what is observed. It can be concluded that, in this case, estimating a lower temperature in the low ionization zone will

an estimate of the total oxygen abundance to calculate the effective temperature of the exciting stars. With this, they then use model H II region calculations to determine the temperature in the low ionization zone. If such a scheme is used, will the observed abundance anomalies disappear? This can be answered by further inspection of nuclei A and C in NGC 5471. From table 3.1 it is found that the estimated effective stellar temperatures are 42,500K and 37,500K respectively. The [O III] temperatures are 12,850 and 12,050. From table 5.2, the N^+ abundances are 5.71×10^{-7} and 18.0×10^{-7}. It is possible that the difference in in the calculated nitrogen abundance could be attributable to the differences in the effective temperatures of the exciting stars (and therefore a difference in the temperature of the low ionization zone). Table 5.7 shows the results of three model calculations by Stasinska (1980). These calculations show the effect of changing the effective temperature of the exciting stars for a gas of one tenth solar metallicity. The changes in the low ionization zone temperature are less than the changes in the high ionization zone. The difference between the temperatures in the two zones increases with increasing temperature. If the real abundances were identical in the two nuclei, one would expect that the calculated nitrogen abundance would be greatest in the higher temperature nucleus A. This is, of course, just opposite to what is observed. It can be concluded that, in this case, estimating a lower temperature in the low ionization zone will

Table 5.7

Results of Changing Stellar Effective Temperature

On Model H II Region Temperatures

model	T_{eff}	T (O III)	T (O II)
EB2	37,500	12,320	11,810
EC2	40,000	12,870	11,970
ED2	45,000	13,570	12,660

not erase the abundance discrepancy. In general, the additional work of estimating temperatures for the low ionization zone will not significantly alter the chemical abundance analysis results.

Conclusions

Having now made the observation that real differences in emission line ratios exist within single GEHRs, that the physical reasons for these differences cannot be unambiguously determined (even by studies designed to do just that), and that the results of abundances analysis can depend on the size and position of the entrance aperture of the spectrograph, it is now appropriate to comment on the relevance of these conclusions to other GEHR research.

To start with the positive, it is noted that the calculated oxygen abundances in all three GEHRs are consistent for all spectrographs used. The standard abundance calculation techniques appear to work quite well for oxygen. On the other hand, the nitrogen abundances show a large scatter. Nitrogen abundances in GEHRs have been the center of a controversy. The point of contention is the relationship between the nitrogen to oxygen ratio and the total oxygen abundance. If nitrogen is a secondary product of stellar nucleosynthesis, as suggested by Talbot and Arnett (1974), then the N/O ratio should be proportional to the O/H ratio. The relative abundances of primary products are constant for all metallicities. Smith (1975), Edmunds and Pagel (1978), Alloin et al.

(1979), and Lequeux et al. (1979) all studied the N/O versus O/H relationship for GEHRs and all found a large scatter, but also a general trend arguing for a combination of both primary and secondary nucleosynthetic origins for nitrogen. Kunth and Sargent (1983) also found a large scatter, but noted that a line drawn from the value derived for Orion to the center of gravity of their results for GEHRs had a slope of 1.0 - consistent with nitrogen being solely a secondary nucleosynthetic product. The results of this study imply that it is likely that the large scatter in N/O abundances may be due to observational effects. If it is possible to get factor of three differences for the nitrogen abundance in a single GEHR for which the oxygen abundance is well constrained, it is likely that any studies of the N/O abundance ratio will be swamped by observational and interpretive error. Fine tuning of the abundance analysis by including estimates of the temperature variations or employing two zone model calculations are not likely to improve the results.

Lastly it is interesting to compare the results of this study to others. In this way, it is possible to better gauge the effects of using different aperture size/spectrograph set-ups. NGC 5471 is the most studied of all objects studied here, and table 5.8 lists the results of a number of studies. The results confirm the earlier conclusions that the value of c(Hβ) is dependent on both the aperture size and which Balmer lines are used in the measurement. The values

Table 5.8

A Comparison with Published Data for NGC 5471

observation	aperture (arc sec)	c(Hβ)	T(O III) (K)	O^{++}/H^{+} (x 10^{5})	He^{+}/H^{+} (λ5876)	Hα used?
A	4.2	.54	12,850	9.5	.068	no
AL	4.7	.18	12,500	10.3	.072	yes
IRS	22.0	.07	13,000	7.4	.087	yes
S+S[1]	7	.18	12,050	9.9	.062	yes
S+A[1]	2x4	.1	12,900	9.7	.065	yes
RPT[1]	3.8x12.4	.40	12,400	10.3	.072	?
McC[1]	4	.25	11,450	13.7	.077	yes
DRW[1]	2x4	.50	13,300	8.4	.061	no

([1]S+S = Shields and Searle 1978; S+A = Sedwick and Aller 1981; RPT = Rayo, Peimbert, and Torres-Peimbert 1982; McC = McCall 1982; DRW = D'Odorico, Rosa, and Wampler 1983)

of the temperature show a range of almost 2000K. The O^{++} abundance was chosen for comparison because it is almost independent of reddening corrections, and the He^{+} abundance because it is very insensitive to the temperature. Both ionic abundances show a large range of values. Although observational errors may account for some of the differences, it is probable that differences in aperture coverage and the methods of dereddening the spectra are the primary sources of the differences in table 5.8.

Chapter VI SNRs and WRs in GEHRs

One of the points emphasized in the last chapter was the necessity of a good understanding of the physical conditions in GEHRs in order to make accurate measurements of chemical abundances. Perhaps the most uncertain aspect of the physical conditions in GEHRs is their kinematics. All GEHRs that have been observed at sufficient kinematic resolution have shown anomalously large turbulent velocities. The energy source necessary to support these large turbulent velocities is a matter of debate. As stated in the introductory chapter, supernova remnants (SNRs), stellar winds from Wolf-Rayet (WR) stars, large scale flows due to gas pressure gradients, and the gravitational binding energy of the entire H I/H II complex have all been suggested as potential energy sources for the observed anomalous kinematics. The material in this chapter represents a sensitive search for the presence of SNRs and WR stars in GEHRs. The study of these objects is important beyond providing clues to the nature of the anomalous kinematics of GEHRs. It was shown in the last chapter the SNRs can significantly complicate the abundance analysis in GEHRs. On a scale much larger than the present study, information about SNRs may allow a statistical tool for studying the high mass end of the initial mass function for star formation. The study of the presence of WR stars also may help in the understanding of massive star evolution. For example, objects with the spectra of WR stars are presently candidates for the title

of most massive stars in the universe. This chapter will be divided into separate sections on SNRs and WRs.

SNRs in GEHRs

The Expected Supernova Rate

One can begin with the question, 'Are supernova remnants expected to be an important component in GEHRs?' To answer this one needs to estimate the expected supernova rate, the mechanical energy output and the radiative luminosity of a typical supernova. Throughout this discussion, supernovas will be synonymous with Type II supernovas; the explosive event resulting from the collapse of a massive population I star. Supernova remnant will be synonymous with the evolved type supernova remnant associated with type II supernovas.

In order to predict a supernova rate, one needs to know the initial mass function (IMF) for star formation, a minimum mass of a supernova progenitor star, the star formation rate (SFR), and the duration of the star formation period. Uncertainties in all of these quantities are large, and numerous assumptions will be needed. However, as will be seen, it appears that a reasonably believable estimate can be made.

One such calculation has been carried out by Bevenuti, D'Odorico, and Dumontel (1979) (BDD) in which the GEHR NGC 604 was modeled. Their calculation made the assumption of a steady state in which the initial mass function as determined by Lequeux (1979) is maintained by continuous star formation. Given a fixed distribution of stellar types and knowledge of the stellar lifetimes and uv flux distributions, it is possible to derive a supernova rate as a function of observed Hβ flux and progenitor mass cutoff. This result can be expressed as the ratio of the observable Hβ flux produced by the massive stars to the supernova rate of these same stars. BDD derive values of 2.5×10^{42} erg(Hβ)/s/SN/yr for a cutoff of 8 solar masses, and a value of 8.5×10^{41} erg(Hβ)/s/SN/yr for a cutoff of 5 solar masses.

Rieke et al. (1980) performed a series of calculations in order to model the intense burst of star formation in the nucleus of M82. In their models, the IMF, the SFR, and the time since the onset of star formation were all free parameters. The star formation rate was modeled as a single burst with an exponentially decaying SFR. Models were calculated over a large range in IMF, and a progenitor mass cutoff of 6 solar masses was used. Given the large range of input values, it is surprising that the results yield a very narrow range of $2 - 8 \times 10^{41}$ erg(Hβ)/s/SN/yr. The fact that these two very different methods yield comparable results implies that expected supernova rates are not very sensitive to input model conditions.

From these calculations a value of 8 10^{41} erg(Hβ)/s/SN/yr can be assumed to be valid to within a factor of three. Now, from the Hβ photometry of Melnick (1979), supernova rates can be calculated for the GEHRs studied here. Values of .0068, .0060, .0034, and .0003 supernova/year are derived for NGC 5471, NGC 2363, NGC 2403 #1, and Hubble V. These values can be multiplied by a visibility window to determine the number of visible SNRs that should reside in each GEHR. The canonical lifetime of an SNR is 10^4 years, so there should be 68, 60, 34, and 3 supernova remnants contributing to the luminosity of the GEHRs named above. Even though these calculations are believed to have a minimum uncertainty of a factor of three, they provide a strong case for investigating the importance of SHRs in GEHRs.

Detectability

The observations of SNRs in the Magellanic Clouds allow an estimate of the requisite sensitivity for radio searches for extragalactic SNRs. Milne, Caswell, and Haynes (1980) (MCH) have compiled 5 GHz observations for 15 SNRs in the Large Magellanic Cloud (LMC). Their sample has an average integrated flux density of 750 mJy with a maximum of 3.98 Jy (30 Dor B). Adopting 55 kpc as the distance to the LMC, their average value can be converted to a benchmark value of 2.3mJyMpc^2. Thus, at the distance of M101, the average of their sample would have a flux density at 5 GHz of only 0.04 mJy. This is slightly less than the value of the r.m.s. noise in the 5 GHz maps in the present study. The situation is much better

for the M81 group galaxies where the average MCH SNR would have a flux density of 0.3 mJy. Still, considering that the sample of MCH represents the high end of the SNR radio luminosity function, the VLA maps should only be able to detect the most luminous of the SNRs in the candidate GEHRs.

Of course, the real problem is discerning the presumably non-thermal radio continuum from the thermal radio emission emitted by the H II region. A supernova remnant like 30 Dor B is strong enough to be separated from the H II region by its non-thermal spectrum, even at the distance of M101. However, the average SNR would not be identifiable in this manner. Besides being able to pick out individual SNRs, it is possible to derive limits to the total contribution to the radio continuum emission by SNRs. Although individual SNRs may be below the detection threshold, the combined emission of several SNRs may show up as a slightly non-thermal global radio spectrum.

Optically, collisionally heated nebulae such as SNRs are generally separated from H II regions by the $(\lambda6717+\lambda6731)/\lambda6563$ emission ratio. In H II regions this ratio varies between 0.01 and 0.1, while typical values for SNRs range from 0.4 to 1.0. Thus, being able to pick out SNRs embedded in H II regions via optical spectrophotometry depends on the ratio of the H II region emission to the SNR emission. There is no reasonable way to quantify the expected sensitivity using this method, because it is strongly

dependent on the geometry of the emitting regions.

SNR Candidates in GEHRs

Of the GEHRs described so far, the strongest case for the presence of an SNR is provided by NGC 5471 B. This nucleus has both a non-thermal radio spectrum, and significantly enhanced [S II] emission. These observations are most easily accounted for by the presence of a supernova remnant. For the rest of the discussion it is assumed that there is an SNR at the position of NGC 5471 B. Next, an attempt is made to calculate physical properties of the SNR.

A detailed analysis of the supernova remnant is dependent upon separating its spectrum from the surrounding nebulosity. This is all but impossible. It is possible, however, to assume that nucleus B would be comparable to the other nuclei if the SNR were absent. Investigating differences between the nuclei might yield information about the SNR.

The radio flux and spectral index of the SNR can be estimated by comparing the radio maps with the Hα map. Assuming the extinction corrected Hα/radio continuum flux ratio is a constant for all the thermal radio radiation, and that the Hα flux of nucleus B is all due to the thermal component, an estimate of the (minimum) non-thermal radio flux of the SNR at λ6 cm and λ20 cm can be made. This assumption produces a flux density for the non-thermal component of 2.1 +/- 0.8 mJy at 1420 MHz and a spectral index (α) of -0.7 +/- 0.3.

This would place the SNR among the most powerful known radio emitting SNRs, with a radio luminosity at 1420 MHz 5 times more powerful than Cassiopeia A (Parker 1968; $\alpha = -.77$), 9 times stronger than N132 D (Mathewson and Clarke 1973; $\alpha = -.65$) and about one third the strength of the SNR in NGC 4449 (Seaquist and Bignell 1983; $\alpha = -.62$).

Divining the optical spectrum of the SNR is yet more treacherous. Table 6.1 shows the results of a comparison of the spectrum of nucleus B to the spectra of the other nuclei. The comparison was constructed by finding the difference between the line strengths of nucleus B and the other nuclei (normalized to Hβ) and then normalizing the difference by dividing by the strength of the line in the nucleus being compared. In this way a list of enhanced/weakened lines is produced. The results for lines showing differences of more than 10 percent are listed in table 6.1. In order to better interpret the results, the spectrum of the SNR in NGC 6822 (D'Odorico and Dopita, 1983) is compared to the average spectrum of the H II regions Hubble V and Hubble X in NGC 6822 (Lequeux et al. 1979; Pagel, Edmunds, and Smith 1980). By using a comparison of H II regions and an SNR observed in a low abundance enviroment, it is hoped that the abundance effects can be minimized. The chemical abundance has been shown to be the primary factor in determining the spectrum of an evolved type extragalactic SNR (Dopita et al. 1984).

Table 6.1

Evidence of SNR Emission

line	IIDS (B - A)/A	IIDS (B - C)/C	IIDS/MT. L. (B - D)/D	NGC 6822 (SNR-HII)/HII
[O II] λ3727	+130%	+47%	+140%	+130%
[S II] λ4068+λ4076	+190%	+82%	+44%	...
[O III] λ4363	-38%	+14%	-13%	...
[O III] λ5007	-44%	-14%	-36%	-85%
[O I] λ6300	+320%	+250%	+670%	+6600%
[N II] λ6584	+110%	-18%	+76%	+270%
[S II] λ6716	+220%	+73%	+160%	+680%
[S II] λ6731	+270%	+89%	+160%	+1100%

The analysis of the optical spectrum of the SNR can start with a discussion of what is not present in the spectrum. There is no evidence for lines broader than the instrumental resolution (~ 300 km/s). If this SNR had a broad component only one tenth as luminous as the SNR in NGC 4449, it would easily be detected in these measurements. The largest differences between the spectrum of nucleus B and the other nuclei are found at λ6300. This is as would be expected from the results of the NGC 6822 comparison. The [S II] lines also show the same trend of enhancement. The [N II] and [O II] lines are enhanced, but the difference is not as large. Of the three other nuclei, nucleus B is most like nucleus C. The gas in the local environment of the SNR is not being kept completely ionized by the surrounding stars as evidenced by emission from the neutral species of oxygen (λ6300 and λ6363) and magnesium (λ4562 and λ4571). Further discussion of the optical emission of the SNR is difficult. It is safe to say that the derived optical spectrum is similar to that of a typical 'old' SNR, [e.g. the Cygnus Loop (Miller 1974) and 30 Dor B (Danziger et al. 1981; Gilmozzi et al. 1983)], by virtue of the strong [O I], [S II] and the detection of [Mg I].

Since it is easily possible for an SNR to remain undetected and yet subtly alter estimates of physical conditions and chemical compositions, it would be convenient to have a test for the presence of SNRs. Baldwin, Phillips, and Terlevich (1981) (BPT) have discussed diagnostic diagrams for distinguishing the excitation

mechanisms in extragalactic emission line objects. The different nuclei in NGC 5471 do not distinguish themselves in the <E> parameter developed in BPT. However, in a plot of λ6300/λ5007 versus λ3727/λ5007 (as suggested by Heckman (1980) for distinguishing Seyfert nuclei from LINERs) nucleus B does stand out as strongest of all positions observed in NGC 5471 in both ratios.

Figure 6.1 shows the plot of λ6300/λ5007 versus λ3727/λ5007. The nuclear and core spectra are indicated by letters. For comparison, the metal poor galaxies of KS and the emission line galaxies of French (1980) are also included. The regions of Seyfert nuclei and LINERs come from Heckman (1980) and the boundaries for planetary nebulae and H II regions are from BPT. The high luminosity galaxies of French occupy the same region of the diagram as nucleus B. Despite the fact that the [O III] temperatures for the high luminosity galaxies are lower than the temperature of nucleus B, there is evidence for supernova remnants in two of them. This intriguing coincidence will be discussed again in chapter VIII.

NGC 2363 is another promising candidate for suspected SNRs in a GEHR. The radio spectrum is nonthermal throughout the region, and relatively constant. The spectral index of -0.4 +/- 0.1 for the entire region agrees well with the value of -0.5 +/- 0.24 (derived from 2.8 and 11 cm measurements) reported by Klein, Grave and Wielebinski (1983). If the nonthermal spectral index were due to SNRs, nonthermal point sources would be expected. The fact that the

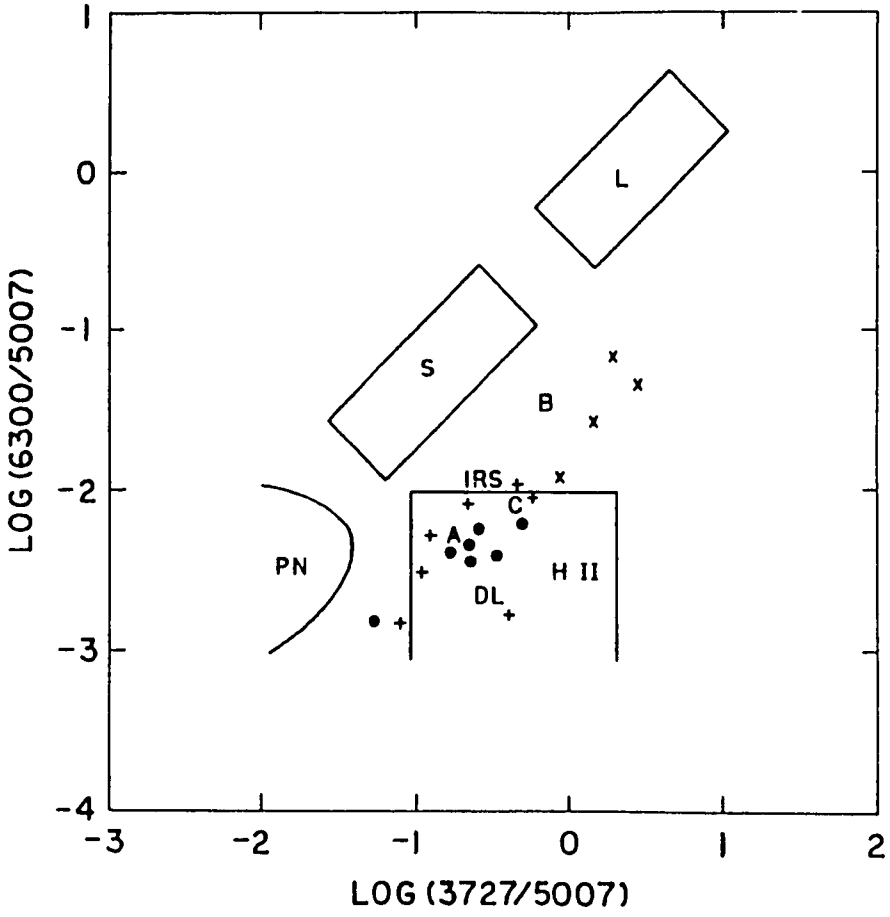

Figure 6.1 Oxygen Line Ratios Diagnostic Diagram

A plot of the [O I]/[O III] line strength ratio versus the [O II]/[O III] line strength ratio as used by Heckman (1980) to distinguish between heating by photoionization and heating by shocks. Planetary nebulae (PN), Seyfert galaxies (S), LINERs (L), and H II regions (H II) all occupy different regions in such a graph. The spectra at different positions in NGC 5471 are marked with letters. The H II galaxies of Kunth and Sargent (1983) are marked with +'s, the low luminosity galaxies of French (1980) with .'s and the high luminosity galaxies of French with x's.

entire region shows nonthermal emission suggests the presence of several SNRs. These inferred SNRs may be partially resposible for the very high [O III] temperature measured in NGC 2363. On the other hand, there is no evidence of enhanced [O I] or [S II] emission. Also, all of the spectrophometric observations yield oxygen line ratios that fall in the normal H II region area of a λ6300/λ5007 versus λ3727/λ5007 diagnostic diagram. Perhaps these two tests are not reliable detectors of SNRs.

Hubble V is similar to NGC 2363 by virtue of a nonthermal radio spectral index and a lack of enhanced [O I] and [S II] emission. Klein, Grave, and Wielebinski reported a spectral index of -0.20 +/- 0.11 for Hubble V. By combining the λ6 cm map reported here with a λ21 cm continuum map of NGC 6822 (Skillman unpublished), a value of -0.21 +/- 0.04 is derived for Hubble V. Small aperture spectrophotometry of Hubble V has been conducted by Smith (1975), Lequeux et al. (1979), and Pagel, Edmunds and Smith (1980). There is no evidence of enhanced emission in the [S II] or [O I] lines in any of their measurements. Although the radio spectral index of Hubble V is less negative than that of NGC 2363, both present the problem of nonthermal radio emission with no identifiable optical SNRs.

SNRs and Abundance Calculations

The effects of the presence of an SNR on standard abundance calculations will be examined here in two different ways. The first method is to simply compare the abundances derived from standard abundance analysis calculations for nucleus B in NGC 5471 with the abundances derived for the other nuclei. Under the assumption that the abundances are homogeneous throughout the NGC 5471, this allows a direct measure of the effects of the SNR detected there. A second method consists of synthesizing spectra from a combination of an H II region spectrum and an SNR spectrum, and then analyzing the composite spectra with standard abundance analysis.

The results of the standard abundance analysis calculations for nucleus B in NGC 5471 are shown in tables 5.2 and 5.5. The calculated ionic abundances are dependent on both the estimated temperature and the measured line strength. For nucleus B the presence of the SNR has resulted in an estimated temperature higher than the surrounding nuclei. For a constant line strength, this will have the effect of lowering the calculated ionic abundances. This effect is seen in the O^{++} and Ne^{++} abundance determinations which are lower for nucleus B than for any of the other positions. The line strength for O^{+} is stronger at position B than at the other positions. Thus the effects of increased estimated temperature and increased line strength tend to offset each other in the calculated O^{+} abundance. The picture for both O^{+} and N^{+} is a somewhat confused

one. Both show a large range of values from nucleus to nucleus. Thus it is difficult to assess the impact of the SNR on the N^{+} and O^{+} ionic abundance calculations for nucleus B. For the total elemental abundance measurements, the dominant effect is the increased estimated temperature which lowers the O^{++} abundance. Since most of the oxygen is in the O^{++} state, this lowers the calculated total oxygen abundance. Because the calculations of the total nitrogen and neon abundances are based on the total oxygen abundance, this, in turn, causes the calculated total nitrogen and neon abundances for nucleus B to be the lowest of all of the nuclear positions.

The results of the second investigation are shown in table 6.2. Here the spectrum of NGC 5471 from Rayo, Peimbert, and Torres-Peimbert (1982) has been combined with the spectrum of an SNR in IC 1613 (Dopita and D'Odorico 1983). The SNR in IC 1613 was chosen because it has the best published spectra of an SNR with a metallicity of one tenth of solar. NGC 5471 has a comparable metallicity. Both spectra were dereddened and normalized to Hβ. Then the two spectra were added after weighting by a multiplicative constant. As the table reads from left to right, each column shows the results of a standard abundance calculation, each with increasing influence by the SNR. The first two parameters listed are the calculated [O III] temperature and the observed [S II]/Hα (λ6717+λ6731/λ6563) ratio. The estimated temperature rises steadily

Table 6.2

The Affects of a SNR on Abundance Calculations

parameter	RPT	RPT+.01SNR	RPT+.1SNR	RPT+1SNR	5471 B
T(O III)	12,424	12,414	12,512	13,448	13,450
[S II]/Hα	.051	.054	.073	.175	.172
$O^+/H^+ \times 10^5$	2.1	2.1	2.1	1.7	3.2
$O^{++}/H^+ \times 10^5$	10.3	10.2	9.2	4.2	4.6
$N^+/H^+ \times 10^7$	7.6	7.7	8.5	11.4	10.9
$He^+/H^+ \times 10^2$	7.4	7.4	7.3	6.9	7.4
$N^+/O^+ \times 10^2$	3.6	3.7	4.0	6.7	3.4
$O/H \times 10^5$	12.4	12.3	11.3	5.9	7.8
$N/H \times 10^6$	4.5	4.5	4.6	4.0	2.7

as the influence of the SNR increases. The [S II]/Hα ratio is frequently used to distinguish extragalactic SNRs from extragalactic H II regions (e.g. Dopita, D'Odorico and Benvenuti 1980). Usually an [S II]/Hα ratio of more than 0.4 is assumed to indicate the presence of an SNR. As can be seen from the table, the effects of the SNR on the abundance determination are very small if the luminous output of the SNR is one tenth or less of the H II region. However, when the SNR puts out a comparable amount of optical emission, the affects are quite noticeable. The addition of the SNR lowers the total and ionic oxygen abundances and raises the ionic nitrogen abundance.

The results for NGC 5471 B are also listed in the table. It is intriguing that the values of the [O III] temperature and the [S II]/Hα ratio show such a good agreement. The results for N^+/H^+ and O^{++}/H^+ are also quite good. The major difference between the NGC 5471 B spectrum and the 50%/50% SNR-H II composite spectrum is the large discrepancy in the O^+/H^+ ratio.

It is important to note that even when the SNR is responsible for half of the Hβ flux, the [S II]/Hα ratio is still a factor of two below the canonical cutoff indicating the presence of an SNR. At this level of contamination by the SNR, the calculated oxygen abundance has been decreased by more than 50 percent and the calculated total nitrogen abundance has decreased only slightly. This demonstrates that the N/O ratio is very sensitive to the

presence of SNRs, and may go a long way toward explaining the large scatter observed in the N/O abundance ratios for GEHRs. Of course, just to make things interesting, the N^+/O^+ ratios for nuclei A and B are almost identical.

WR stars in GEHRs

There are two reasons to search for WR stars in GEHRs. The first is to investigate the possibility that WR stellar winds may be responsible for the anomalous kinematics of GEHRs. The second is to increase the data concerning the presence of massive stars in GEHRs.

The nearest GEHR, 30 Doradus in the LMC, has a very large population of WR stars (Feast, Thackeray and Wesselink 1960). When Smith and Weedman (1972) discovered the anomalous broad emission lines in 30 Doradus, they suggested that the stellar winds of the numerous WR stars might be responsible. Conti and Massey (1981) and D'Odorico and Rosa (1981) independently discovered several WR stars in NGC 604 in M33. Since Melnick (1979) had expanded the data of Smith and Weedman (1970), showing that all GEHRs produced anomalously broad lines, this lead Conti and Massey to speculate that WR stars may be present in all GEHRs. Recently, D'Odorico, Rosa, and Wampler (1983) have published a search for WR stars in the GEHRs of NGC 300 and M 101. They detected the presence of WR stars in 2 of 16 regions in NGC 300 and 2 of 6 in M 101. This work does not constitute a thorough search of these regions, as typically only one position,

covering only a fraction of the nebular surface, was observed in each case.

WR stars can be found with sensitive searches of the λ4650 - λ4700 (blue band) and λ5650 - λ5850 (red band) regions of the optical spectrum. The blue band can consist of emission from N III λ4634 - λ4642, N V λ4603 - λ4619, C III λ4650, C IV λ4658, and He II λ4686. The red band can consist of emission from C III λ5696 and C IV λ5802 - λ5812. WR stars are divided into N and C types showing primarily nitrogen and carbon emission respectively. A typical individual (galactic) WR star will have an equivalent width of 30 to 40 angstroms of emission in both the blue and red bands. In NGC 604, many positions show a blue and red band equivalent width of more than 10 - 20 Angstroms.

Figures 6.2, 6.3, 6.4, and 6.5 show plots of the IIDS spectrophotometry from λ4400 to λ4850 at different positions in NGC 5471, NGC 4214, NGC 2363, and NGC 2403 #1. The blue band of WR emission is detected in the spectra of NGC 4214N and NGC 2403 #1 A. The equivalent widths of the emission in the blue band have been measured and listed in table 6.3. The important point here is that WR emission is not detected at most of the positions observed.

This observation can be quantified and converted to an estimate of the upper limit of the ratio of WR stars to normal early-type stars in these GEHRs. The r.m.s. deviation in the continuum was

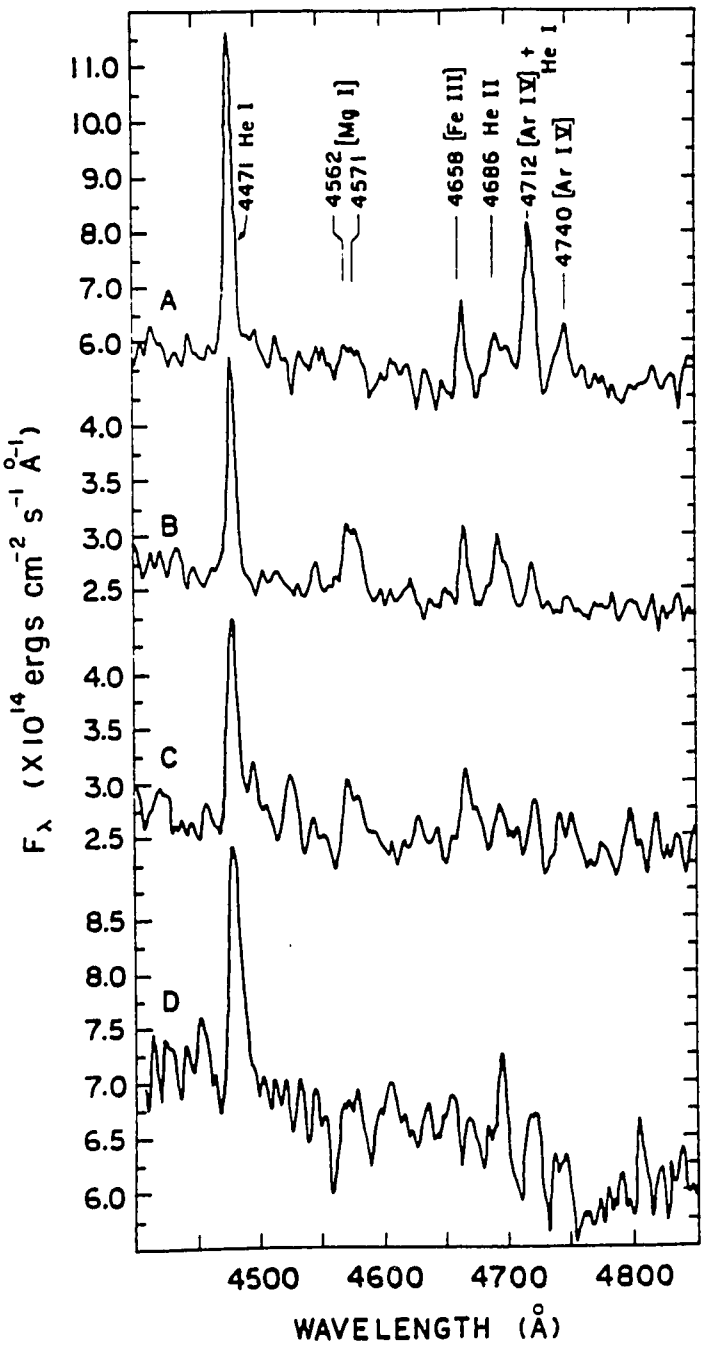

Figure 6.2 IIDS Spectra Near the WR Blue Band for NGC 5471

The IIDS spectra for four positions in NGC 5471 in the range of λ4400 to λ4850. The prominent emission lines and the respective elements are noted.

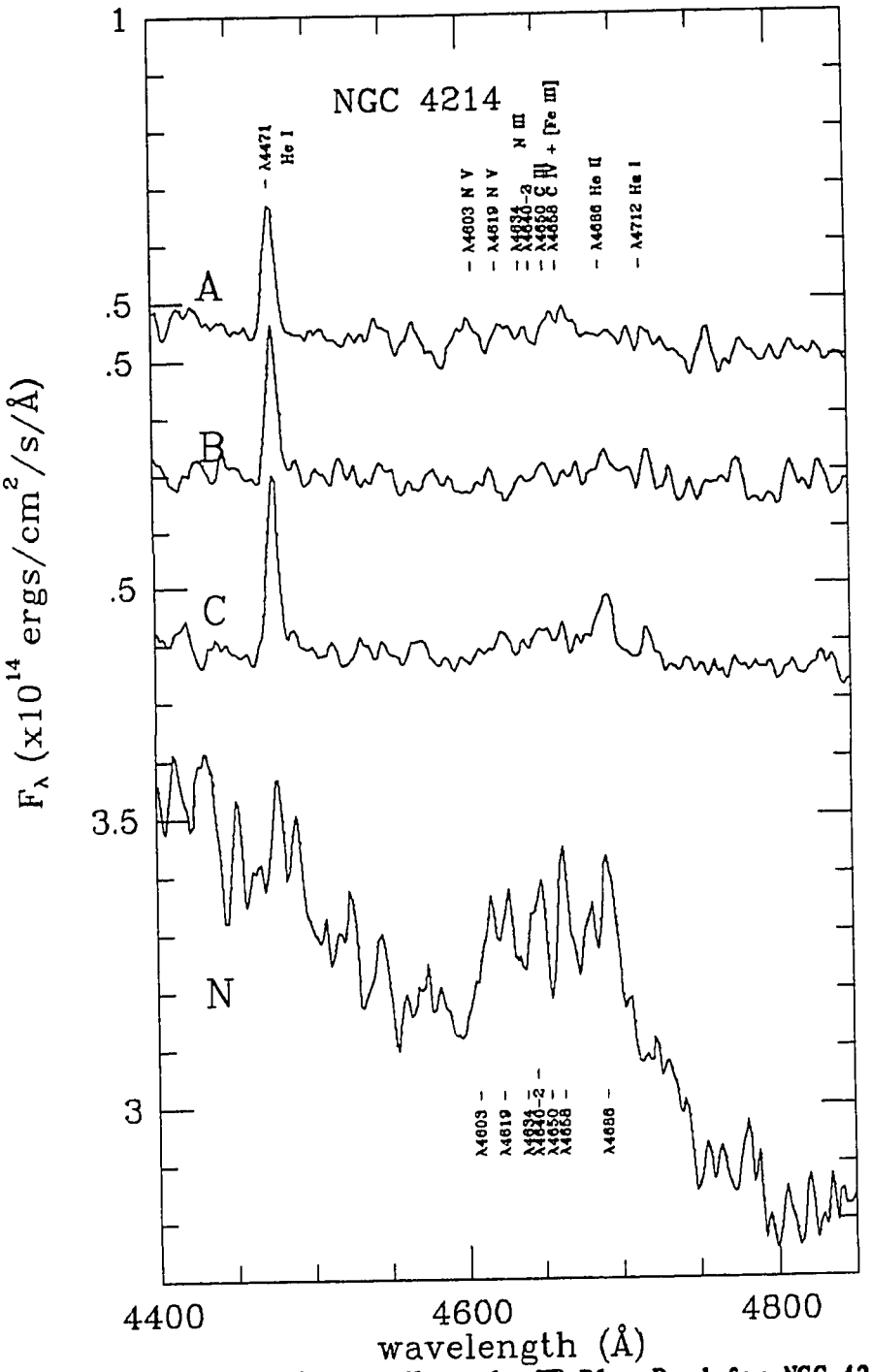

Figure 6.3 IIDS Spectra Near the WR Blue Band for NGC 4214

The IIDS spectra for four positions in NGC 4214 in the range of λ4400 to λ4850. The prominent emission lines and the respective elements are noted.

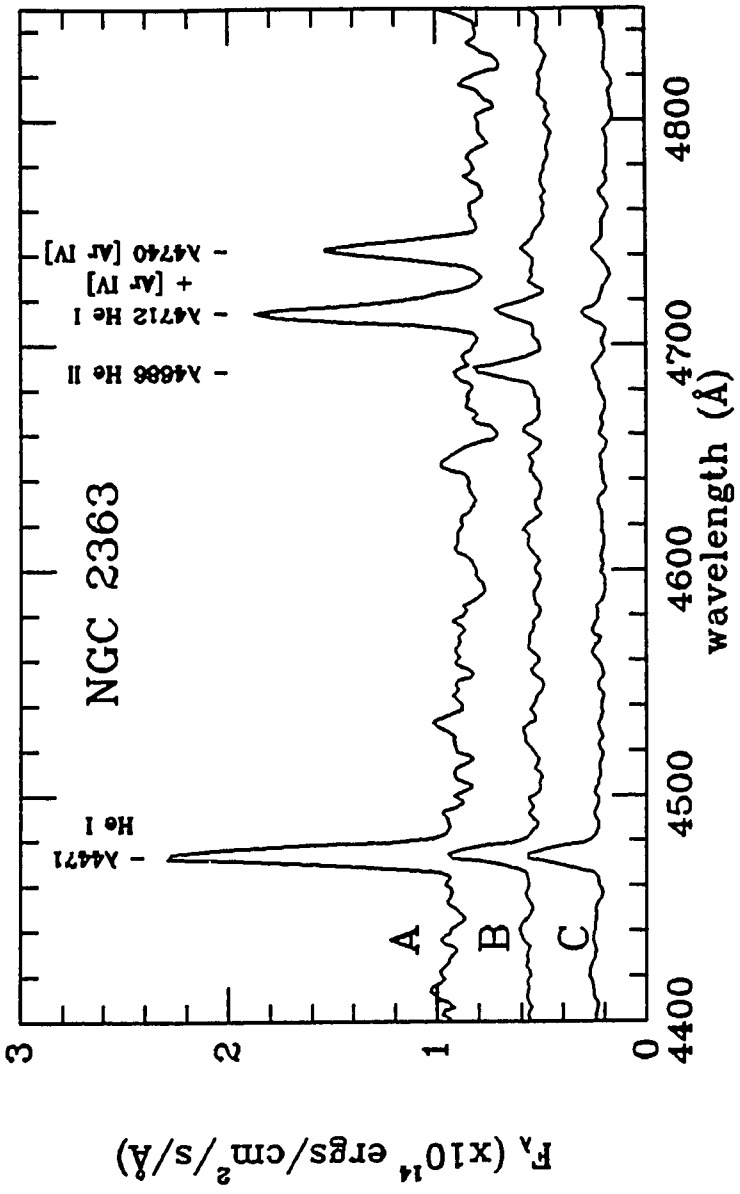

Figure 6.4 IIDS Spectra Near the WR Blue Band for NGC 2363

The IIDS spectra for three positions in NGC 2363 in the range of λ4400 to λ4850. The prominent emission lines and the respective elements are noted.

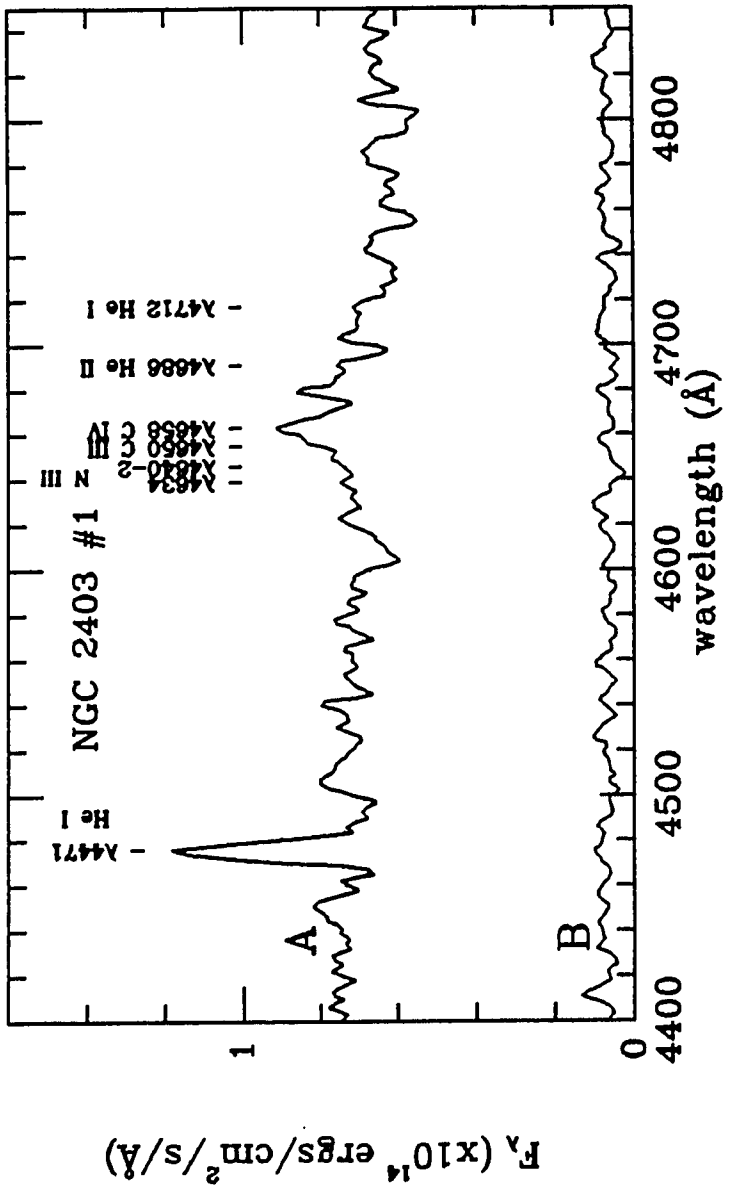

Figure 6.5 IIDS Spectra Near the WR Blue Band for NGC 2403 #1

The IIDS spectra for four positions in NGC 2403 #1 in the range of λ4400 to λ4850. The prominent emission lines and the respective elements are noted.

Table 6.3

WR Blue Band Strengths

position	r.m.s. % of continuum	EW (BB)	Observed w/ Echelle
NGC 5471 A	6	...	yes
B	4	2.3 (1.0) (λ4686)	no
C	10	...	no
D	9	1.0 (0.5) (λ4686)	no
NGC 4214 A	3	...	no
B	6	...	yes
C	5	1.5 (1.0) (λ4686)	no
N	3	6.0 (2.0)	no
NGC 2363 A	7	...	yes
B	6	2.2 (1.0) (λ4686)	yes
C	6	...	no
NGC 2403 1 A	6	6.0 (2.0)	yes
B	31	...	no

determined for each spectrum in the line free region between λ4490 and λ4540, and is also listed in table 6.3. A typical value for the r.m.s. deviation is about 6 percent of the continuum for most of the observations. Smoothing the spectra increases the sensitivity to broad features, but smoothing did not reveal any new evidence of broad emission in any of the regions where WR emission was not previously detected. From the r.m.s. deviations of the continuum a very conservative upper limit of 5 angstroms equivalent width can be set for the blue WR emission band at all positions. Following the method of D'Odorico and Rosa (1981), it is assumed that WR stars have blue luminosities comparable to main sequence and supergiant O, B, and A stars. Then, adopting an equivalent width of 50 angstroms as the typical value for the blue emission band of a WR star places an upper limit on the fraction of WR stars at 10 percent. Using this method, D'Odorico and Rosa found a fraction of WR stars of 50 percent for NGC 604.

The emission lines of all of these regions are known to be broad (FWHM > 50 km/s) from large aperture global studies (Smith and Weedman 1970, Melnick 1977). For several positions (also noted in table 6.3), high spatial resolution slit spectra also showed broad line widths (Skillman and Balick 1984). Since the supersonic flows produced by WR stars cannot outlive the stars, in order to account for the broad lines in these regions in terms of WR winds, the proposed WR stars in these regions must have a much higher efficiency

of imparted mechanical energy per luminosity than the WR stars in NGC 604.

The fact that the velocity dispersion in GEHRs scales with total luminosity despite a large range in fraction of luminosity contribution by WR stars argues against WR stars being the sole source of mechanical energy producing the anomalously large velocity dispersions observed. Note that this does not rule out stellar winds as a sole energy source. Abbott (1982) has shown that the total energy contribution of stellar winds from O stars can be comparable to that of WR stars when averaged over total stellar populations and lifetimes.

Conclusions

The observations reported here raise many more questions than they answer. Of course, the main question that drives all others is the source of the larger line widths. To date, our only clue has been the correlation of line width with total luminosity. In the Terlevich and Melnick (TM) picture of a GEHR, this has a natural explanation. Unfortunately, conducting a critical test of the TM model is not an easy task.

There is every reason to believe that supernovae and supernova remnants play an important role in determining the physical conditions in GEHRs. The observations here have uncovered at least one SNR in a GEHR and raised suspicion of the existence of several

others. The results of the optical spectrophotometry have shown that, given unlimited sensitivity, the λ6300 line of [O I] is the best optical discriminant of SNRs. A comparison of optical spectrophotometry with radio spectral index measurements has, for the first time, cast doubt on the ability of the [S II]/Hα ratio as an SNR detector. Two different tests have shown that, whereas SNRs may be difficult to detect, their presence can significantly alter the results of standard abundance analysis calculations.

It is now quite clear that WR stars are not omnipresent in GEHRs. This makes it unlikely that the stellar winds of WR stars can be soley responsible for the anomalous kinematics of GEHRs. This also places constraints on the suggestion of Massey and Hutchings (1983) that supermassive stars may be required for the development of GEHRs. Massey and Hutchings observed that the spectra of the most luminous stars in the GEHRs of M 33 resembled the spectrum of R 136, the most luminous star in 30 Doradus. This coincidence and the presence of WR spectral features in a large number of GEHRs led them to the proposition that, 'the presence and size, of giant H II regions in galaxies may be controlled by the properties of a few highly luminous and massive stars.' A point to be emphasized here is that these observations only constrain, and do not negate, the proposal of Massey and Hutchings. There is no reason to presume that very massive stars must have WR spectral types. While the stellar winds of normal WR stars are a factor of ten times more powerful than

comparable O stars, O stars are known to have strong stellar winds. Any extrapolation up to stars of 100+ solar masses must be regarded as speculative. Finally, it should be noted that the presence of supermassive stars will invalidate the calculations of the expected supernova rate per Hβ luminosity, since one supermassive star can produce the UV output of hundreds of lesser stars (BDD).

Chapter VII The Neutral Gas Environment of GEHRs

The massive stars that produce the ionizing radiation in GEHRs have lifetimes of order 10^7 years or less. Thus, GEHRs are astronomically 'young' objects. Since GEHRs are so young, the environment presently surrounding a GEHR must be comparable to the physical surroundings preceding the star formation event that resulted in a GEHR. Assuming that the GEHR has not had sufficient time to significantly alter its surroundings, studying the present local environment of a GEHR should provide clues leading to a better understanding of the early stages of evolution of a GEHR. As a check of this assumption, note that a sound speed of 10 km/s translates to a rate of transmission of hydrodynamical information of 10 pc per million years. Since typical dimensions of GEHRs range from 100 - 1000 pc, this implies that any hydrodynamical disturbances due to the massive stars (stellar winds, supernovae) will be confined to the GEHR, and will not have time to significantly alter the surroundings.

There are many important questions that can be answered through observations of the neutral gas environment surrounding the GEHR. Is the GEHR adjacent to or surrounded by the neutral gas from which it was born? This simple observation could place constraints on a model of the basic process that leads to the star formation event. Is there a minimum surface density of H I necessary for the formation of a GEHR and how does this compare with quoted limits for normal H II regions? Does the presence of an anomalously large H II region imply

the presence of an anomalously large H I cloud and vice versa? Answers to these questions will help determine whether GEHRs are born due to anomalous initial conditions or if GEHRs just represent one extreme of a normal distribution. What is the ratio of the mass of the neutral gas to the mass of the ionized gas? This ratio can be used to estimate the astration efficiency - a key parameter in modeling the evolution of a GEHR. Are the anomalous kinematics of GEHRs reflected in the kinematics of the surrounding neutral gas? It may be that observations of the neutral gas can help in understanding the origin of the broad emission line widths observed in GEHRs.

The Observations

VLA spectral line observations of NGC 5471, NGC 2363, NGC 4214, and NGC 3239 have been made at frequencies corresponding to the hyperfine transition of neutral hydrogen. The observing parameters are listed in table 7.1. At the time of the earlier observations, velocity channel separations of 5 or 20 km/s were available, with a practical limit of 15 separate velocity channels. Channel separations of 20 km/s for NGC 5471 and NGC 2363 and 5 km/s for NGC 4214 were chosen based on signal to noise considerations. Maps were constructed for each channel and then a continuum map constructed in the identical manner was subtracted from each channel map. Throughout this chapter, 'spectral line channel map' will refer to the continuum-free map. The problem of missing short spacings is always a concern for interferometric spectral line work, but

Table 7.1

VLA Spectral Line Observing Parameters

	NGC 5471	NGC 2363	NGC 4214	NGC 3239
VLA Configuration	B	B	C	C
Integration Time (hr)	5	5	8	8
Number of Antennae	25	25	25	25
Center Velocity (km/s)	280	100	295	765
Channel Width (km/s)	20	20	5	10
Number of Channels	15	15	15	31

fortunately all galaxies have been either previously mapped at a lower resolution (Viallefond, Allen, and Goss 1981 (VAG); Wevers 1984; Allsop 1979), or single dish measurements exist (Dickel and Rood 1978). Comparison of the results of the present study with the previous interferometric and single dish studies will reveal to what degree signal has been missed due to the effects of missing short interferometer spacings.

a.) NGC 5471

Figure 7.1 shows the λ21 cm continuum map and maps of the three spectral line channels in which signal was detected. The spectral line maps correspond to central velocities of 260, 280, and 300 km/s. The central velocity of 280 km/s corresponds to the central velocity for both λ21 cm H I and Hα measurements reported by VAG. All maps have been constructed with a strong taper resulting in a synthesized beam of 12" FWHM. The contour levels in the spectral line channel maps are set at 5 mJy/beam which translates to steps of 7.9×10^{20} atoms/cm^2 in surface density of neutral hydrogen. The cross in each spectral line channel map represents the position of the radio continuum peak. The ionized hydrogen appears to lie in a local minimum of H I between two large concentrations to the northeast and the southwest.

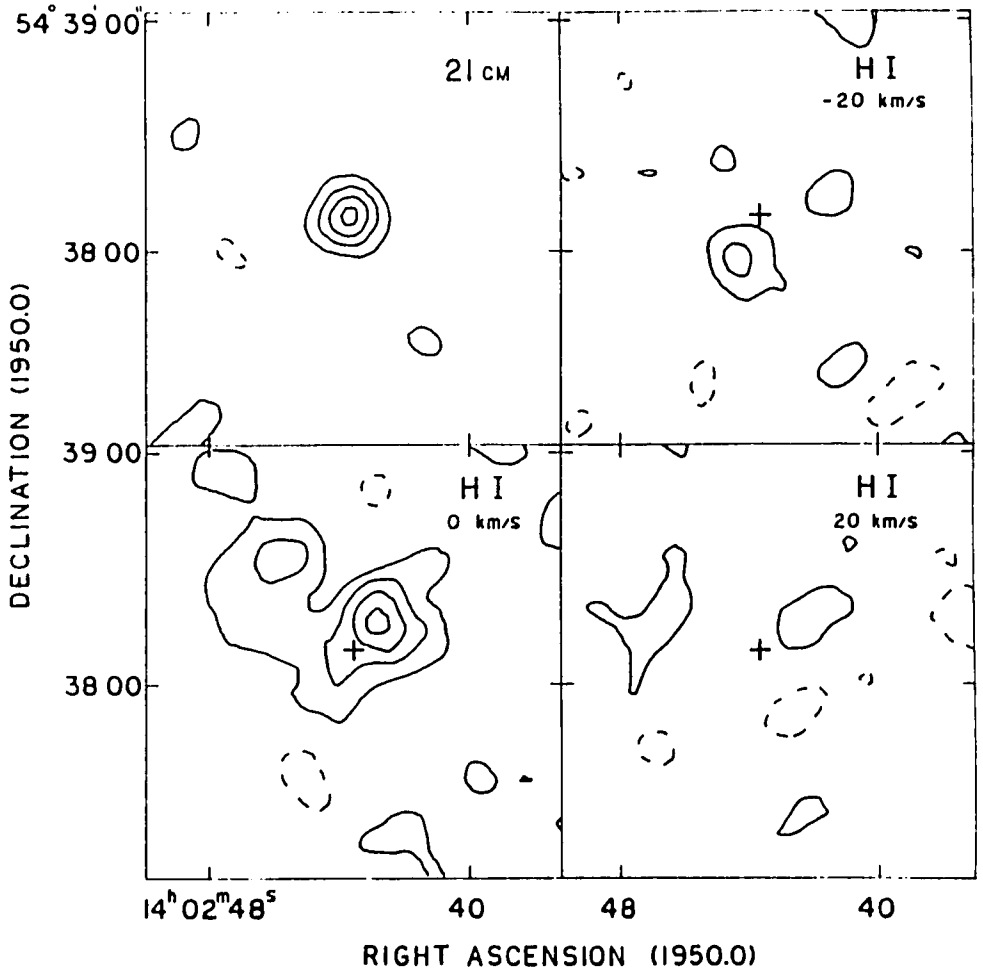

Figure 7.1 λ21 cm Spectral Line Maps for NGC 5471

The λ21cm radio continuum and H I spectral line maps for NGC 5471. These maps were constructed with a beamsize of 12 . The contour levels in the H I maps are set at 5 mJy/beam which corresponds to 7.9 x 10^{20} H I atoms/cm2. The cross marks the central position of the GEHR.

The total H I in the three spectral line maps represents 60 +/- 15 x 10^6 $M_\odot$ of neutral hydrogen, which compares quite favorably with the 86 +/- 14 x 10^6 $M_\odot$ reported by VAG. Since 70 percent of the H I was detected at this higher resolution, it can be concluded that most of the H I is concentrated in the clouds detected. There are three more physical parameters that can be derived from the data: the total H II mass and the H I and H II densities. Unfortunately all three parameters are dependent on modelling the gas distribution. Deriving the density of the HI is dependent on modelling the third dimension of the H I distribution. If the H I distribution is modelled as a cylinder with its axis of symmetry in the plane of the sky and projected dimensions of 45" x 20" (1570 pc x 700 pc), then the average density of H I is 4.0 +/- 2 atoms/cm^3.

The density and mass of the ionized hydrogen is extremely model dependent. The physical basis for this large dependency is the fact that thermal bremsstrahlung radiation is dependent on the square of the ionized gas density. Mezger and Henderson (1967) have used the bremsstrahlung emissivity formulation of Oster (1961) to produce formulae for calculating the density and total mass of ionized hydrogen. The necessary input parameters are a model geometry, the observed flux, the distance and a gas temperature. For GEHRs, the largest uncertainty comes from dividing the observed geometry into core and halo components. As an illustrative example, the data on NGC 5471 from Isreal, Goss, and Allen (1975) (IAG) will be examined

here. IAG calculate the density and mass of the ionized gas in NGC 5471 via two different models. In the first model, all of the radio continuum radiation is assumed to come from a cylinder of a diameter and depth equal to 255 pc. The second model consists of 3 cores (22% of the total flux, 100 pc diameters) and 1 envelope (33% of the flux, 650 pc diameter). The first model yields an electron density of 21 cm^{-3} and a total mass of 7 x 10^6 $M_\odot$. The second model gives a slightly higher density for the cores (32 cm^{-3}) and, of course, a lower density for the envelope (2.3 cm^{-3}). The mass estimates for the second model are 1.2 x 10^6 $M_\odot$ for each of the cores, and 24 x 10^6 $M_\odot$ for the envelope. Thus, the mass estimate of the ionized gas increased by a factor of 4 when a more detailed model was employed. The most frustrating aspect of the situation is that most of the estimated mass is in the envelope. Given the relatively low radio continuum surface brightness of the envelope, estimates of the total flux and size of the envelope are quite vulnerable to error. Note also the dependency on the assumption of uniform density. If the ionized gas is clumpy, then the total mass estimates represent only upper limits.

Cognizant of the problems inherent in estimating the H II mass and density, calculations following the method of IGA have been performed, and the results are presented in table 7.2. The first row, labeled total, represents calculations for a single homogeneous cylinder model. The flux measurement is from table 3.7, the

temperature comes from the optical spectroscopy, and the size chosen comes from the radio map. Next the region is divided into nuclei and a halo with the flux in the halo derived from the difference between the total region flux and the sum of the nuclear fluxes. The mass from the single component model reported here is larger than that calculated by IGA because the model size is larger. If the region size is chosen to be 10" instead of 15", the density doubles and the total mass estimate halves. All other estimates of mass and density are within factors of two of those reported by IGA. Given the results of table 7.2, a reasonable value of the mass of the ionized gas in NGC 5471 is 20 +/- 10 x 10^6 $M_\odot$.

For completeness, the distribution of neutral hydrogen in the parent galaxy of NGC 5471, M 101, will be reviewed here. The relationship between H I concentrations and H II complexes in M 101 has been studied by VAG. The conclusions of their study which are most relevant to this discussion are:

> 1.) The brightest concentrations of H I are found near optically prominent giant H II complexes. These H I complexes are large (sizes up to 2 kpc, H I masses of 20 - 90 x 10^6 $M_\odot$) and of relatively low mean H I density (1 - 6 cm^{-3}).
>
> 2.) Similarly massive H I concentrations are occasionally associated with faint H II regions in the outer parts of the galaxy.
>
> 4.) The associations can be grouped roughly into three morphological classes: objects for which the H II complex is coincident (C) with the maximum H I column density; objects for which the the H II complex is at the edge (E) of the H I concentration; and objects for which the H II complex is between (B) two H I concentrations.

Table 7.2

H II Mass and Density Estimates

	Te	S_ν(5 GHz) (mJy)	D (Mpc)	size (arc sec)	Ne (cm^{-3})	M ($x10^6$)
NGC 5471						
Total	12,500	9.2	7.2	15	5.5	27
A	12,500	3.7	7.2	2	73	0.82
B	12,500	2.5	7.2	2	60	0.67
C	12,500	1.4	7.2	2	45	0.50
Halo	12,500	1.6	7.2	20	1.5	17
NGC 2363						
Total	14,500	9.8	3.25	10	16	2.1
A	14,500	5.1	3.25	2	130	0.14
B	14,500	1.5	3.25	2	71	0.07
C	14,500	1.6	3.25	2	74	0.07
Halo	14,500	1.6	3.25	20	2.3	2.4
NGC 4214						
Total	10,000	4.0	7.0	10	6.5	8.6
A	10,000	0.5	7.0	2	26	0.27
B	10,000	1.8	7.0	2	50	0.51
C	10,000	1.5	7.0	2	46	0.47
Halo	10,000	0.2	7.0	14	0.9	3.2
NGC 3239						
Total	12,000	33.9	15.2	40	1.7	1510
A	12,000	19.0	15.2	10	9.9	140
B	12,000	7.0	15.2	6	13.0	40
Halo	12,000	7.9	15.2	60	.4	1340

> In general for the B and E objects there is a rough agreement between the amount of 'missing' H I and the mass of the H II present.

VAG classify NGC 5471 as a C type H II complex, and note that this means that the 'region of ionization is too small to significantly deplete the neutral gas.' The higher resolution observations reported here show that NGC 5471 might better be classified as a B type H II complex.

b.) NGC 2363

Figure 7.2 shows 7 spectral line channel maps of NGC 2366 constructed with a synthesized beam size of 18.6" FWHM. The channel maps are separated by 20 km/s in velocity. The contour levels are set at intervals of 8 mJy/beam which corresponds to 5.3×10^{20} atoms/cm^{-2} of neutral hydrogen. The position and size of the cross in each map corresponds to the position and approximate size (15") of NGC 2363. The GEHR is adjacent to a large neutral gas cloud which shows significant signal in two channels. Figure 7.3 shows four spectral line channel maps made with a beamsize of 12.2". The higher resolution shows that the GEHR is indeed more adjacent to than coincident with the large H I concentration.

Figure 7.4 is a map of the total H I content of NGC 2366 which has been constructed with the MOMNT program of the NRAO AIPS image processing system. MOMNT makes weighted sums over a number of spectral line channel maps and can simultaneously smooth the images

Figure 7.2 λ21 cm Spectral Line Maps for NGC 2366

The λ21cm radio continuum and H I spectral line maps for NGC 2366. These maps were constructed with a beamsize of 18.6 FWHM. The contour levels in the H I maps are set at 8 mJy/beam which corresponds to 5.3 x 10^{20} H I atoms/cm2. The cross marks the position of NGC 2363.

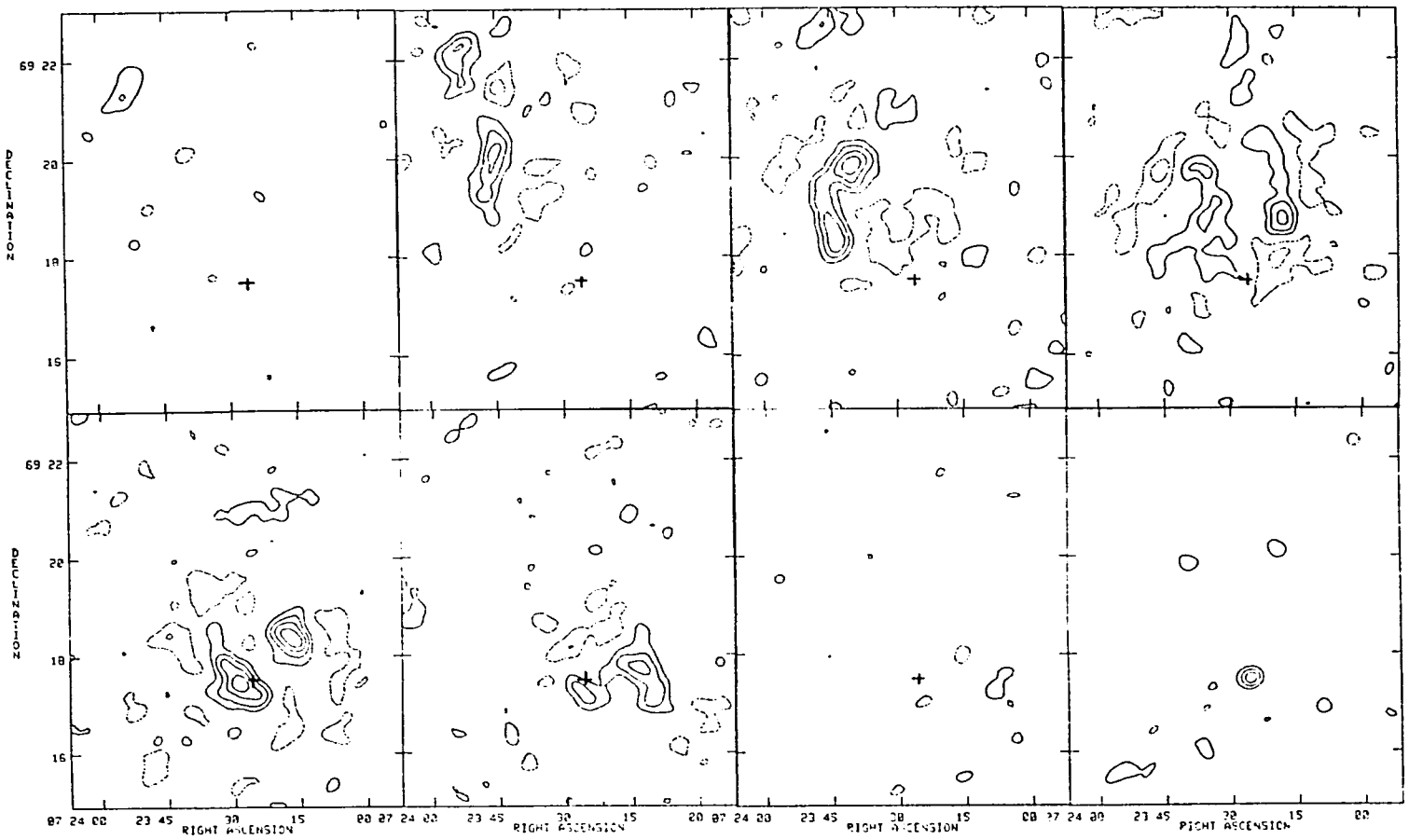
69 22
20
18
16
DECLINATION
07 24 00
23 45
30
15
08 07 24 00
RIGHT ASCENSION

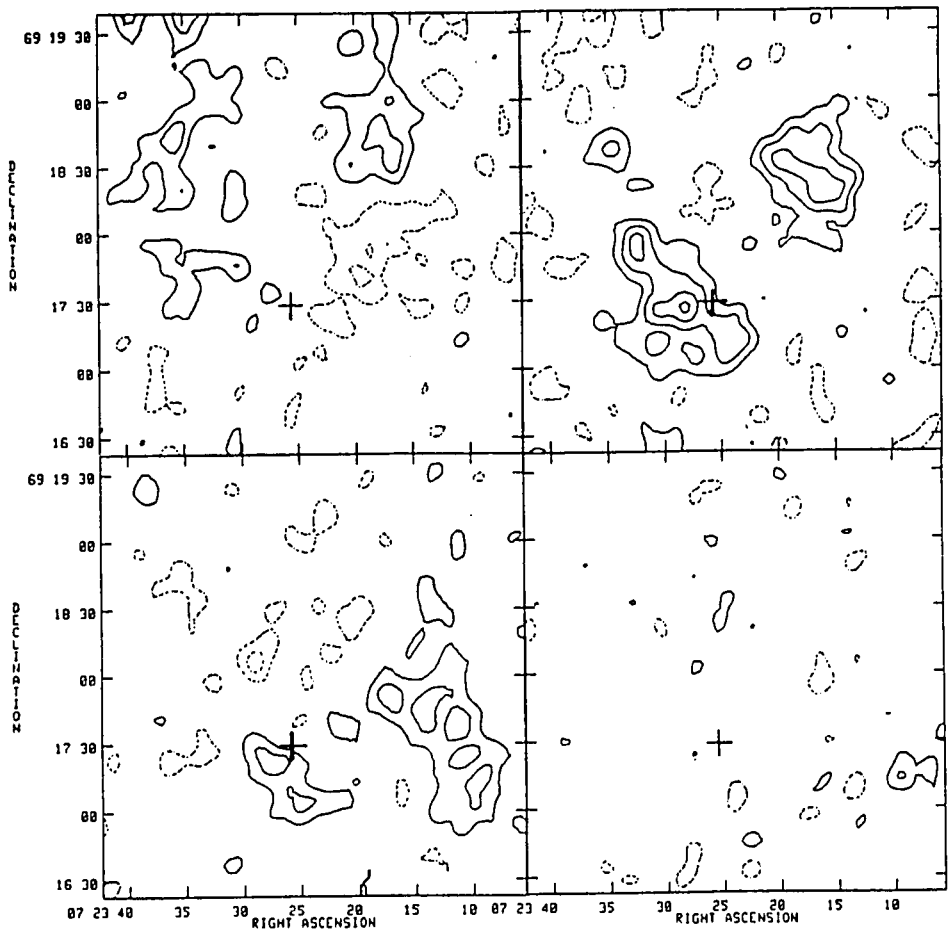

Figure 7.3 λ21 cm Spectral line Maps for NGC 2363

High resolution H I spectral line maps in the vicinity of NGC 2363. These maps were constructed with a beamsize of 12.2". The contour levels are set at 4mJy/beam.

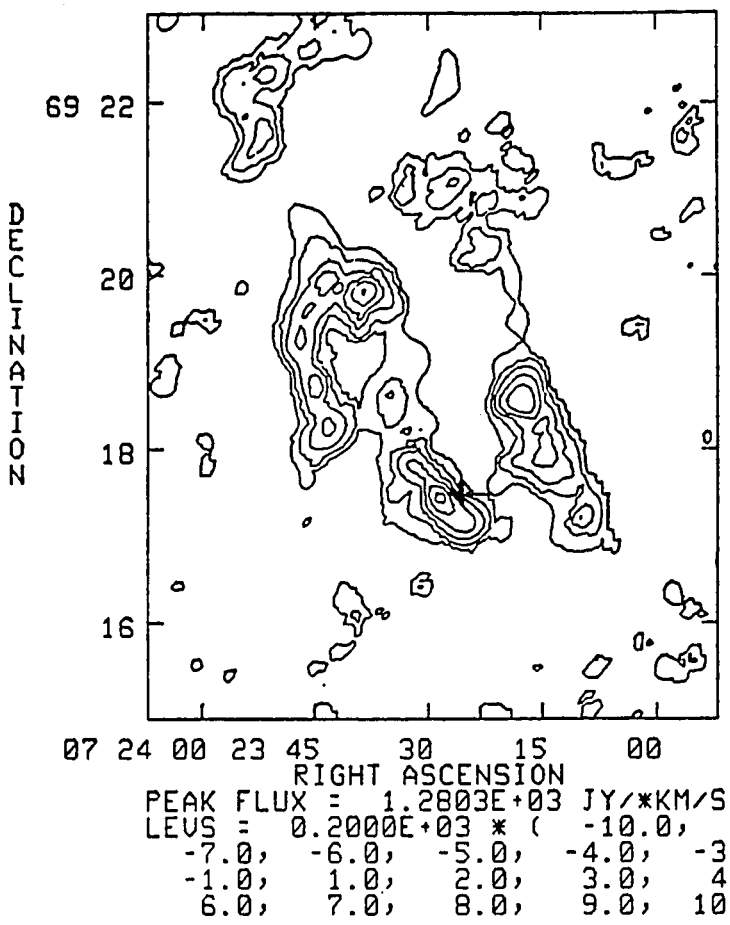

Figure 7.4 Total H I Map for NGC 2366

The sum of the total H I from the maps in figure 7.2. The cross marks the position of the GEHR NGC 2363.

in both the spatial and velocity dimensions. After smoothing is applied, but before the signal is summed, a cutoff is applied such that only signal above the cutoff is included in the calculation. In this way, negative sidelobe structure, which would otherwise erase significant signal, can be excised. Figure 7.4 was constructed from the series of spectral line channel maps shown in figure 7.2. The data were smoothed in the spatial regime with a two dimensional Gaussian of 10" FWHM, but no smoothing was applied in the velocity dimension. A cutoff of 3 mJy/pixel/channel was used here. Several MOMNT calculations were made with this data base, and the results were quite consistent within a reasonable range in the choice of smoothing functions and cutoff. The total integrated signal in figure 7.3 is 104 Jy*km/s. This can be compared with the single dish measurement of 195 Jy*km/s (Dickel and Rood 1978) or 203 Jy*km/s (Wevers 1984), and means that, despite the lack of shorter spacings, the VLA was sensitive to at least half of the total H I in NGC 2366.

The total mass of H I in the concentration next to NGC 2363 was measured to be 3.1 x 10^6 $M_\odot$. This measurement was made by summing over an area of 40" x 28" (630 x 450pc), which, using a cylindrical model, would represent an average density of 1 +/- 0.5 H I atoms/cm^3. Calculations of the H II mass and densities for NGC 2363, similar to those carried out for NGC 5471, are listed in table 7.2. 2 +/- 0.5 x 10^6 $M_\odot$ is a reasonable estimate of the mass of ionized gas, and the gas density estimates are comparable to those for NGC 5471.

It can be seen from figure 7.4 that the H I cloud adjacent to NGC 2363 is not the only strong concentration of HI in NGC 2366. A comparison of this H I map with an Hα photograph (Hodge and Kennicutt 1983) shows H II regions associated with the other H I concentrations, however, nowhere else in NGC 2366 is there an H II region approaching the dimensions and luminosity of NGC 2363. This is pointed out by Hodge (1983) in a study of the size distribution of H II regions in Irregular galaxies.

c.) NGC 4214

Figure 7.5 shows the 15 spectral line channel maps and a total H I map for the galaxy NGC 4214. These maps were constructed with a synthesized beam size of 24.5". Note the size scale of the maps in figure 7.5 to compare with figure 7.6. The pandemonium labeled figure 7.6 is a montage of high resolution maps of the same 15 spectral line channels and the corresponding continuum map for the central part of the galaxy. The maps in figure 7.6 have been constructed with a synthesized beam size of 13.2" FWHM. The channels are separated by 5.1 km/s and span the range from 259 km/s to 331 km/s. The contour levels are set at intervals of 5 mJy/beam which correspond to intervals in surface density of 1.6×10^{20} H I atoms/cm^2. The positions of the two crosses represent the continuum emission peaks. The southern cross corresponds to the position of

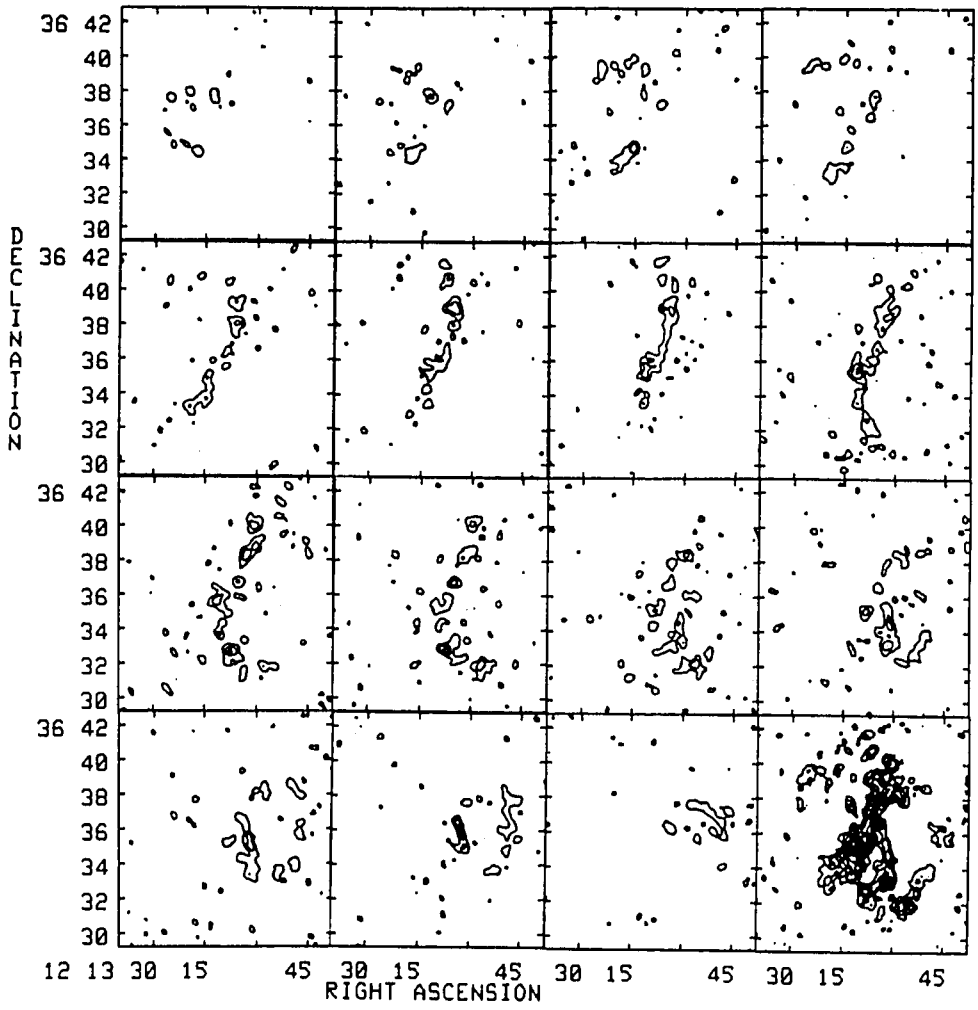

Figure 7.5 λ21 cm Spectral Line Maps for NGC 4214

Fifteen H I spectral line maps and a total H I map for the galaxy NGC 4214. The maps were constructed with a beamsize of 25". The contour levels in the spectral line maps are set at intervals of 12 mJy/beam.

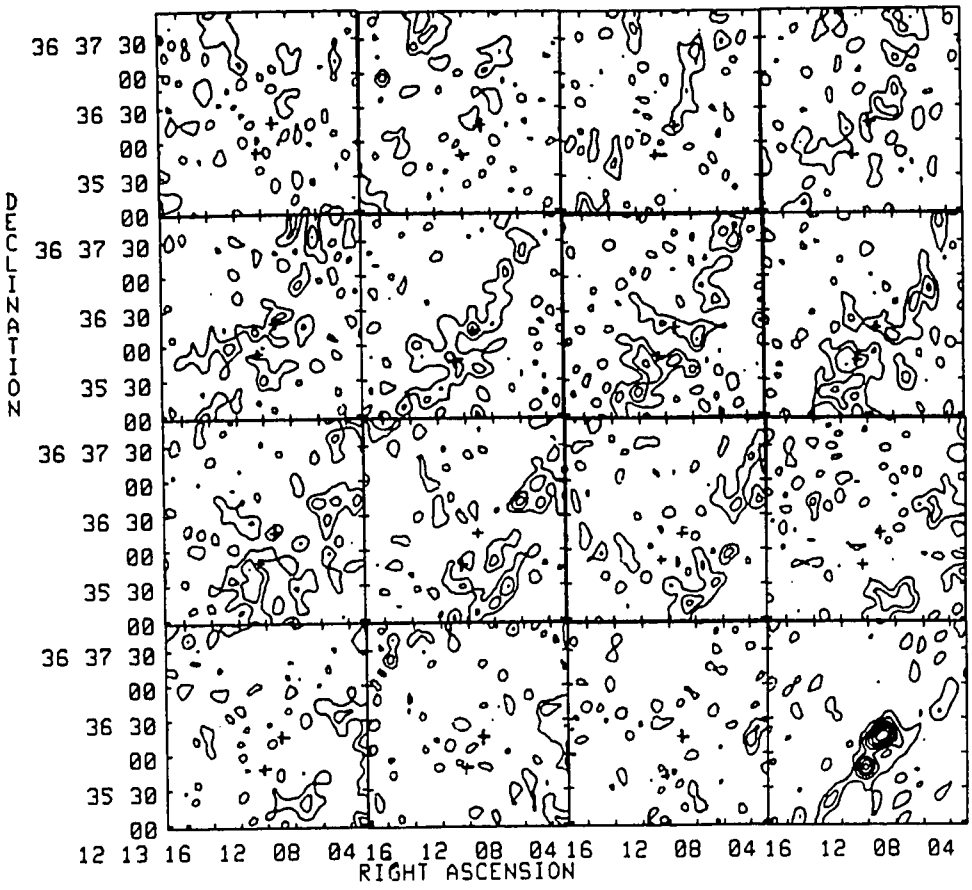

Figure 7.6 λ21 cm Spectral Line Maps for the Center of NGC 4214

Fifteen high resolution H I spectral line channel maps in the center of NGC 4214. The maps were constructed with a synthesized beam width of 13.2". A λ21 cm continuum map made at the same resolution is shown in the lower right corner. The two crosses correspond to the GEHRs NGC 42142 #1 and NGC 4214 N.

NGC 4214 #1 and the northern cross represents NGC 4214 N.

Figure 7.7 shows the result of a MOMNT calculation for the data shown in figure 7.6. The channel maps were Hanning smoothed in velocity and smoothed in the spatial dimensions with a two dimensional Gaussian of 8" FWHM. A cutoff of 4 mJy/pixel/channel was used. Note that the two continuum peaks are adjacent to H I concentrations. Six H I concentrations have been identified in figure 7.7 with numbers. All six H I concentrations fall in the range of 4 to 8 x 10^6 $M_\odot$ of neutral hydrogen. Concentration 1, next to NGC 4214 #1, consists of 5 +/- 2 x 10^6 $M_\odot$ of neutral hydrogen. With approximate dimensions of 25" x 22" (660 x 760pc), a cylindrical model of the H I in concentration 1 leads to an estimate of the average density of .8 +/- .4 H I atoms/cm^3. A measurement of the H I for the entire galaxy gave a value of 1.4 x 10^9 $M_\odot$. This is 60 percent of the total H I reported by Allsop (1979). Because of the nature of the cutoff used in the MOMNT calculations, this means that these measurements are sensitive to most of the neutral hydrogen in NGC 4214. The calculations of H II mass listed in table 7.2 indicate that a credible mass for the ionized gas in NGC 4214 #1 is 4 +/- 2 x 10^6 $M_\odot$. The H II densities are comparable with those for NGC 5471 and NGC 2363.

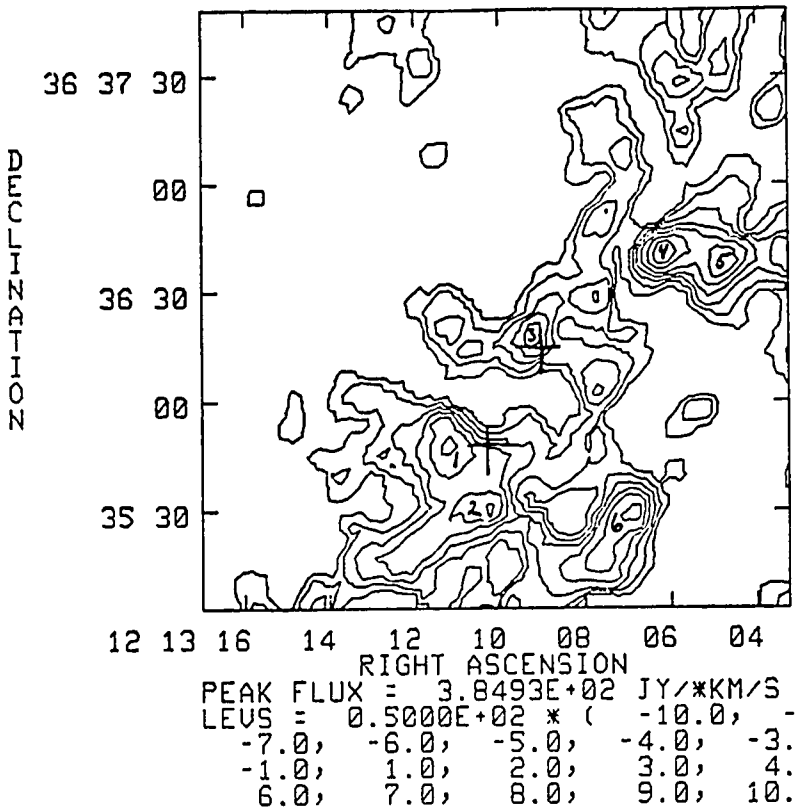

Figure 7.7 Total H I Map for the Center of NGC 4214

The total H I in the vicinity of the GEHRs in NGC 4214. Six H I concentrations are labeled.

The higher velocity resolution of the NGC 4214 observations allows an investigation of the velocity dispersion in the neutral gas. Figure 7.8 presents H I spectra for each of the six positions identified in figure 7.7. The points represent averages over a projected beamwidth of 450 pc FWHM. The velocity width for all of the profiles is between 25 and 35 km/s. This compares to an instrumental velocity resolution of 6.1 km/s (1.2 x the 5.1 km/s channel separation). Neutral gas at the expected temperature of 70 K (Dyson and Williams 1980) would have a thermally broadened profile of 1.8 km/s FWHM. Obviously there are large non-thermal motions in the neutral gas of NGC 4214.

Three possible explanations could account for the relatively broad H I profile widths. The first is the possibility that the rotation of the galaxy is responsible for the large line widths. If the synthesized beam width is large in comparison with the changes in the velocity field, broad line profiles will be the result. The second possibility is that processes associated with recent star formation (stellar winds, supernovae) could be 'stirring up' the gas. This second possibility is discounted by comparing the H I map to an Hα map of NGC 4214 (Hodge and Kennicutt 1983). There is evidence of recent star formation only adjacent to the H I clouds 1 and 3, but all 6 H I concentrations show relatively broad lines. Finally, the broad lines may be associated with the large gravitational forces represented by the H I concentrations. The broad lines may be

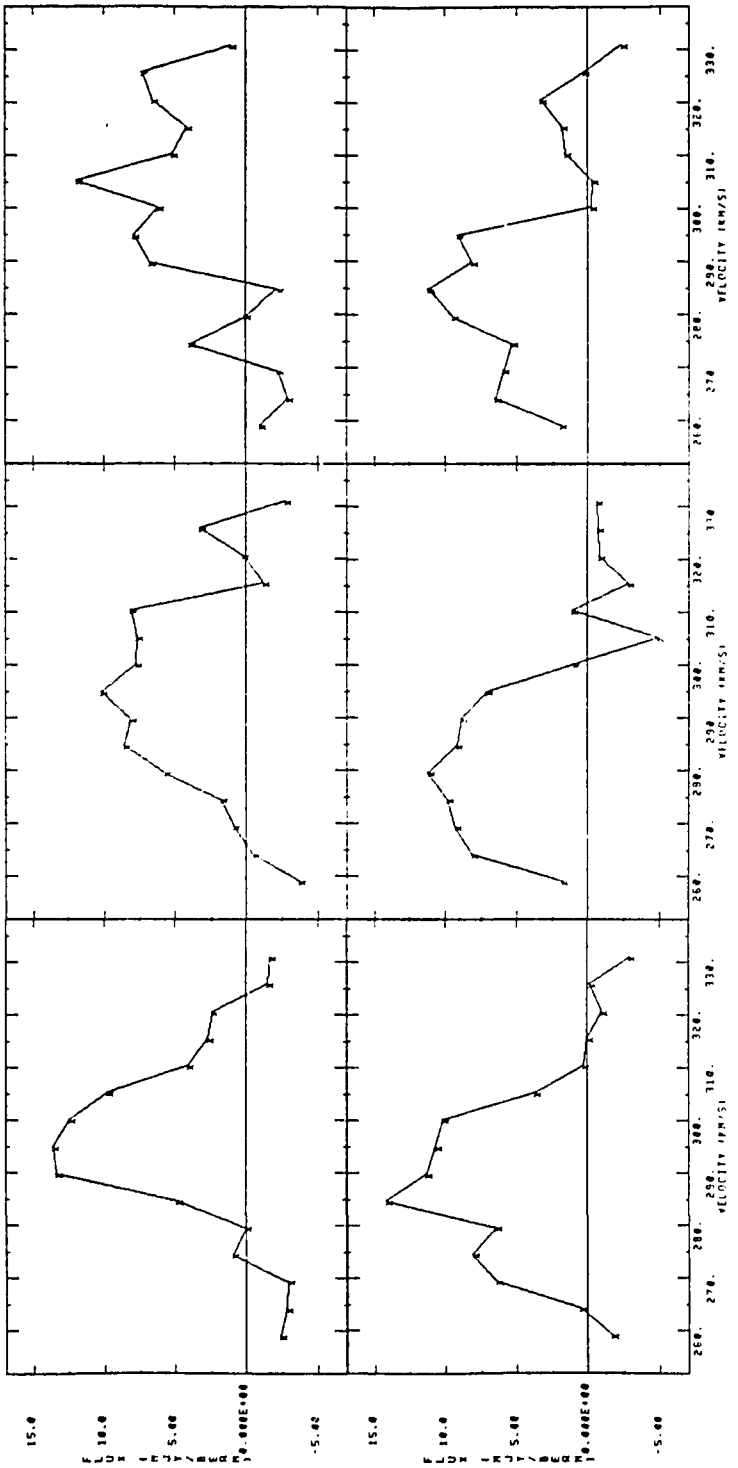

Figure 7.8 H I Spectra for 6 Positions in NGC 4214

The H I spectra for the six H I concentrations identified in figure 7.7. These spectra are constructed from the maps in figure 7.6. No velocity smoothing has been applied.

representative of the motions of cloud collapse or virialized motions of H I cloudlets in the large gravitational potential of the H I concentration.

In order to investigate possibilities 1 and 3, another MOMNT calculation was performed on the 13.2" resolution maps. Figures 7.9 a, b, and c show the results of this calculation. A grayscale plus contours representation has been chosen here to help make sense of broken contour lines. Map 7.9 a shows the total H I. A liberal cutoff of 3 mJy/beam/pixel was used, so this map shows more total H I than figure 7.7. Map 7.9 b shows the velocity field in the central region of NGC 4214. The contours are set at 10 km/s intervals, and the grayscale shows the sense of rotation of the galaxy. The important point to notice is that at several of the positions of the H I concentrations, the gradient in the velocity field is quite small. Several of these positions would be consistent with a total velocity field change of less than 5 km/s across the area of integration. Map 7.9 c shows the second moment calculation. The second moment is related to the velocity dispersion in the gas. For a Gaussian distribution, the second moment is equal to the dispersion, or 0.425 times the FWHM. Comparing maps 7.9 a and 7.9 c, it is clear that in several places, the positions of highest velocity dispersion correspond to positions of the largest H I concentrations. This is strong evidence in favor of the broad H I line profiles being attributable to gravitational forces.

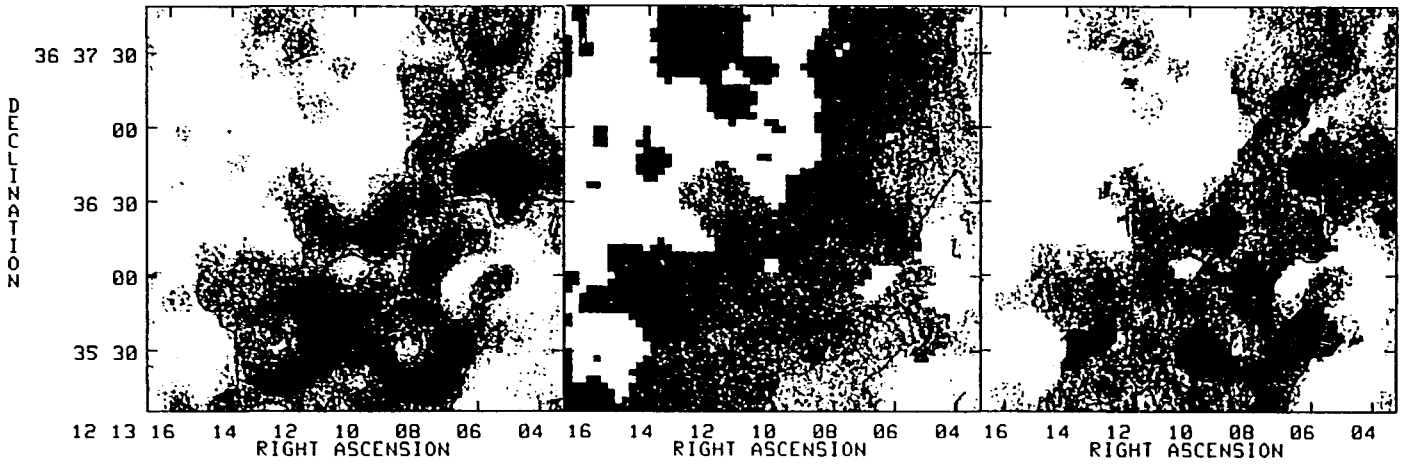

Figure 7.9 Zero, First and Second Moment Maps for NGC 4214

Maps of the total H I, the velocity field, and the velocity dispersion of the H I in the center of NGC 4214. Darker colors in the grayscale correspond to larger numbers in all three maps. In the second map, contours are set at 10 km/s intervals. In the third map, contours are set at 5, 10, 15 and 20 km/s.

In order to further study the velocity distribution of the gas in NGC 4214, a histogram plot of the individual pixel values in the second moment map was made (figure 7.10). Since the graph is in units of dispersion, the instrumental velocity resolution corresponds to 2.6 km/s. The mode of the distribution is 6 km/s. If the widths are thought of as the square root of the sum of the squares of the instrumental resolution, the thermal doppler width of the gas, and and an excess turbulent velocity, then the mode corresponds to an excess turbulent velocity of 5.4 km/s. This is a reasonable value for the effect of integrating over the galaxy's velocity field. However, there are a significant number of points above 10 km/s. This corresponds to an excess turbulent velocity of 9.6 km/s. A comparison of the spatial resolution of the spectral observations (13.2) and the range in velocity field gradient (0.2 to 1 km/s/arcsec) indicates that broadening due to rotation should correspond to a dispersion of 1 to 3.6 km/s. It would appear unlikely that spatial resolution effects could account for the large excess turbulent velocities. Nonetheless, it remains that the coincidence of broad H I line profiles with relatively small velocity gradients is the strongest evidence in favor of gravitationally induced broad H I line profiles in NGC 4214.

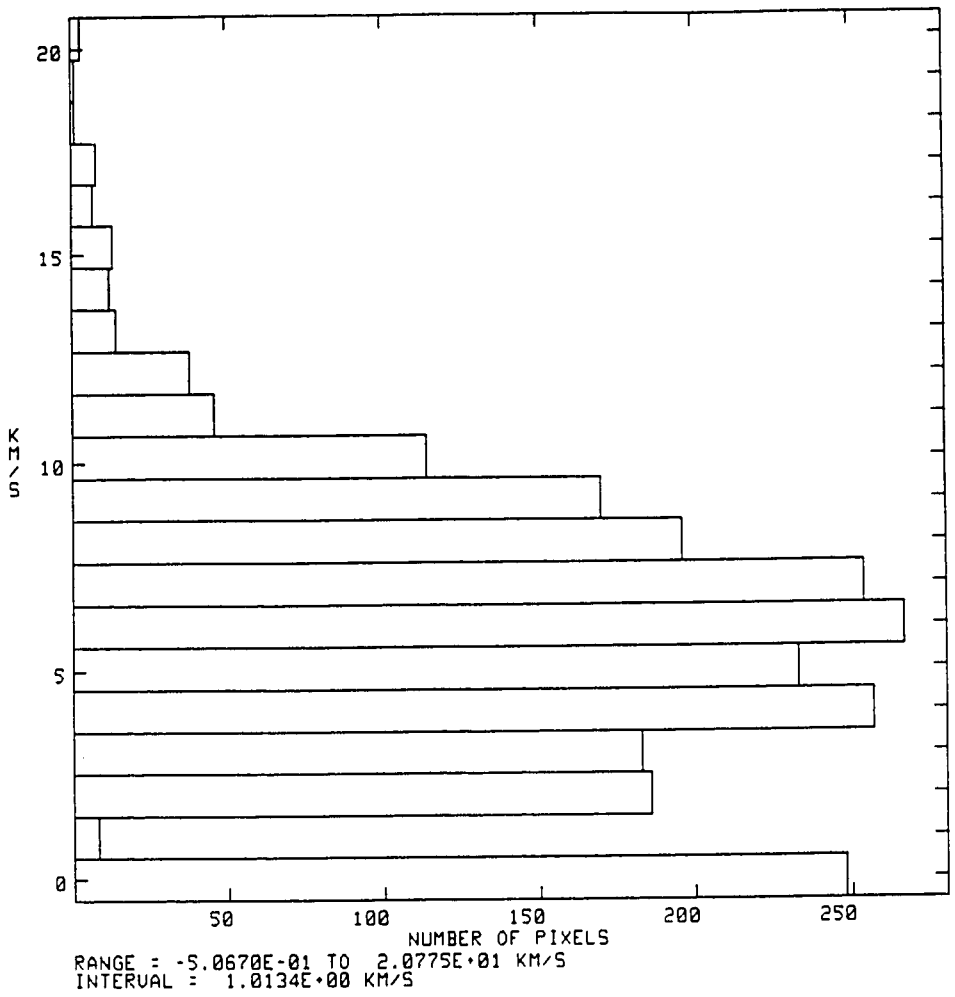

Figure 7.10 Histogram of Velocity Dispersion Values for NGC 4214

A histogram of the velocity dispersion at every pixel represented in the map of figure 7.9. The data have been binned at 1 km/s intervals.

d.) NGC 3239

NGC 3239 is an irregular galaxy with a GEHR (Hodge 1983). This galaxy was mapped at the VLA as a part of a separate study (Skillman and Hodge in preparation). Figures 7.11 a and b show the radio continuum map and the total H I map in the vicinity of the GEHR. The maps were constructed with a beam width of 14.1" FWHM. In map 7.11 b the contour levels correspond to intervals of 4.2 x 10^20 HI atoms/cm^2. As before, the crosses mark the positions of the continuum peaks. Both continuum peaks are adjacent to large H I concentrations. Both H I clouds contain about 1.3 x 10^8 $M_\odot$ of H I with a total mass in the region of 4 x 10^8 $M_\odot$. Cylindrical models yield average H I densities of .7 atoms/cm^3 for both clouds. The H II masses derived in the standard way, are listed in table 7.2. The H II mass and density estimates may be strongly affected by resolution effects. An overestimate in size results in an overestimate of the total H II mass.

Figures 7.12 a, b, and c show the results of MOMNT calculations for the entire galaxy. The GEHR is associated with the most massive H I concentrations in the galaxy, but there are many other large H I concentrations. The total H I in the maps is equal to 33 Jy*km/s which is about half of the single dish measurement of 73.4 Jy*km/s reported by Dickel and Rood (1978). Considering the conservative value of the cutoff used in the MOMNT calculation and the fact that the total signal in a set of maps made with a stronger taper gave a

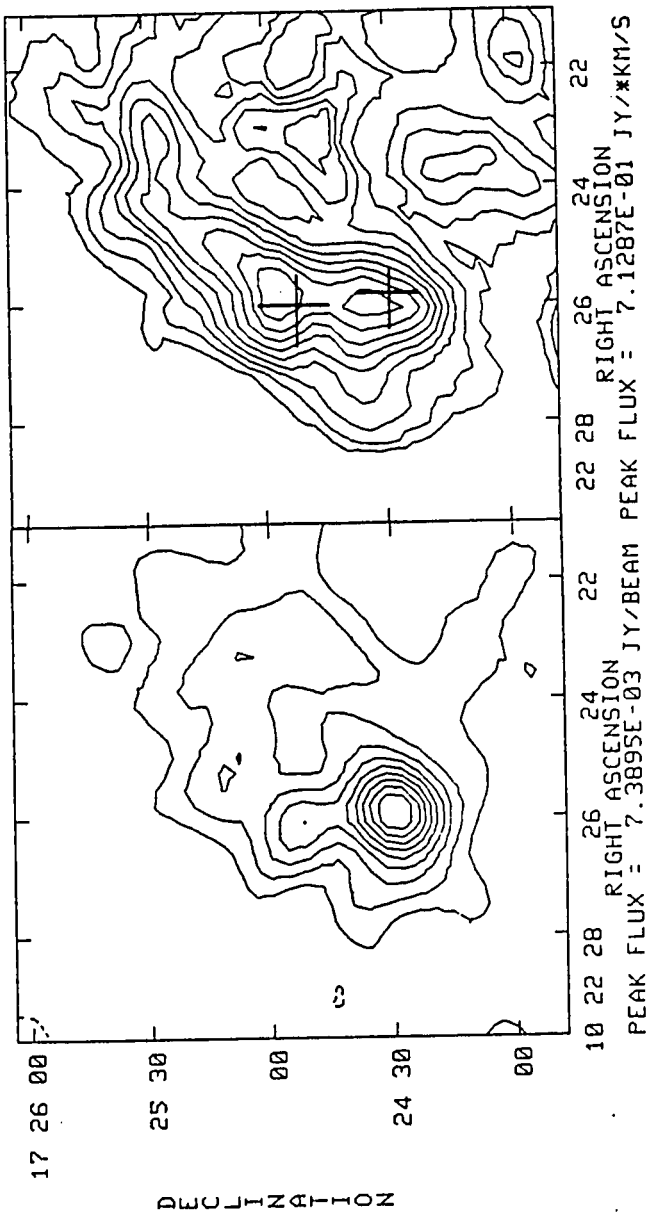

Figure 7.11 H II and H I Maps for the GEHR in NGC 3239

The λ21 cm radio continuum and total H I maps in the vicinity of the GEHRs in NGC 3239. The contour levels in both maps are set at intervals of 10% of the peak value in the map. The maps were constructed with a beamsize of 14.2" FWHM. The crosses in the H I map mark the positions of the radio continuum maxima.

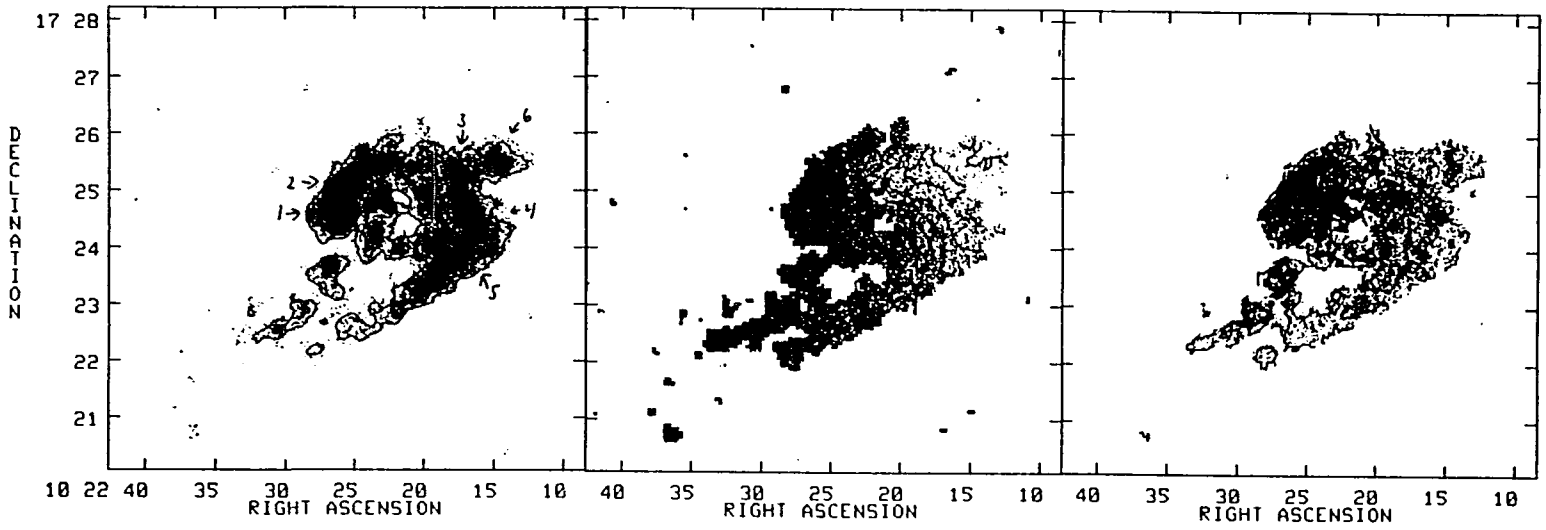

Figure 7.12 Zero, First and Second Moment Maps for NGC 3239

The total H I, the velocity field, and the velocity dispersion of the H I in the galaxy NGC 3239. Six H I concentrations have been identified in the total H I map. The contour levels in the velocity field map are set at intervals of 15 km/s. The contour levels in the velocity dispersion map are set at intervals of 5 km/s.

value 15 percent higher than that of Dickel and Rood, it is probable that these measurements are sensitive to most of the H I in NGC 3239. Comparison of the total H I map with an Hα photograph (Hodge and Kennicutt 1983) shows star formation associated with most of the H I concentrations. The velocity field is systematic, showing primarily solid body rotation with a warp. The velocity dispersion is largest in the vicinity of the GEHR, and, in general, is greatest near the strong H I concentrations. Figure 7.13 is a histogram plot of the points in the second moment map. For reference, the instrumental resolution is 10 km/s corresponding to a dispersion of 4.25 km/s. Like in NGC 4214, the velocity dispersion of the neutral gas in NGC 3239 is often much larger than consistent with the instrumental profile.

To get a better idea of the H I velocity dispersion, spectra were constructed for the 6 H I concentrations labeled in the total hydrogen map. These spectra are shown in figure 7.14. The broadest H I profiles are in the vicinity of the GEHR, although there are other broad profiles. Table 7.3 lists the results of fitting Gaussian profiles to the observed H I spectra. The most striking case is at position number 2 where the H I profile is at least 60 km/s wide. With a beam width of 13.6" FWHM and a velocity gradient of 1 - 2 km/s/arcsec, the expected broadening of the profiles due to the rotation of the galaxy should be of the order of 20 km/s or less. From the H I spectra, it can be stated conclusively that the large

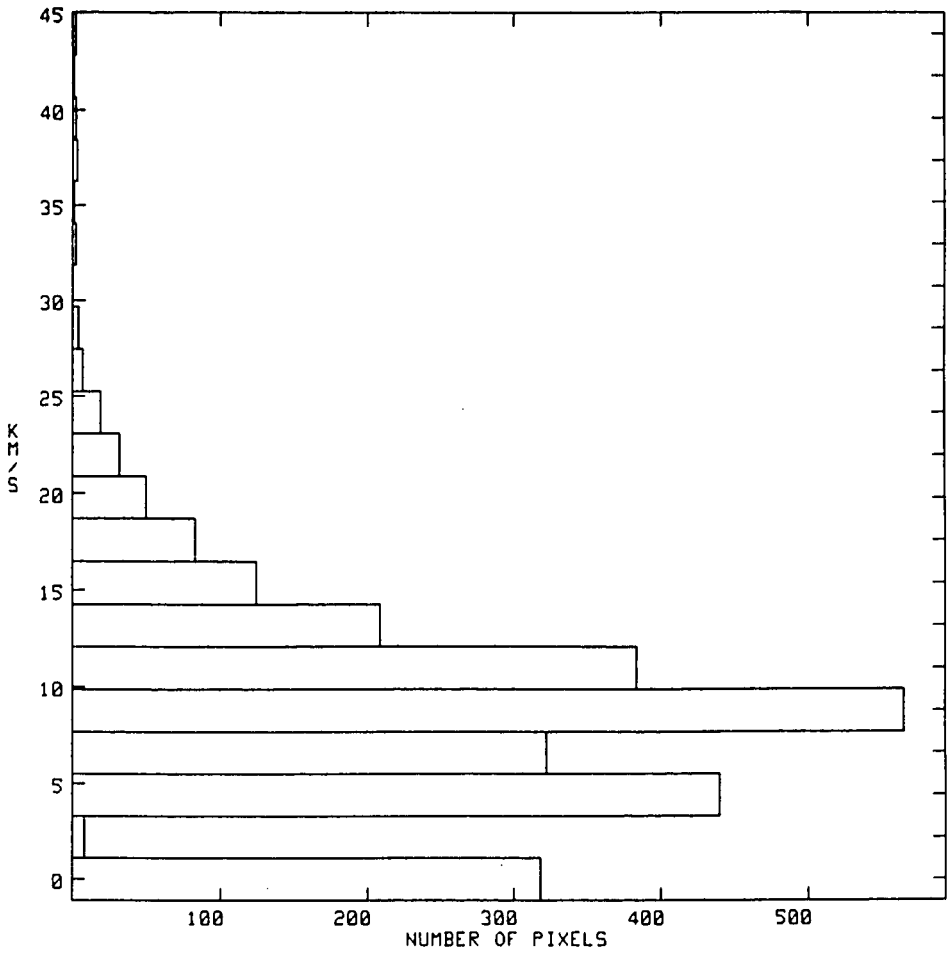

Figure 7.13 Histogram of Velocity Dispersion Values for NGC 3239

A histogram of the velocity dispersion at each of the pixels in the map in figure 7.12. The data have been binned ar 2.2 km/s intervals.

Figure 7.14 H I Spectra for 6 Positions in NGC 3239

The H I spectra for the six H I concentrations marked in figure 7.12.

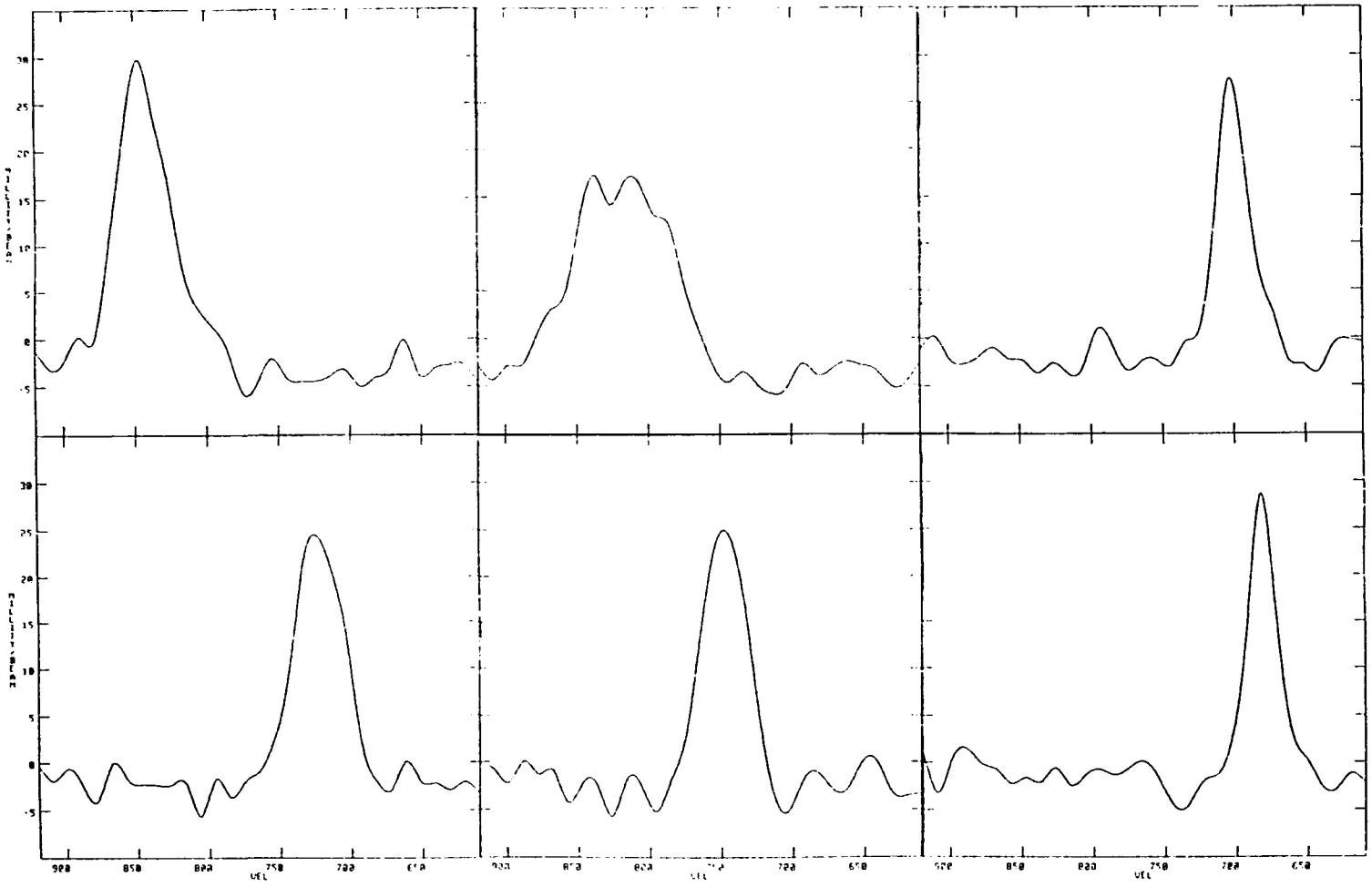

Table 7.3

Gaussian Fits to H I Spectra in NGC 3239

position	peak (mJy/beam)	error	velocity (km/s)	error	FWHM (km/s)	error
1	29.2	.5	844.3	.6	38.1	1.4
2	18.3	.5	818.3	1.3	62.7	3.0
3	27.0	.5	700.7	.4	25.0	.8
4	25.7	.4	723.1	.5	35.4	1.1
5	26.5	.5	747.8	.5	31.4	1.2
6	28.0	.4	681.9	.3	22.4	.7

velocity dispersions observed in NGC 3239 are inherent to the gas and not a result of integrating across changes in the velocity field. The correspondence of the peaks in the total H I map with the peaks in the second moment map is also strong evidence in favor of a gravitational explanation for the broad H I profiles.

Interpretation

The neutral gas environments of four GEHRs have been studied in the last section. All four GEHRs were found to be adjacent to large H I concentrations. The H I concentrations associated with the GEHRs were among the most massive in the parent galaxies, but comparable in size to other H I concentrations lacking GEHR companions. Table 7.4 lists several observed and derived properties for the four GEHRs. Despite the range of two orders of magnitude in the masses of the H I concentrations, the GEHRs studied here showed similarities in several properties. The values of the peak H I surface density and the average H I volume density are all very similar. All of the clouds have H I surface densities of about 3-4 x 10^{21} HI atoms/cm^2, and all of the estimated H I volume densities fall in the range of 0.5 to 4 cm^{-3}.

Comparing the H I density measurements with the H II density measurements revealed a consistent trend. In all cases, when a two component model of the GEHR was adopted, the ionized gas densities of the nuclear components were approximately 100 cm^{-3} (in good

Table 7.4

Properties of Four GEHRs

	NGC 5471	NGC 2363	NGC 4214 #1	NGC 3239 #1
M (H II) ($\times 10^6$ $M_\odot$)	20	2	4	140
M (H I) ($\times 10^6$ $M_\odot$)	60	3.1	5	200
D (H II) (pc)	680	315	370	1470
D (H I) (pc)	1530	790	850	2950
Γ	.7	2.5	1.1	1.4
[O III]/Hβ	7.5	9.4	4.5	6.6
HI s. d. (HI/cm^2)$\times 10^{21}$	4.4	4.0	2.5	4.2
FWHM (H II) (km/s)	57	41	34	45
FWHM (H I) (km/s)	41	...	25	38

agreement with the estimates from the optical spectroscopy), while the ionized gas densities of the halo components were about 1 cm^{-3} (in good agreement with the estimates of the surrounding neutral gas densities). The difference between the densities of the nuclei and the halos can be converted into an estimate of the filling factor for the ionized gas. If a GEHR is modelled simply as a condensation which has collapsed from an otherwise homogeneous environment, then the filling factor in the GEHR is simply the ratio of the volume densities. Nuclei with a density of 100 cm^{-3} in an environment of 1 cm^{-3} imply a volume filling factor of 0.01. This value can be compared with the recent studies of the volume filling factors of GEHRs by Kennicutt (1984) and O'Dell and Castaneda (1984). Both studies compare densities derived from optical spectroscopy with densities derived from Hα surface photometry. Kennicutt attributes the Hα surface brightness gradient to a decreasing r.m.s. electron density, and O'Dell and Castaneda model the gradient as an exponential decrease in the volume filling factor. Kennicutt determined filling factors of 0.01 for NGC 2363 and 0.09 for NGC 5471. O'Dell and Castaneda derived a value of 0.103 for the central volume filling factor of NGC 5471. Comparing the surrounding H I volume density with the derived central nuclear densities, the data reported here yield volume filling factors of .05 to .09 for NGC 5471 and .008 to .014 for NGC 2363. The agreement between these values imply that the pre-collapse densities of the clouds that formed the GEHRs were probably quite similar to the present densities in the

adjacent clouds.

The high resolution H I images presented here have shown that the H I concentrations are complex objects themselves. The result is that it is difficult to define precisely the size of an H I concentration associated with a GEHR. The H I concentrations are irregular in shape and gently blend into the background H I of the galaxy. One would then be drawn to the conclusion that investigations involving the sizes of H I clouds associated with GEHRs are vulnerable to all of the systematic errors that have plagued the studies of H II region diameters. In one such study, VAG have studied the relationship between H I and H II region diameters for the largest H II regions in M 101. They find a tight correlation between the H I/H II region size ratio and the distance of the H II region from the center of the galaxy. Since M 101 is also known to show a radial gradient in elemental abundances, the H I/H II region size ratio will correlate with elemental abundance. In pursuing this relationship, VAG devised a radio index for measuring the efficiency of massive star formation; Γ. Γ is the ratio of the mass of stars in an H II region to the mass of the neutral gas from which the stars formed, normalized by the average surrounding gas density. Γ can be expressed solely in terms of the radio observable quantities of the sizes and masses of the H I and H II regions. The resulting parameterization is:

$$\Gamma = (d_{HI}/d_{HII})^{3}(1 + M_{HI}/M_{HII})^{-2}$$

VAG point to the fact that a relationship between Γ and elemental abundance is meaningful if it holds not only for the H II regions in M 101, but for all H II regions. They plot Γ versus the excitation ([O III]/Hβ) and find a very good correlation for the H II regions from a handful of different galaxies.

Values for Γ and the global [O III]/Hβ ratios from the IRS observations are listed in table 7.4. Figure 7.15 shows the positions of these four regions in the Γ versus excitation plot of VAG. The agreement with the correlation found by VAG is very good for NGC 2363, but not very good for NGC 4214. Note the difference in the values for NGC 5471, the one GEHR both studies have in common. The difference arises mainly due to a discrepancy in the estimate of the H II region diameter. Considering the uncertainties associated with the variables used to calculate Γ, it is surprising that there is not a larger scatter. Nonetheless, the suggestion of the relationship, that metal poor gas is much more efficient at forming massive stars, seems well founded.

The high spatial and velocity resolution observations of NGC 4214 and NGC 3239 have shown that the velocity dispersion in the neutral gas is correlated with the H I surface density. In table 7.4, the velocity dispersions of the H I in the clouds adjacent to the GEHRs are compared to the velocity dispersions obtained from Hα

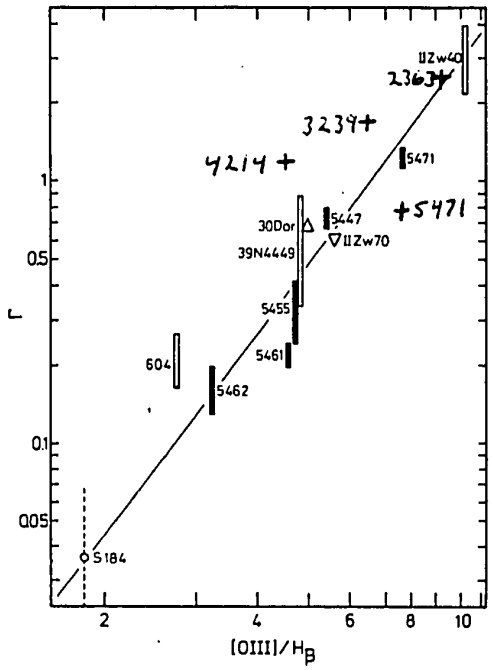

Figure 7.15 Plot of Γ versus [O III]/Hβ

The plot of Γ versus [O III]/Hβ copied from VAG. The four GEHR discussed here have been added to the figure.

Echelle spectroscopy (Skillman and Balick 1984). In both cases the velocity dispersion of the neutral gas is more than 70 percent of the velocity dispersion of the ionized gas. This strongly supports the hypothesis that the large velocity dispersions observed in GEHRs are due to the motions in the original H I cloud from which the GEHR formed, and not due to the energy released by the stars.

Terlevich and Melnick (1981) originally proposed that the broad lines of GEHR were due to the self-gravitating nature of the H I - H II complexes. In their study they compared the velocity dispersion of the ionized gas and the adjacent neutral gas of five GEHRs. The agreement was generally excellent. Unfortunately, these measurements were quoted without errors, and the results were subject to several biases which were left unexplored. In one case (Hubble X), the quoted velocity dispersion was 11 km/s for the H I and 9.8 km/s for the H II. This is nearly identical to the average value one would expect at any position in any galaxy. --Allsop (1978) and Tully et al. (1978) find typical values of the r.m.s. dispersion of the neutral gas in Irregular galaxies between 6 and 11 km/s, and van der Kruit and Shostak (1982,1983) and Shostak and van der Kruit (1984) find a range of 7 to 12 km/s for spiral galaxies.-- For the other four values, the limited velocity resolution and/or spatial resolution of the observations make the results vulnerable to significant errors of the types already discussed.

It may be premature to wholeheartedly endorse the Terlevich and Melnick portrayal of GEHRs solely on the basis of H I observations of NGC 4214 and NGC 3239. Consider for a moment the case of NGC 604, a GEHR in M 33. Terlevich and Melnick presented the agreement between the H I velocity dispersion (17 km/s; Wright 1971) and the H II velocity dispersion (17.8 km/s; Melnick 1979) as evidence supporting the case of a gravitationally bound system. In contrast, Wright had concluded from his radio data that NGC 604 was a factor of 10 shy of being massive enough to be gravitationally bound. Rosa and Solf (1984) interpreted the coincidence of high velocity structures in the ionized gas of the order of 100 km/s with the positions of Wolf-Rayet stars to 'clearly rule out' the dominance of gravitational motions in broadening the emission line profiles. The data will allow ample room for future debate.

On their own, the H I data presented here are suggestive, but the idea that large H I clouds have large velocity dispersions is also supported by the work of VAG. VAG reported a range of 11 to 25 km/s for the velocity dispersion of the H I associated with five GEHRs in M 101. For three of these GEHRs, the agreement between the H I and Hα velocity dispersions was within reported errors. The limitations of their observations in both spatial resolution (FWHM = 1 kpc) and velocity resolution (FWHM = 27 km/s) limits the confidence of any conclusions drawn from this small data base, but it definitely supports the model of a GEHR as a gravitationally bound system.

Viallefond, Goss, and Allen (1982) have investigated the formation process of a GEHR following Elmegreen's (1979) description of a self-gravitational collapse. In comparing the observations of VAG with the theoretical predictions of Elmegreen, it is concluded that the GEHRs in M 101 can arise quite naturally as density wave triggered star formation in gravitationally bound massive cloud complexes. The key element connecting the H I concentrations of M 101 to Elmegreen's theory is the change in morphology of the H I gas clouds with galactocentric radius. Only if the H I clouds are gravitationally self-bound would one expect the observed change from elongated to spherical shapes with increasing radius. It should be noted as an aside here that the theory of Elmegreen cannot be applied directly to the GEHRs in Irregular galaxies because there is no evidence for density waves in Irregular galaxies. On the other hand, there are kinematical warps in both NGC 4214 and NGC 3239, and perhaps these warps fulfill the role of the triggering mechanism in these two galaxies.

Conclusions

The H I observations presented here have shown that GEHRs are always associated with large H I concentrations. The comparison of gas densities derived from optical and radio measurements imply that GEHRs are produced as the result of a collapse from gas at an average density of 1 atom/cm^3 and that the density of the gas in the vicinity of the newly formed stars is of the order of 100 atoms/cm^3. The

filling factors obtained from a direct comparison of the ionized and neutral gas densities derived from radio measurements are consistent with those derived from optical methods.

A GEHR will always be located near to one of the most massive H I concentrations in its parent galaxy, but the presence of a massive H I concentration does not imply the presence of a GEHR. This does not rule out the possibility that every massive H I concentration will produce a GEHR. The collapse phase of a giant H I cloud lasts about ten times longer than the lifetime of the stars responsible for ionizing the gas (Elmegreen 1979). The balance between the relative lifetimes of the two phases and the number of generations of GEHRs that a single H I concentration can form will determine the relative number of GEHRs to H I concentrations.

GEHRs require a minimum surface density of 2-4 x 10^21 atoms/cm^2 of neutral hydrogen in order to form. The data suggest that some form of a galaxy scale dynamical disturbance, either a density wave or a warp is needed in order to trigger that star formation event.

The velocity dispersion in the neutral gas adjacent to a GEHR shows the same type of anomalously broad line width that has been observed in the ionized gas. This is taken as strong evidence that the source of the broad lines is gravitational and not a product of the energy released from stars.

Chapter VIII Summary and Conclusions

The introductory chapter contained a demonstration of the key role of GEHR observations to many areas of current astrophysical research, a summary of current problems and discrepant notions concerning GEHRs, and a description of an observational program designed to shed some light on those problems. It is now time to take stock and to judge what progress, if any, has been made. The introductory section on current problems was divided into three main categories: problems of reddening and extinction; problems of physical conditions and elemental abundance analyses; and problems concerning the anomalously broad emission line widths and the true nature of GEHRs. Thus, this final chapter will also take a tripartite form.

Perhaps the most important result of all of the work concerning extinction and reddening is the evidence that the large discrepancy between results from the optical method and the radio-optical method may be almost entirely due to resolution effects. This would imply that most of the dust responsible for the extinction is distributed in clumps external to the GEHR. In this case it is probably inappropriate to consider the large amount of extinction implied by the radio-optical method when dereddening optical spectra.

It would be very desirable to have far infrared maps of GEHRs to attempt to locate the dust. Comparing the infrared maps with radio continuum maps might lead to a better description of the distribution of the dust, specifically if the dust is internal to the ionizing gas region. By concentrating on local group GEHRs, one can gain in real spatial resolution, and improvements on the data in the literature for NGC 595, NGC 604, 30 Doradus, and Hubble V are certainly possible. It would be very important to have far infrared measurements of GEHRs that encompass a large range of excitation values. This would allow an investigation of the relationship of the dust content with the metal abundance by direct observations of the dust as opposed to inferences from reddening and extinction measures. If the anomalous extinction is basically a resolution effect, then even higher resolution observations should be definitive. Good seeing conditions would allow an improvement of up to a factor of three over the resolution of Hα and Hβ imaging presented here. Full synthesis maps in the same configuration, or λ6 cm VLA A configuration observations would allow matching resolution radio continuum observations.

The study of chemical abundance analysis presented here has yielded both support for and criticism of standard abundance analysis as applied to GEHRs. As long as both the singly and doubly ionized species of oxygen are measured, the total oxygen abundance is very nearly independent of aperture size or position in a GEHR. The

exception to this occurs when the spectrum is contaminated by the presence of a supernova remnant. The case for nitrogen abundances is just the opposite however. Total nitrogen abundances can vary by factors of two or more with changes in both aperture size and position. It is not clear if this is a fundamental statement about the nucleosynthetic history of nitrogen production, or if the problems associated with converting observed relative λ3727 and λ6584 intensities into relative oxygen and nitrogen abundances are just limited to accuracies of no better than factors of two. The presence of supernova remnants appears to represent a real wild card in the abundance analysis process for GEHRs. It has been shown that there is every reason to expect their presence, and that their ability to affect the derived abundance outdistances their detectability. The only suggested solution is that a measurement of the λ6300 line of [O I] is a mandatory prerequisite for accurate GEHR abundance analysis work. The presence of a radial gradient, in either temperature, ionization structure, or both, has been found to be universal in GEHRs. Temperature variations from nucleus to nucleus exist at about the ten percent level.

The results of this study suggest several additional observations. Imaging in the λ3727 line of [O II] could be combined with the λ5007 [O III] images to construct maps of the ionization structure. Images in [S II], and, for the nearest regions, [O I] could serve to search for supernova remnants. It would be especially

important to make these observations for GEHRs like NGC 2363 where the radio spectral index is nonthermal, yet none of the nuclei show any sign of enhanced [S II] or [O II]. Long slit spectra would provide another means of investigating the radial gradient in physical conditions. It is very important to get spectra of the low surface brightness halo gas, and follow up on the differences discovered between the large and small aperture spectrophotometry. The difference between a gradient in the filling factor and a gradient in the r.m.s. electron density can be determined by following variations along the slit in the density dependent forbidden line ratios. Temperature gradients and ionization structure can also be explored in this way. It should be noted that the task of getting enough telescope time to do the job properly would be formidable. The spectra here represent typical integration times of 15 minutes to one hour. Ideally one would like to follow the variations in physical conditions out from the core and into the halo. The decrease in surface brightness of a factor of 100 or more means that only the brightest lines of oxygen and hydrogen can be hoped to be seen.

The neutral hydrogen observations have presented the key to understanding the anomalous kinematics of GEHRs. Although supernova remnants and Wolf-Rayet stars may be doing their share of pushing around the ionized gas, it is doubtful that either would leave a significant impression on the kinematics of the neutral gas. If one

accepts the fact that the large H I concentrations show a larger velocity dispersion than the rest of the gas in the disk of the galaxy, then it follows naturally that when this gas is ionized following a nearby star formation event, the ionized gas should reflect the original velocity dispersion of the neutral gas. There is good evidence that the filling factor in the ionized gas is quite small; on the order of 0.1 or less. The large velocity dispersion in the neutral gas implies that the filling factor of the H I must also be small. In a uniform density gas, the large velocity dispersion would mean an unreasonably high temperature. If the neutral gas is thought of as highly clumped, than the neutral cloudlets could be moving with speeds of up to their free fall velocity. To take this scenario further, the cloudlet-cloudlet collisions may be responsible for initiating star formation.

If GEHRs and their associated H I concentrations are coherent, gravitationally bound systems, then many exciting possibilities are realized. Terlevich and Melnick (1981) proposed the use of the correlation of GEHR Hβ luminosities with line widths to construct a distance indicator for galaxies. Both Viallefond, Goss and Allen (1982) and Terlevich and Melnick (1984) draw conclusions about the initial mass function for massive star formation from correlations based on GEHRs. Starting with an initial mass function resembling the one in our galaxy, Viallefond, Goss, and Allen conclude that the upper mass cut-off must be a function of heavy element abundance.

Terlevich and Melnick begin with the stellar evolution models of Melnick, Terlevich, and Eggleton (1984), and conclude that the slope of the initial mass function must be a function of total heavy element abundance. In both cases, the studies could only benefit from more and better data.

A first goal is to establish the physical limit of a gravitationally bound complex. When estimating the mass of the cloud responsible for the formation of a GEHR, is the total mass of the GEHR and all of the neutral gas surrounding it appropriate, or is the relevant dynamical unit just the mass of gas that collapsed to form the GEHR? VAG have found some surprisingly tight correlations combining the estimated masses and sizes of the neutral hydrogen clouds and the ionized gas clouds. The success of these relationships is even more surprising considering the uncertainties involved in the measured quantities. High spatial and velocity resolution H I observations of galaxies showing star formation on all scales will be important to test the range of the relationships discussed by VAG. It would be interesting to compare the distribution of sizes of H I clouds to the already catalogued distributions of H II region sizes.

High velocity resolution observations of the halo gas of GEHRs is also important. To date, such observations exist only for 30 Doradus (Smith and Weedman 1972) and NGC 604 (Rosa and Solf 1984). If this type of observation can be combined with high resolution H I

observations, the presence or absence of discontinuities in the kinematics between the H I and H II can be investigated.

Additionally, an extension of this observational program to star forming regions of an even larger scale would be of great interest. The star-burst nuclei galaxies (Weedman et al. 1981, Balzano 1983, Gehrz, Sramek, and Weedman 1983) appear to be larger scale versions of GEHRs in which the importance of supernova remnants is already recognized. The recent suggestion by Weedman (1984) that star-burst nuclei are the precursors to Seyfert nuclei adds impetus to this course of study.

Bibliography

Abbott, D. C. 1982, Ap. J., 263, 723.

Aller. L. H. 1942, Ap. J., 95, 52.

Alloin, D., Collin-Souffrin, S., Joly, M., Vigroux, L. 1979, Astr. Ap., 78, 200.

Allsop, N. J. 1978, M. N. R. A. S., 184, 397.

_____. 1979, M. N. R. A. S., 188, 765.

Baldwin, J. A., Phillips, M. M., and Terlevich, R. 1981, Pub. A. S. P., 93, 5 (BPT).

Balick, B., and Sneden, C. 1976, Ap. J., 208, 336.

Balzano, V. A. 1983, Ap. J., 268, 602.

Benvenuti, P., D'Odorico, S., and Dumontel, M. 1979, Ap. Space Sci., 66, 39.

Bignell, R. C. and Seaquist, E. R. 1983, Ap. J., 270, 140.

Brocklehurst, M. 1971, M.N.R.A.S., 153, 471.

_____. 1972, M.N.R.A.S., 157, 211.

Brugel, E. W. 1980, Ph.D. thesis, University of Washington.

Butcher, H. and Oemler, A.,Jr. 1978, Astr. Ap., 219, 18.

Clark, B. G. 1980, Astr. Ap., 89, 377.

Conti, P. S., and Massey, P. 1981, Ap. J., 249, 471.

Costero, R., and Peimbert, M. 1970, Bol. Obs. Tonantzintla y Tacubaya, 5, 229.

Danziger, I. J., Goss, W. M., Murdin, P., Clark, D. H., and Boksenberg, A. 1981, M.N.R.A.S., 195, 33p.

de Vaucouleurs, G., de Vaucouleurs, A., and Corwin, H. G. 1976, Second Reference Catalogue of Bright Galaxies, University of Texas Press, Austin and London.

Dickel, J. R., and Rood, H. J. 1978, Ap. J., 223, 391.

D'Odorico, S., and Dopita, M. A. 1983, in IAU Symposium 101, Supernova Remnants and their X-ray Emission, ed. P. Gorenstein and J. Danziger (Dordrecht: Reidel), p517.

D'Odorico, S., and Rosa, M. 1981, Ap. J., 248, 1015.

D'Odorico, S., Rosa, M., and Wampler, E. J. 1983, Astr. Ap. Suppl., 53, 97.

Dopita, M. A., Binette, L., D'Odorico, S., and Benvenuti, P. 1984, Ap. J., 276, 653.

Dopita, M. A., D'Odorico, S., and Benvenuti, P. 1980, Ap. J., 236, 628.

Dufour, R. J., Talbot, R. J., Jensen, E. B., and Shields, G. 1980, Ap. J., 236, 119.

Dyson, J. E., 1979, Astr. Ap., 73, 132.

Dyson, J. E., and Williams, D. A. 1980, Physics of the Interstellar Medium, (New York : John Wiley and Sons), p173.

Edmunds, M. G., and Pagel, B. E. J. 1978, M. N. R. A. S., 185, 77p.

Elmegreen, B. G. 1979, Ap. J., 231, 372.

Elmegreen, B. G. and Lada, C. J. 1977, Ap. J., 214, 725.

Feast, M. W., Thackeray, A. D., and Wesselink, A. J. 1960, M. N. R. A. S., 121, 337.

Filippenko, A. V. 1982, Pub. A. S. P., 94, 715.

French, H. B. 1980, Ap. J., 240, 41.

French, H. B. and Grandi, S. A. 1981, Ap. J., 244, 493.

Gallagher, J. S. and Hunter, D. A. 1983, Ap. J., 274, 141.

Gebel, W. L. 1968, Ap. J., 153, 743.

Gehrz, R. D., Sramek, R. A., and Weedman, D. W. 1983, Ap. J., 267, 551.

Gilmozzi, R., Murdin, P., Clark, D. H., Malin, D. 1983, M.N.R.A.S., 202, 927.

Hawley, S. A., and Duncan, D. K. 1976, Pub. A. S. P., 88, 672.

Hayes, D., and Massey, P. 1984, KPNO Newsletter, No. 33, p7.

Heckman, T. M. 1980, Astr. Ap., 87, 152.

Hodge, P. W. 1983, A. J., 88, 1323.

Hodge, P. W., and Kennicutt, R. C. 1983, A. J., 88, 296.

Hogbom, J. 1974, Ap. J. Suppl., 15, 417.

Huchra, J. P. 1977, Ap. J., 217, 928.

Israel, F. P., Goss, W. M., and Allen, R. J. 1975, Astr. Ap., 40, 421 (IAG).

Israel, F. P. and Kennicutt, R. C. 1980, Astr. Lett., 21, 1.

Kennicutt, R. C. 1979, Ap. J., 228, 394.

_____. 1984, preprint.

Kennicutt, R. C., Balick, B., and Heckman, T. 1980, Pub. A. S. P., 92, 134.

Kinman, T. D., and Davidson, K. 1981, Ap. J., 243, 127.

Klein, U., Grave, R., and Wielebinski, R. 1983, Astr. Ap., 117, 332.

Kunth, D. and Sargent, W. L. 1983, Ap. J., 273, 81 (KS).

Lamers, 1982, Proceedings of the NATO Advance Studies Institute on Diffuse Matter in Galaxies, Cargese, ed. Adouze, Lequeux, Levy, Vidal-Madjar, (Dordrecht : Reidel), p35.

Lequeux, J. 1979, Astr. Ap., 71, 1.

_____. 1980, Star Formation, eds. A. Maeder and L. Martinet, Geneva Observatory, Geneva.

Lequeux, J., Maucherat-Joubert, M., Deharveng, J. M., and Kunth, D. 1981, Astr. Ap., 103, 305.

Lequeux, J., Peimbert, M., Rayo, J. F., Serrano, A. and Torres-Peimbert, S. 1979, Astr. Ap., 80, 155.

Massey, P., and Hutchings, J. 1983, Ap. J., 275, 578.

Mathewson, D. S. and Clarke, J. N. 1973, Ap. J., 180, 725.

Mathis, J. S. 1983, Ap. J., 267, 119.

Mathis, J. S., Rumpl, W., and Nordsieck, K. H. 1977, Ap. J., 217, 425.

McCall, L. M. 1982, Ph. D. thesis, University of Texas.

Melnick, J. 1977, Ap. J., 213, 15.

_____. 1978, Astr. Ap., 70, 157

_____. 1979, Ap. J., 228, 112.

Melnick J., and Terlevich, R. 1984, Preprint.

Mezger, P. G., and Henderson, A. P. 1967, Ap. J., 147, 471.

Miller, J. S. 1974, Ap. J., 189, 239.

Milne, D. K., Caswell, J. L., and Haynes, R. F. 1980, M. N. R. A. S., 191, 469.

O'dell, C. R., and Castaneda, H. O. 1984, Ap. J., 283, 158.

Oster, L., 1961, Ap. J., 134, 1010.

Osterbrock, D. E. 1970, Quart. J. R. A. S., 11, 199.

____. 1974, Astrophysics of Gaseous Nebulae (San Francisco : Freeman)

Pagel, B. E. J., and Edmunds, M. G. 1981, Ann. Rev. Astr. Ap., 19, 77.

Pagel, B. E. J., Edmunds, M. G., Blackwell, D. E., Chun, M. S., and Smith, G. 1979, M. N. R. A. S., 189, 95.

Pagel, B. E. J., Edmunds, M. G., and Smith, G. 1980, M.N.R.A.S., 193, 219.

Parker, E. A. 1968, M.N.R.A.S., 138, 407.

Peimbert, M. 1975, Ann. Rev. Astr. Ap., 13, 113.

Peimbert, M., and Costero, R. 1969 Bol. Obs. Tonantzintla y Tacubaya, 5, 3.

Peimbert, M., and Torres-Peimbert, S. 1974, Ap. J., 193, 327.

_____. 1977, M. N. R. A. S., 179, 217.

Pradhan, A. K. 1978, M.N.R.A.S., 183, 89p.

Rayo, J. F., Peimbert, M., and Torres-Peimbert, S. 1982, Ap. J., 255, 1 (RPT).

Reike, G. H., Lebofsky, M. J., Thompson, R. I., Low, F. J., and Tokunaga, A. T. 1980, Ap. J., 238, 24.

Rosa, M. 1980, Astr. Ap., 85, L21.

_____. 1983, Highlights of Astronomy, 6, 625.

Rosa, M., and D'Odorico, S. 1982, Astr. Ap., 108, 339.

Rosa, M., and Solf, J. 1984, Astr. Ap., 130, 29.

Rubin, R. H. 1968, Ap. J., 154, 391.

_____. 1983, Ap. J., 274, 671.

Sandage, A. 1973, Ap. J., 183, 711.

Sandage, A., and Tammann, G. A. 1974a, Ap. J., 190, 525.

_____. 1974b, Ap. J., 194, 223.

_____. 1974c, Ap. J., 194, 559.

Sargent, W. L. W., and Searle, L. 1970, Ap. J. (Letters), 162, 1155.

Schild, R. E. 1977, A. J., 82, 5.

Searle, L. 1971, Ap. J., 168, 327.

Seaton, M. J. 1975, M.N.R.A.S., 170, 475.

Sedwick, K. E., and Aller, L. H. 1981, Proc. Nat. Acad. Sci USA, 78, 1994.

Seyfert, C. K. 1940, Ap. J., 91, 261.

Shields, G. A. and Searle, L. 1978, Ap. J., 222, 821.

Shields, G. A. and Tinsley, B. M. 1976, Ap. J., 203, 66.

Shostak, G. S., and van der Kruit, P. C. 1984, Astr. Ap., 132, 20.

Skillman, E. D., and Balick, B. 1984, Ap J., 280, 580.

Smith, H. E. 1975, Ap. J., 199, 591.

Smith, M. G., and Weedman, D. W. 1970a, Ap. J., 160, 65.

_____. 1970b, Ap. J., 161, 33.

_____. 1972, Ap. J., 172, 307.

Stasinska, G. 1980, Astr. Ap., 84, 320.

Talbot, R. J., and Arnett, W. D. 1974, Ap. J., 190, 605.

Terlevich, R., and Melnick, J. 1981, M.N.R.A.S., 195, 839.

_____. 1984, preprint.

Tody, D. 1980, Proc. S. P. E., 264, 121.

Torres-Peimbert, S., Peimbert, M., and Daltabuit, E. 1980, Ap. J., 238, 133.

Tully, R. B., Boesgaard, A. M., Dyck, H. M., and Schempp, W. V. 1981, Ap. J., 246, 38.

Tully, R. B., Bottinelli, L., Fisher, R. J., Gougnenheim, L., Sancisi, R., and van Woerden, H. 1978, Astr. Ap., 63, 37.

van den Bergh, S. 1980, Ap. J., 235, 1.

van der Kruit, P. C. and Shostak, G. S. 1982, Astr. Ap., 105, 351.

_____. 1983, Internal Kinematics and Dynamics of Galaxies, p.86, IAU Symp. No. 100, ed. E. Athanassoula, Reidel,Dordrecht.

Viallefond, F. V., Allen, R. J. A., and Goss, W. M. G. 1981, Astr. Ap., 104, 127 (VAG).

Viallefond, F. V., Goss, W. M., and Allen, R. J. 1982, Astr. Ap., 115, 373.

Weaver, R., McCray, R., and Castor, J. 1977, Ap. J.,218, 377.

Weedman, D. W. 1983, Ap. J., 266, 479.

Weedman, D. W., Feldman, F. R., Balzano, V. A., Ramsey, L. W., Sramek, R. A., and Wu, C. 1981, Ap. J., 248, 105.

Wevers, B. M. H. R. 1984, PhD. thesis, University of Groningen.

Whitford, A. E. 1958, A. J., 63, 210.

Wright, M. C. H. 1971, Astr. Letts., 7, 209.

Vita

Evan David Skillman, the son of David C. and Frances H. Skillman, was born in Rochester, New York on January 27, 1955. He was valedictorian of his graduating class at Greece Athena High School in June 1973. In May 1977 he received a Bachelor of Arts in Physics from Cornell University, and in May 1978 he was a member of the starting line-up of the Eastern Championship Cornell University Big Red Buds Ultimate Frisbee Team. In September 1978 he began study in the graduate program in astronomy at the University of Washington in Seattle where he distinguished himself by having the nicest office.